Space Sci Rev (2016) 200:205–259
DOI 10.1007/s11214-016-0234-7

Origins of the Earth's Diffuse Auroral Precipitation

Binbin Ni[1] · Richard M. Thorne[2] · Xiaojia Zhang[2,3] · Jacob Bortnik[2] · Zuyin Pu[4] · Lun Xie[4] · Ze-jun Hu[5] · Desheng Han[5] · Run Shi[6] · Chen Zhou[1] · Xudong Gu[1]

Received: 7 September 2015 / Accepted: 5 January 2016 / Published online: 2 February 2016

Abstract The Earth's diffuse auroral precipitation provides the major source of energy input into the nightside upper atmosphere and acts as an essential linkage of the magnetosphere-ionosphere coupling. Resonant wave-particle interactions play a dominant role in the scattering of injected plasma sheet electrons, leading to the diffuse auroral precipitation. We review the recent advances in understanding the origin of the diffuse aurora and in quantifying the exact roles of various magnetospheric waves in producing the global distribution of diffuse auroral precipitation and its variability with the geomagnetic activity. Combined scattering by upper-and lower-band chorus accounts for the most intense inner magnetospheric electron diffuse auroral precipitation on the nightside. Dayside chorus can be responsible for the weaker dayside electron diffuse auroral precipitation. Pulsating auroras, the dynamic auroral structures embedded in the diffuse aurora, can be mainly caused by modulation of the excitation of lower band chorus due to macroscopic density variations in the magnetosphere. Electrostatic electron cyclotron harmonic waves are an important or even dominant cause for the nightside electron diffuse auroral precipitation beyond $\sim 8R_e$ and can also contribute to the occurrence of the pulsating aurora at high L-shells. Scattering by electromagnetic ion cyclotron waves could quite possibly be the leading candidate responsible for the ion precipitation (especially the reversed-type events of the energy-latitude dispersion) in the regions

✉ B. Ni
bbni@whu.edu.cn

1 Department of Space Physics, School of Electronic Information, Wuhan University, Wuhan, Hubei 430072, China

2 Department of Atmospheric and Oceanic Sciences, University of California, Los Angeles, Los Angeles, CA 90095-1565, USA

3 Department of Earth, Planetary, and Space Sciences, University of California, Los Angeles, Los Angeles, CA 90095-1567, USA

4 Institute of Space Physics and Applied Technology, Peking University, Beijing 100871, China

5 SOA Key Laboratory for Polar Science, Polar Research Institute of China, Shanghai 200136, China

6 Department of Mathematics and Statistics, Memorial University of Newfoundland, St. John's, Newfoundland A1C 5S7, Canada

of the central plasma sheet and ring current. We conclude the review with a summary of current understanding, outstanding questions, and a number of suggestions for future research.

1 Introduction

An aurora, sometimes referred to as a polar light, is a natural light display in the sky, predominantly seen at high latitudes, e.g., the Arctic and Antarctic regions, caused by the collision of energetic charged particles with atoms in the upper atmosphere. Occasionally, auroras are also seen at latitudes below the auroral zone when the solar wind becomes very active and/or the geomagnetic activity is substantially intensified. It was Loomis (1860) that produced the first concrete morphological map of the aurora, which was followed by Fritz (1873) that reported auroral sightings on a global scale. The modern auroral morphology began when Feldstein (1963) determined the geometry of the auroral oval on the basis of the International Geophysical Year (IGY) all-sky camera network (Akasofu 2012). From then on, the wealth of data (either ground-based or space-borne) on polar auroras has grown massively, so has our knowledge on the comprehensive, global picture of the terrestrial auroras.

It has been well recognized that auroras take place in various forms. In general, auroras can be primarily classified as discrete or diffuse aurora. The discrete auroras are sharply defined structures, which vary in brightness from just barely visible to the naked eye to bright enough to read a newspaper at night. Discrete auroras are usually observed only in the night sky because they are not as bright as the sunlit sky. They can change within seconds or remain unchanged for hours, in association with electron acceleration by two distinct physical mechanisms, namely, quasi-static electric fields, producing inverted V-type (i.e., monoenergetic) auroras, and dispersive Alfven waves, producing broadband auroras (Frank and Ackerson 1971; Burch 1991; Newell 2000; Newell et al. 2009). In contrast, the diffuse aurora is a featureless glow in the sky, which may not be visible to the naked eye even on a dark night and occurs on the equatorward part of the auroral zone to define the extent of the latter. Unlike the discrete aurora, the diffuse aurora is relatively unstructured and is a semi-permanent feature of the auroral ionosphere, more likely connecting to wave-induced scattering processes (e.g., Davidson 1990; Shprits et al. 2008a, 2008b; Thorne et al. 2010; Lessard 2012).

As the focus of this review, more specifically, the diffuse aurora is a belt of weak emissions extending around the entire auroral oval. In the early 1960's, using optical data at many Antarctic stations principally in the years 1959 and 1963, Sandford (1968) performed an extensive statistical study of variations of auroral emissions with time, geomagnetic activity, and the solar cycle. The first observations of the diffuse aurora in space were reported by Lui and Anger (1973). Using Polar PIXIE X-ray observations, Petrinec et al. (1999) statistically examined the auroral intensity caused by energetic electron (2–25 keV) precipitations at different geomagnetic activities (as shown in Fig. 1) and found that it intensifies significantly with increasing geomagnetic activity levels (denoted by Kp, AE and Dst indices). A recent statistical study on precipitation from different types of aurora, based on 11 years of DMSP observations, showed that the diffuse aurora constitutes 84 % of the energy flux into the ionosphere during low solar wind driving conditions and 71 % of that during high solar wind driving conditions (Newell et al. 2009). Figure 2 shows the pattern of electron diffuse aurora in the ionosphere. Their energy flux is enhanced by a factor of three from low to high solar wind driving conditions.

The diffuse aurora extends over a latitude range of 5° to 10° and maps along the magnetic field lines from the outer radiation belts ($L \sim 4$) to the entire central plasma sheet

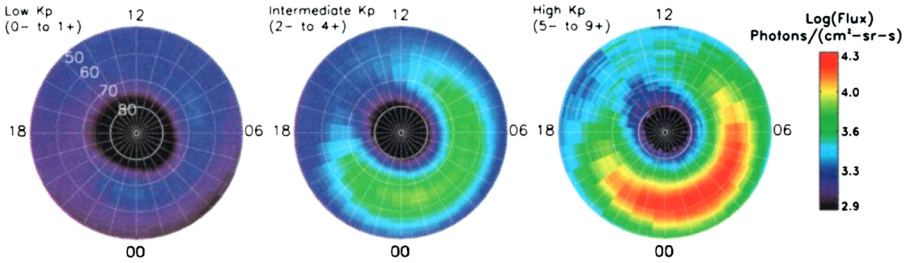

Fig. 1 Adapted from Fig. 2 of Petrinec et al. (1999). Averaged statistical X-ray aurora (northern hemisphere) as observed by PIXIE (5-minute exposure) during the interval April 1996–July 1998, as a function of geomagnetic activity as determined by the Kp index

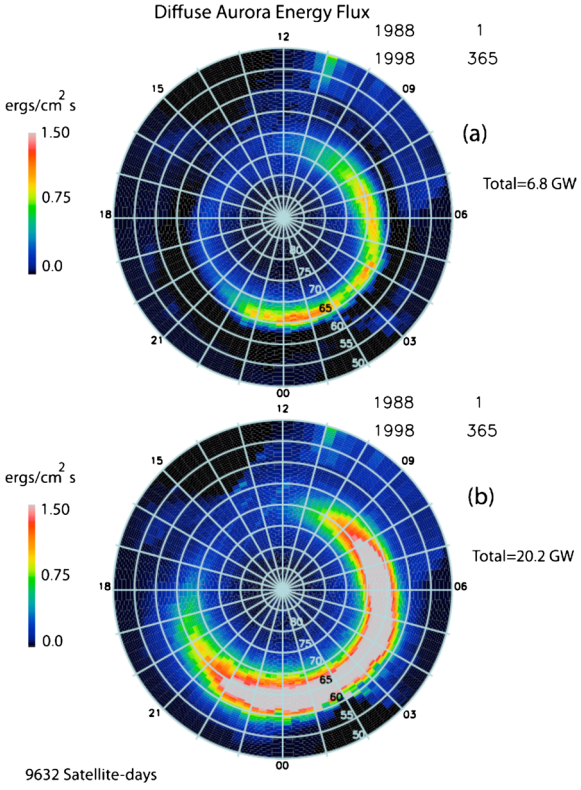

Fig. 2 Corrected version of Fig. 5 of Newell et al. (2009). Diffuse aurora hemispheric energy flux for (**a**) low and (**b**) high solar wind driving

($L \sim 12$) (Petrinec et al. 1999; Newell et al. 2009; Meredith et al. 2009), with significant precipitations from middle to outer magnetosphere ($L > 8$) during low solar wind driving. However, as shown in Figs. 1 and 2, such a contribution from middle to outer magnetosphere decreases under geomagnetically moderate and active conditions. Latitudinal ranges and peak energy flux location of the diffuse aurora also vary with the solar wind conditions and seasonal changes (Newell et al. 2009, 2010). As solar wind condition intensifies, the diffuse auroral latitudinal range expands into both lower and higher latitudes, and the location of peak energy flux moves to lower latitudes well below 65°. Owing to the predominant eastward transport of electrons as a result of a combination of $\mathbf{E} \times \mathbf{B}$ and gradient drifting

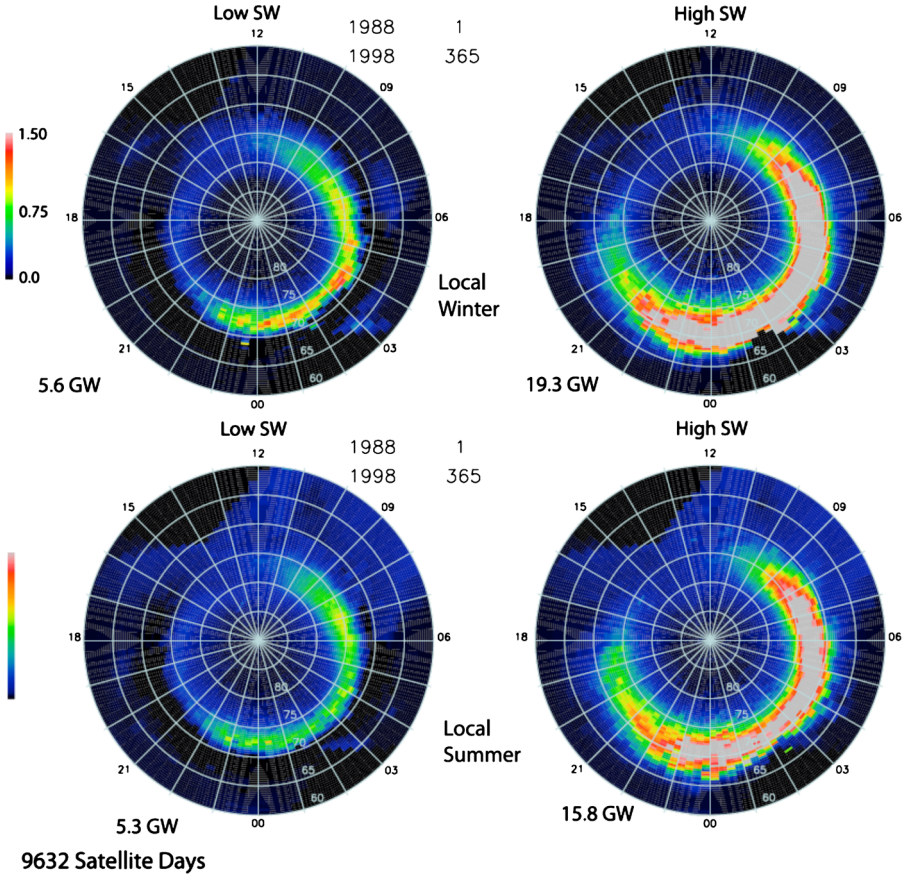

Fig. 3 Adapted from Fig. 1 of Newell et al. (2010). Diffuse aurora hemispheric flux for (*top*) local winter and (*bottom*) local summer. (*left*) Low and (*right*) high solar wind driving

from the nightside plasma sheet, the diffuse aurora is most intense in the magnetic local time (MLT) sector from premidnight to dawn. Precipitation loss leads to greatly reduced energy deposition on the dayside and relatively insignificant input from postnoon through dusk. The seasonal variations in the diffuse aurora are also found to be the dominant contributor to seasonal variations of energy input to the ionosphere. The precipitating energy flux of the diffuse aurora is greater during winter than summer, as illustrated in Fig. 3. For the nightside aurora, which dominates the energy flux, this is true for both low and high solar wind driving conditions, and the seasonal effect on the nightside diffuse aurora is much more pronounced for strong solar wind driving despite a localized exception for the pre-midnight sector. In contrast, the seasonal variation pattern for the dayside diffuse aurora is more nuanced. Higher energy fluxes occur on the dayside in summer, at least for quiet conditions, while for active conditions the dayside has about the same energy flux in the summer as in the winter. Another very prominent features of the seasonal variation of the diffuse aurora is the strong tendency for much higher number fluxes on the dayside during the summer. Han et al. (2015) extensively surveyed both structured and unstructured dayside diffuse aurora based on 7-year optical auroral observations obtained at the Chinese Arctic Yellow River Station. They reported that the unstructured dayside diffuse aurora normally shows

homogeneous luminosity in a large region and sometimes are embedded with black auroral structures, whereas the structured dayside diffuse aurora mainly shows patchy, striped, or irregular shapes.

Both ion precipitation and electron precipitation contribute to the occurrences of the diffuse aurora. Ion precipitation is thought to mainly result from field line curvature scattering when the radius of the curvature of the field lines in the stretched magnetotail becomes comparable to the gyro-radius of a trapped particle. The integral ion energy flux maximized at premidnight during all levels of geomagnetic activity. However, the average integral number flux and energy flux of the precipitating ions is typically 1 to 2 orders of magnitude less than that of the precipitating electrons at all latitudes, MLTs, and activities (Hardy et al. 1985, 1989). Therefore, electron precipitation plays a dominant role in driving the diffuse auroral activity.

Although the diffuse aurora is sub-visual, the net global energy input into the atmosphere due to the precipitation of energetic electrons (and to a lesser extent ions) is substantially larger than that associated with the localized discrete auroral arcs. The global pattern of precipitation can dramatically change the ionospheric conductivity, which can in turn influence the global pattern of magnetospheric convection. Diffuse auroral precipitation therefore provides a strong coupling mechanism between the magnetosphere and the ionosphere, which needs to be included in the development of the Geospace Global Circulation Model (GGCM). The microphysical processes that are responsible for precipitation also provide a coupling to the macroscopic convective flow within the system. The system is highly nonlinear, since the convective flow is responsible for injecting plasma sheet particles, which provide the source for plasma waves that ultimately cause the diffuse auroral precipitation.

It is generally accepted that the central plasma sheet electrons of ~100 eV–10 keV are the dominant source population for the diffuse aurora (e.g., Lui et al. 1977; Meng et al. 1979) and that the occurrence of the diffuse aurora is a result of pitch angle scattering of plasma sheet electrons into the loss cone by resonant wave-particle interactions (e.g., Kennel and Petschek 1966; Kennel 1969; Swift 1981; Kennel and Ashour-Abdalla 1982; Fontaine and Blanc 1983; Coroniti 1985; Davidson 1985; Inan et al. 1992; Schulz 1998). Both electrostatic electron cyclotron harmonic (ECH) waves and electromagnetic whistler-mode chorus waves can resonate with electrons in this energy range (Anderson and Maeda 1977). In addition, both of these two wave modes have the global morphology and the dependence on geomagnetic activity similar to those for the diffuse aurora, as observed from space (Meredith et al. 2009; Thorne et al. 2010). As a consequence, scattering by chorus and ECH waves have been long proposed as underlying mechanisms responsible for plasma sheet electron precipitations. However, which of these two main mechanisms is more influential in the production of diffuse aurora has remained a subject of controversy for over 40 years (e.g., Kennel et al. 1970; Lyons 1974a; Belmont et al. 1983; Johnstone et al. 1993; Villalón and Burke 1995; Meredith et al. 2000, 2009; Horne and Thorne 2000; Horne et al. 2003; Ni et al. 2008; Samara et al. 2010). It is of primary importance to comprehensively understand the mechanisms for the diffuse aurora. But only recently, a number of significantly improved studies, which combined data analyses, numerical simulations, and theoretical interpretations, have been able to uncover the mystery of the major origins that dominate the occurrences of the diffuse aurora and its global distribution.

In this paper we will perform a historical review of studies on the Earth's diffuse aurora, including recent advances on understanding its origins in which resonant wave-particle interactions play a fundamental and critical role. The outline of this paper is as follows. A brief description of resonant wave-particle interactions is given in Sect. 2, followed by Sect. 3 with discussions of magnetospheric plasma waves, which focus on whistler-mode chorus,

electrostatic ECH waves, and electromagnetic ion cyclotron (EMIC) waves that can either resonate with plasma sheet electrons or protons to drive the diffuse auroral precipitation. Formulations of quasi-linear diffusion coefficient evaluations and computed particle scattering rates due to the above three wave modes are presented in Sect. 4. Numerical results and quantitative comparisons with observations are described in Sect. 5 to elaborate the recently improved understanding of the major wave origins of different types of the diffuse aurora (nightside electron diffuse aurora, dayside electron diffuse aurora, pulsating aurora, and proton aurora). The respective contributions of chorus, ECH emissions, and EMIC waves are intensively reviewed and evaluated. We finish in Sect. 6 with a summary of the recent advances and outstanding questions regarding the formation of the diffuse aurora, and suggestions for future research as well.

2 Resonant Wave-Particle Interactions

Trapped particles in the Earth's magnetosphere undergo three types of quasi-periodic motions: gyration around magnetic field lines, bounce motion between the mirror points, and azimuthal drift around the Earth. Each periodic motion is associated with an adiabatic invariant. The first adiabatic invariant, μ, is associated with a gyromotion of a particle in the guiding center reference frame and derived from the Hamilton-Jacobi theorem. If the magnetic field changes over a gyro-period are small, then μ is conserved. The invariant associated with the bounce motion is J, which is the integral of the parallel momentum over one bounce between mirror points. Another parameter, denoted by K, is frequently used when discussing the second adiabatic invariant. K is a geometric characteristic as a combination of both J and μ, which is independent on the particle mass and charge. Primarily due to the gradient-B drift and field line curvature drift, the particle drift motion leads to the longitudinal drift in the magnetosphere, which produces the third and last adiabatic invariant, the flux invariant (denoted with Φ). This invariant states that the total geomagnetic flux enclosed by a drift orbit is constant so long as the magnetic field does not change on timescales faster than a drift period. Note that some of the diffuse auroral particles do not undergo periodic drifting motion and therefore are not associated with the third adiabatic invariant. Figure 4 illustrates the three characteristic particle motions associated with the adiabatic invariants in the Earth's magnetosphere.

When the ambient electric and magnetic field forces vary on a timescale comparable to the characteristic period of a particle motion, the corresponding invariant is violated. In addition, spatial variations of the force field that are abrupt on a length scale comparable to the gyroradius can also violate adiabatic invariants (Schulz and Lanzerotti 1974). Particle precipitation into the atmosphere is generally associated with the violation of the first

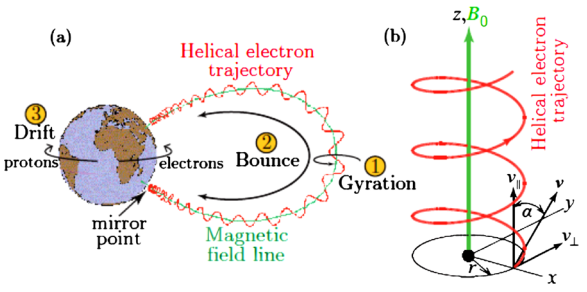

Fig. 4 Adapted from Fig. 2.7 of Walt (1994). Illustration of the three types of periodic motion experienced by electrons in the geomagnetic field: gyration about the field lines, bounce between North and South hemisphere, and longitudinal drift around the Earth

adiabatic invariant, so that pitch angle diffusion can occur and those initially trapped particles can approach and enter into the loss cone angle for atmospheric loss. The process of pitch angle diffusion can affect particle distributions, lead to plasma instabilities, and enhance the realistic precipitation to the ionosphere. Two collisionless scattering mechanisms have been proposed: one is the wave-particle interaction; the other is chaotic scattering in an inhomogeneous magnetic field. The main distinction between these two mechanisms is that wave-particle scattering is limited by the wave intensity, while chaotic scattering only depends on the magnetic field inhomogeneity and particle energy.

The parameter that controls the degree of chaotic scattering is $\kappa = R_c/\rho$, where R_c is the field line radius of curvature at the equator, ρ is the particle gyroradius at the equator. The critical value corresponding to a transition from the weakly scattering condition to a strongly scattering condition is $\kappa = 8$ (e.g., Birmingham et al. 1968; Imhof et al. 1979; Sergeev et al. 1983). Chaotic scattering in the equatorial current sheet of the magnetotail plays a crucial role in determining the scattering rates of energetic protons into the loss cone and resultant proton auroral precipitation, during both active and quiet geomagnetic conditions (Sergeev et al. 1983; Gilson et al. 2012). Due to the much smaller gyroradius of plasma sheet electrons (the energy range of interest is ~0.1–10 keV) compared to the field line curvature radius, the precipitation of diffuse auroral electrons is primarily attributed to wave-particle interactions. As a fundamental process in the Earth's magnetosphere, wave-particle interactions, which couple waves and particles, can lead to wave growth/damping and particle diffusion, and consequently modify the dynamics of the plasma environment. When the wave frequency matches the characteristic frequency of one of the particle's periodic motions, the corresponding adiabatic invariant can be violated and particle diffusion in phase space can take place from higher to lower phase space density regions due to the random exchange of energy between waves and particles. Through such a resonance, particle populations with unstable velocity space densities (exhibiting a gradient in the direction of constant energy in the wave's frame of reference) can efficiently interact with plasma waves, leading to wave growth or damping. For a charged particle with a given kinetic energy and pitch angle, the full gyroresonance condition requires

$$\omega - kv\cos\theta\cos\alpha = \frac{N\Omega_\sigma}{\gamma}, \quad N = 0, \pm 1, \pm 2 \ldots \tag{2.1}$$

where ω is the wave frequency, k is the wave number, θ is the wave normal angle with respect to the ambient magnetic field B_0, v is the particle velocity, α is the particle pitch angle, $\Omega_\sigma = qB_0/m_\sigma$ is the non-relativistic particle gyrofrequency for the particle species σ of charge q and rest mass m_σ (note that Ω_σ contains the sign of the charge), and $\gamma = (1 - v^2/c^2)^{-1/2}$ is the Lorentz factor (c is the speed of light). Physically, Eq. (2.1) means that wave-particle resonance occurs, i.e., a particle interacts most strongly with the waves, when the Doppler-shifted wave frequency experienced by the particle equals a multiple of its gyrofrequency. Landau resonance ($N = 0$) occurs when the particle travels along the ambient magnetic field with the wave parallel phase speed. For the diffuse auroral source population, since their energies are relatively low, the relativistic effect can be reasonably ignored to yield a reduced form of Eq. (2.1),

$$\omega - kv\cos\theta\cos\alpha = N\Omega_\sigma. \tag{2.2}$$

Gyroresonant interactions lead to particle diffusions in pitch angle and/or energy, potentially resulting in wave amplification or damping. Whether a wave mode grows or is damped is determined by the behavior of the particle distribution function near the resonant

velocity, defined by Eq. (2.1). For the interaction with a wave mode of a particular ω and $k_{||}(= k\cos\theta)$, diffusion curves (e.g., Gendrin 1981; Walker 1993; Summers et al. 1998), along which the particles are constrained to move during resonant scattering, can be easily found in the velocity space, i.e. ($v_{||} = v\cos\alpha$, $v_\perp = v\sin\alpha$). In the relativistic regime, by defining two-dimensional variables, $x = \omega/\Omega_\sigma$, $y = kc/\Omega_\sigma$, and $\beta = v/c$, Eq. (2.1) gives

$$y = \frac{x - N/\gamma}{\beta\cos\theta\cos\alpha}. \tag{2.3}$$

When $N \neq 0$, replacing γ by $(1-\beta^2)^{-1/2}$ produces an elliptic equation in the form

$$\left[\beta_{||} - \frac{xy\cos\theta}{(y\cos\theta)^2 + N^2}\right]^2 + \frac{N^2}{(y\cos\theta)^2 + N^2}\beta_\perp^2 = \frac{(xy\cos\theta)^2 - [(y\cos\theta)^2 + N^2](x^2 - N^2)}{[(y\cos\theta)^2 + N^2]^2}, \tag{2.4}$$

where $\beta_{||} = \beta\cos\alpha$ and $\beta_\perp = \beta\sin\alpha$. Equation (2.4) describes that relativistic resonant diffusion follows an elliptic curve with the major axis parallel to the $v_\perp$ axis and the minor axis coincident with the $v_{||}$ axis. For given parameters of wave information, by setting $\beta_\perp = 0$, minimum resonant energy can be evaluated from

$$E_{\min} = \left[\left(1 - (\beta_{||})_{\min}^2\right)^{-1/2} - 1\right] m_\sigma c^2, \tag{2.5}$$

with $(\beta_{||})_{\min}$ taking the smaller value of

$$(\beta_{||})_{\min} = \frac{xy\cos\theta \pm \sqrt{(xy\cos\theta)^2 - [(y\cos\theta)^2 + N^2](x^2 - N^2)}}{(y\cos\theta)^2 + N^2}. \tag{2.6}$$

In contrast, the non-relativistic resonant diffusion curve satisfies (e.g., Summers et al. 1998)

$$\left(\beta_{||} - \frac{\omega}{ck_{||}}\right)^2 + \beta_\perp^2 = \text{const}, \tag{2.7}$$

which means that in the wave rest frame, moving parallel to the magnetic field with phase speed $\omega/k_{||}$, the particle kinetic energy is conserved.

The preferential direction for diffusion along this "diffusion surface" or "resonance ellipse" is dictated by the gradient in phase space density (PSD) along this surface. The net energy and pitch angle diffusion direction can thus be obtained by analyzing the particle diffusion direction relative to constant energy curves in velocity space (e.g., Gendrin 1981). Wave instability is often associated with anisotropic particle distributions, with a temperature anisotropy ($T_\perp > T_{||}$) or loss cone feature, both of which exhibit such gradients along the diffusion surfaces for interactions with specific wave modes.

3 Magnetospheric Distributions of Whistler-Mode Chorus, Electrostatic Electron Cyclotron Harmonic (ECH) Waves, and Electromagnetic Ion Cyclotron (EMIC) Waves

For diffuse auroral electrons at energies of 100's eV–10 keV, electrostatic ECH waves and electromagnetic whistler-mode chorus waves are two major candidates that can resonantly

interact with them. In contrast, EMIC waves play an essential role in pitch angle scattering magnetospheric protons at energies of ~1 keV–100 keV. This section will focus on these three wave modes to give an overall description of their magnetospheric distributions, which have important implications for improved understanding of the diffuse auroral precipitation pattern.

3.1 Whistler-Mode Chorus Waves

Among the most intense electromagnetic emissions in the terrestrial environment, whistler-mode chorus waves are observed in the Earth's magnetosphere, predominantly in the low-density region outside the plasmasphere, over a broad range of local times (2200–1300 MLT). Chorus waves occur characteristically in two frequency bands, a lower band ($0.05–0.5\,f_{ce}$) (where f_{ce} is equatorial electron gyrofrequency) and an upper band ($0.5–0.8\,f_{ce}$) with a minimum wave power near $0.5\,f_{ce}$ (Tsurutani and Smith 1974; Burtis and Helliwell 1976; Koons and Roeder 1990; Meredith et al. 2001).

Observationally, whistler-mode chorus usually consists of discrete elements with rising or falling tones and sometimes short impulsive bursts (e.g., Burtis and Helliwell 1969; Burton and Holzer 1974; Hayakawa et al. 1984; Santolík et al. 2003; Li et al. 2011d). Burtis and Helliwell (1976) showed that rising tones, falling tones, constant frequency tones, and hooks were observed respectively with a ratio of 77 %, 16 %, 12 %, and 5 % of the samples. Hayakawa et al. (1990) reported that on the nightside, chorus waves of various structure types are observed, including falling tones, constant frequency tones and normal rising tones, whereas on the dayside, normal rising tones and impulsive (or burstlike) emissions are mainly observed. Using near-midnight passes of OGO 5 data within 5° of the magnetic equator, Goldstein and Tsurutani (1984) showed that the majority of chorus waves including rising and falling tones propagate within 20° of the magnetic equator. Burton and Holzer (1974) reported that the wave normal angles of typical rising tones were less than 20°, which was further quoted as 5°–20° by Hayakawa et al. (1984). Using wave observations from the Cluster spacecraft, Santolík et al. (2009) performed a case of oblique falling tone chorus close to the resonance cone. Li et al. (2011d) investigated the typical properties of rising and falling tone lower band chorus waves, based upon a statistical survey of THEMIS wave burst data between 1 June 2008 and 1 April 2011. Figure 5 shows the occurrence rates of chorus magnetic wave amplitude and wave normal angle for rising (top) and falling (bottom) tones, respectively. The occurrence rate of rising tone wave amplitude typically peaks for 30–100 pT (~45 %) with ~2 % occurrence for extremely large amplitude (>300 pT). However, magnetic wave amplitudes of falling tones are much weaker, typically less than 30 pT. Falling tones are observed from midnight to noon, while rising tones extend further into afternoon. For rising tones, the occurrence rate is higher at lower latitude on the nightside, while little latitudinal dependence is shown on the dayside. For falling tones, a low occurrence rate is observed on the nightside, and the largest occurrence rate is observed on the dayside at higher latitude (>10°). A number of previous studies have successfully simulated the occurrences of rising tone elements (e.g., Nunn et al. 1997; Katoh and Omura 2007; Omura et al. 2008). Recently, Soto-Chavez et al. (2014) presented a new model to explain the occurrence of the falling tone chorus. They proposed that falling tone chorus starts as a marginally unstable mode, which subsequently produces phase space structures that release energy and trigger wave chirping. Further work is required to better understand the generation and nonlinear evolution of falling tone chorus.

Chorus emissions are largely controlled by geomagnetic substorm activity and intensify when substorm activity is enhanced (Tsurutani and Smith 1977; Meredith et al. 2001).

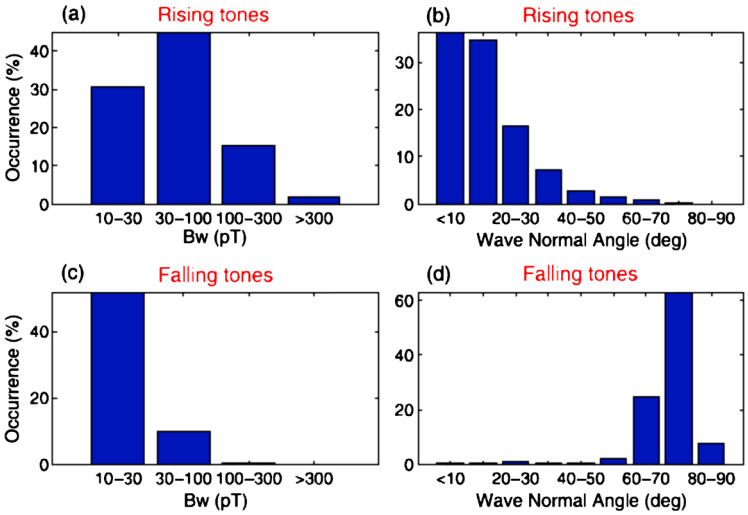

Fig. 5 Adapted from Fig. 3 of Li et al. (2011d). (**a**) and (**b**) the occurrence rate of chorus wave amplitude and wave normal angle for rising tones. (**c**) and (**d**) the same parameters for falling tones

Generally believed to be generated near the geomagnetic equator, typical chorus amplitudes lie in the range of 1–100 pT (Burtis and Helliwell 1975; Meredith et al. 2003a; Li et al. 2009), however, amplitudes of ∼1 nT or above have been reported during intense geomagnetic activity (Parrot and Gaye 1994; Cattell et al. 2008; Cully et al. 2008). Large amplitude chorus has recently received more attention due to its pronounced nonlinear interaction with energetic electrons (e.g., Albert 2002; Bortnik et al. 2008). Bortnik et al. (2008) demonstrated that low amplitude waves exhibit quasi-linear scattering, which leads to large-scale diffusive behavior, whereas large amplitude waves can result in monotonic decreases in pitch angle and energy, causing large-scale de-energization and particle loss. It is worthwhile to note that despite the potential significance of non-linear wave-particle interactions, the recent study of Thorne et al. (2013a) has showed that quasi-linear theory can accurately describe the acceleration to radiation belt energies, which tends to contradict the conclusions of the above simulations that non-liner scattering is required for accurate simulations of the radiation belts. Using high-resolution waveform data from THEMIS, Li et al. (2011a) performed a statistical analysis of the global distribution of wave amplitudes for lower band and upper band chorus. They found that wave amplitudes of both lower and upper band chorus are activity-dependent, generally having larger wave amplitudes during periods of stronger magnetic activity. Chorus wave amplitudes show a particularly close relation with AE^* (maximum AE during the previous 3 h) on the nightside, where chorus generation is directly related to substorm injection or enhanced convection. In contrast, dayside chorus waves are present >10 % of the time at $L > 7$ and can persist even during periods of low geomagnetic activity. As shown in Fig. 6, for lower band chorus, large amplitude (>300 pT) waves are typically observed from premidnight to postdawn near the magnetic equator with an occurrence rate up to a few percent, whereas weaker chorus extends through the noon to the dusk sector. In addition, large amplitude chorus is preferentially observed at lower L shells (<8) with much smaller probability. The properties of upper band chorus are somewhat different. Upper band chorus is considerably weaker in magnetic wave amplitudes, shows tighter confinement to the magnetic equator (<10°), and occurs at $L < 8$. On average, upper band chorus is stronger on the nightside than on the dayside. Observations also

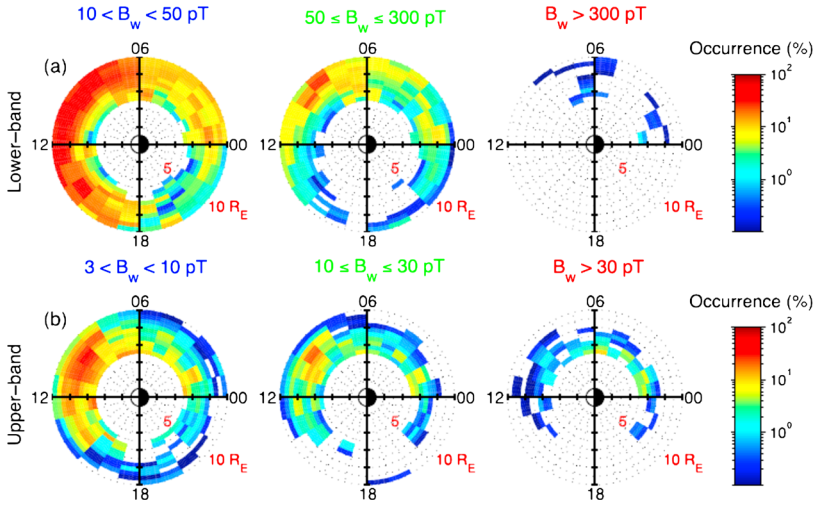

Fig. 6 Adapted from Fig. 3 of Li et al. (2011a). Global distribution of the occurrence rate of (**a**) lower band chorus and (**b**) upper band chorus for modest, strong, and large amplitude waves from THEMIS FFF data, shown in the L-MLT domain with a bin size of $0.5L \times 1$ MLT

show that characteristically nightside (22–06 MLT) chorus is predominantly confined to magnetic latitudes within 15° of the equator, while dayside (06–13 MLT) chorus can propagate to much higher latitudes due to weaker Landau damping (Tsurutani and Smith 1974; Meredith et al. 2001; Horne et al. 2005; Bortnik et al. 2007; Li et al. 2009).

Wave normal angle distribution is another essential ingredient of the properties of chorus waves (Shprits and Ni 2009; Ni et al. 2011d). Using OGO 5 wave measurements, Burton and Holzer (1974) and Goldstein and Tsurutani (1984) found that equatorial lower band chorus waves mainly have wave normal angles <20°. Goldstein and Tsurutani (1984) also found a small concentration of wave normal angles near the Gendrin angle in the frequency range of 0.3–0.45 fce. Combining the Cluster wave measurements and ray tracing modeling, Breneman et al. (2009) reported that near the magnetic equator, lower band chorus is preferentially excited with wave normal angles either within 20° of the ambient magnetic field or near the Gendrin angle. They also found that wave normal angles become more oblique as waves propagate from the equator toward higher latitudes, consistent with ray tracing results of whistler mode chorus waves. Later, using wave data from the Polar spacecraft, Haque et al. (2010) found that lower band chorus waves with wave normal angles less than 20° have the highest occurrence rate, with a secondary peak occurring near the Gendrin angle, in the latitude range of 10°–50°. Santolík et al. (2009) showed very oblique lower band chorus waves falling in frequency, with wave normal angles close to the resonance cone. Using THEMIS FFF datasets, Li et al. (2011d) found that rising tone chorus is typically quasi field-aligned, while falling tone chorus is predominantly very oblique, with wave normal angles typically larger than 60°. Studies of upper band chorus waves indicate that their wave normal angles can vary from essentially field-aligned (Hospodarsky et al. 2001; Lauben et al. 2002) to highly oblique with wave normal angles close to the resonance cone (Hayakawa et al. 1984; Muto et al. 1987). Breneman et al. (2009) reported that upper band chorus is generally found at relatively larger wave normal angles between 30° and 40°. Haque et al. (2010) showed that for upper band chorus, 50 % of the wave normal angles at latitudes near the magnetic equator have values less than 10°, whereas the wave normal angles are close to the reso-

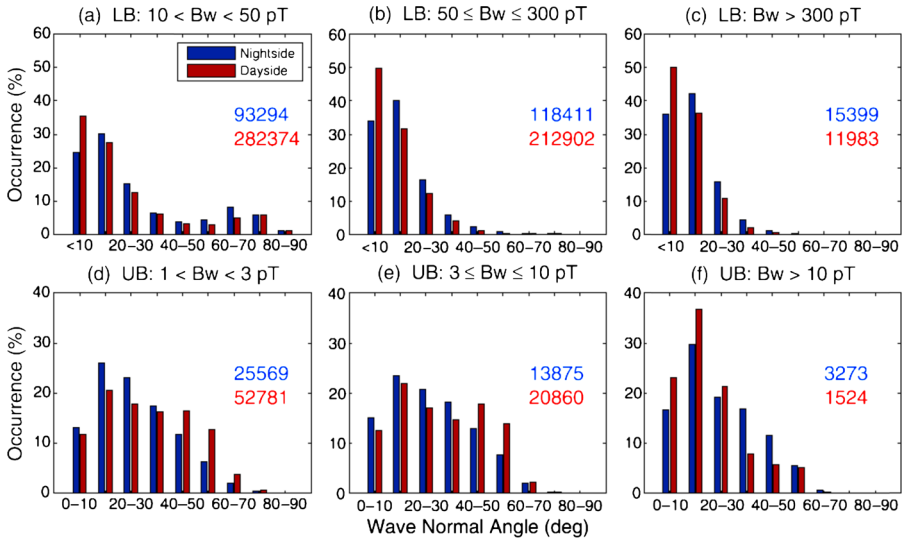

Fig. 7 Adapted from Fig. 6 of Li et al. (2011a). (**a**)–(**c**) Occurrence rates of various wave normal angles for different levels of wave amplitudes on the nightside (*blue*) and the dayside (*red*) for lower-band chorus. (**d**)–(**f**) Parameters as in (**a**)–(**c**) but for upper-band chorus. The numbers in each plot indicate the total number of chorus events collected from the nightside (*blue*) and the dayside (*red*), which are used to calculate the occurrence rate in each corresponding category

nance cone for some other cases. A further study of Li et al. (2011a), based on a THEMIS FFF data survey, found that for lower band chorus, strong waves (>50 pT) tend to have small wave normal angles <20° (Fig. 7). In contrast, for modest waves, the wave normal angles are distributed over a broad range with a major peak at <20° and a small secondary peak at 60°–80°. The wave normal angles are generally smaller on the dayside than on the nightside. Furthermore, the wave normal angles of upper band chorus are generally larger than those of lower-band chorus, ranging from field-aligned to very oblique. For strong upper band chorus, however, the occurrence rate of wave normal angles still peaks at <20° at lower magnetic latitudes, possibly due to stronger Landau damping.

Combined with the local condition of plasma density and ambient magnetic field and propagation angle, the spectral distribution of chorus is required to determine the range of resonant electron energies and the resulting diffusion coefficients. However, statistics of spectral properties are sparse, particularly in the off-equatorial magnetosphere. Using the CRRES wave data, Meredith et al. (2009) performed a statistical analysis of the spectral distribution of equatorial upper band chorus within 3° of the geomagnetic equator for the afternoon (12–18 MLT), evening (18–24 MLT) and morning (00–06 MLT) sectors at the spatial coverage of $L = 3.0$–6.5, corresponding to three (quiet, moderate, and active) geomagnetic conditions. They concluded that upper band chorus power peaks in the range $0.5 f_{ce} < f < 0.6 f_{ce}$ during geomagnetically active conditions typically from $L = 4.0$ to $L = 6.0$, and in the evening sector decreases with increasing frequency. To further investigate the spectral extent of chorus waves in terms of the normalized chorus frequency (with respect to the minimum field line gyrofrequency, Ω_{min}), Bunch et al. (2013) adopted a database of chorus observations from the Polar spacecraft, the orbits of which result in observations confined to the spatial extent of MLT = 0–24, magnetic latitudes <65°, and $R_0 = 3$–11 (where R_0 is the radial distance of equatorial field line crossing). As shown in

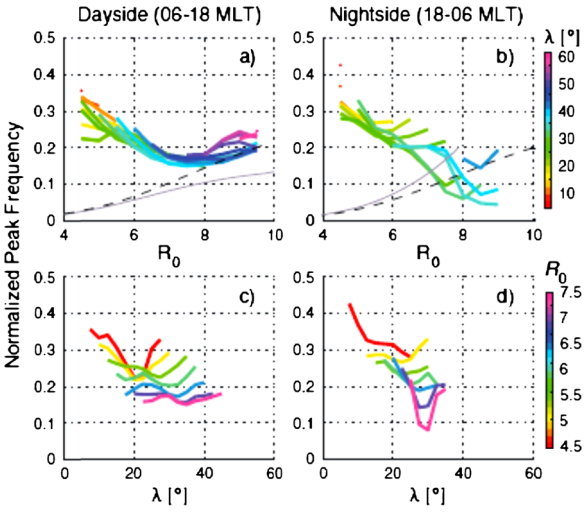

Fig. 8 Adapted from Fig. 2 of Bunch et al. (2013). Chorus normalized peak frequency (Ω_m) as a function of equatorial radial distance (R_0) and magnetic latitude (λ), obtained by a survey using the wave observations from the Polar spacecraft

Fig. 8, they found that on average the chorus spectrum peaks in the range of 0.1–0.4$\Omega_{\min}$ and that the normalized chorus peak frequency varies significantly with magnetic latitude, R_0, and MLT, i.e., decreasing with increasing R_0 and with increasing latitudes $<\sim 25°$. The normalized bandwidths of chorus determined by Gaussian fits to the expectation values of the power spectrum range from 0.04 to 0.09 ($\sim$0.07 on average), which are lower than the widely adopted value of 0.15 used in most diffusion codes, and on the low end of values 0.07–0.13 reported by Ni et al. (2011c) based on the CRRES wave measurements.

3.2 Electrostatic Electron Cyclotron Harmonic (ECH) Waves

ECH waves are electrostatic emissions observed in bands between the harmonics of the electron gyrofrequency, f_{ce}, and sometimes referred to as $(n + 1/2) f_{ce}$ waves since they tend to be observed in narrow bands close to odd integral half-harmonics of the electron gyrofrequency (e.g., Kennel et al. 1970; Fredricks and Scarf 1973; Shaw and Gurnett 1975). First reported by Kennel et al. (1970) from OGO-5 data, these electrostatic emissions have been detected at all local times and at all the latitudes up to $\sim$45° (Fredricks and Scarf 1973; Shaw and Gurnett 1975), and found over a wide range of geocentric distances of 4–12R_e (Kennel et al. 1970; Roeder and Koons 1989). Furthermore, it has been established that the most intense emissions occur over the evening to dawn sector (21–06 MLT) at $4 < L < 8$ and are confined to within a few degrees of the magnetic equator (Gough et al. 1979; Roeder and Koons 1989; Paranicas et al. 1992).

Typical amplitudes reported from OGO-5 observations were very large, ranging from 1 to 10 mV/m and occasionally as high as 100 mV/m (Kennel et al. 1970). Therefore, Kennel et al. (1970) suggested for the first time that ECH waves could provide a mechanism for pitch angle diffusion and turbulent energization of auroral zone electrons with energies from a few hundred eV to several keV, which was later quantified by Lyons (1974a). However, the effectiveness of ECH scattering was challenged by Belmont et al. (1983) who pointed out that the stronger ECH events (>1 mV/m) occur less than 2 % of the time compared to 88 % occurrence of much weaker electric fields (<0.1 mV/m), based on a statistical analysis of the GEOS-2 data within the 22–06 MLT sector and 3° of the geomagnetic equator. A later statistical study by Roeder and Koons (1989) of plasma wave data from the AMPTE IRM

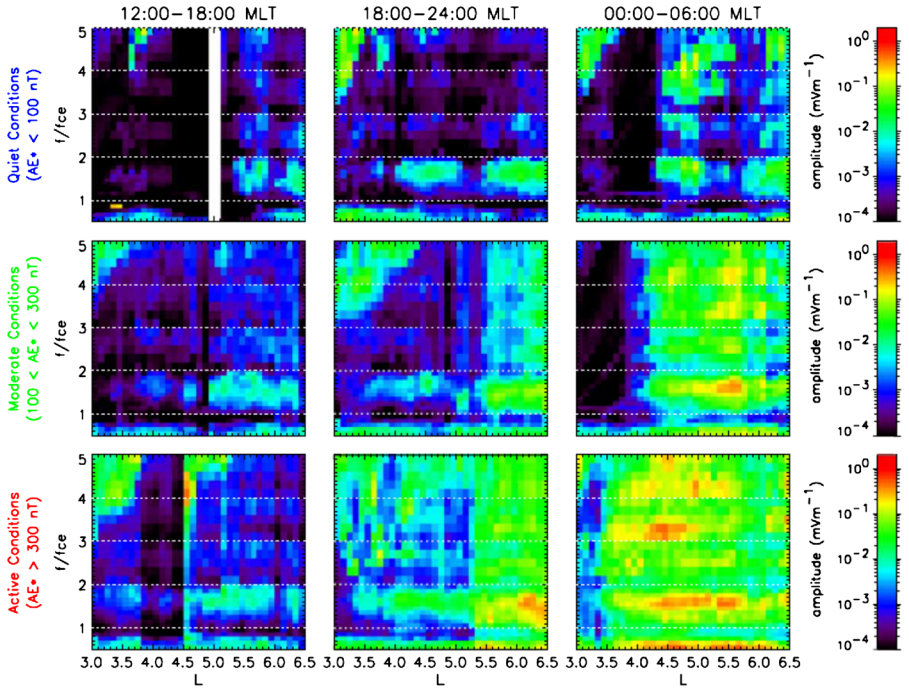

Fig. 9 Adapted from Fig. 5 of Meredith et al. (2009). Average equatorial ($-3° < \lambda < 3°$) wave amplitudes as a function of frequency and L, using the CRRES wave data. The results are shown for, *from left to right*, the afternoon (1200–1800 MLT), evening (1800–2400), and morning (00–06 MLT) sectors for, *from top to bottom*, quiet (AE* < 100 nT), moderate (100 < AE* < 300 nT), and active (AE* > 300 nT). *In each panel*, the local gyrofrequency and its harmonics are plotted as *dashed lines*

and SCATHA satellites indicated that the occurrence of ECH wave emissions is comparable to that reported by Belmont et al. (1983) and that ECH emissions are observed most often in the 03–06 local time (LT) sector of the magnetosphere at geocentric distances of 4–8R_e, confined to $\pm 10°$ off the magnetic equator. The work of Roeder and Koons (1989) covered a broad L-shell range (4–20) and most local times, but only four equal L-shell bins and eight evenly spaced local time bins were adopted. In addition, their analysis did not differentiate between various latitudes within $\pm 10°$.

Paranicas et al. (1992) used the CRRES wave data to study the properties of banded electrostatic emissions above f_{ce}, which presented results similar to those of Belmont et al. (1983) and Roeder and Koons (1989). It is Meredith et al. (2009) that performed a comprehensive survey of ECH waves using the entire 15-month CRRES wave data, the results of which are presented in Fig. 9. They reported that ECH waves intensify with increasing geomagnetic activity and are more intense in the evening sector (00–06 MLT). During active periods, strong ECH waves with amplitudes >1 mV/m were observed within $\pm 3°$ of the magnetic equator at $L = 4$–7 from 21 to 06 MLT approximately 20 % of the time. For each level of activity, there is a tendency for the ECH waves in the first harmonic band to become stronger and peak lower in the band at higher L. ECH wave emissions in the first harmonic band maximize near the center of the band in the frequency range $1.4\,f_{ce} < f < 1.8\,f_{ce}$. ECH emissions are present but weaker in the second harmonic band, while in the higher harmonic bands the emissions maximize low in the band and are associated with periods when the upper hybrid frequency lies in the band. However, the CRRES data coverage is mostly confined

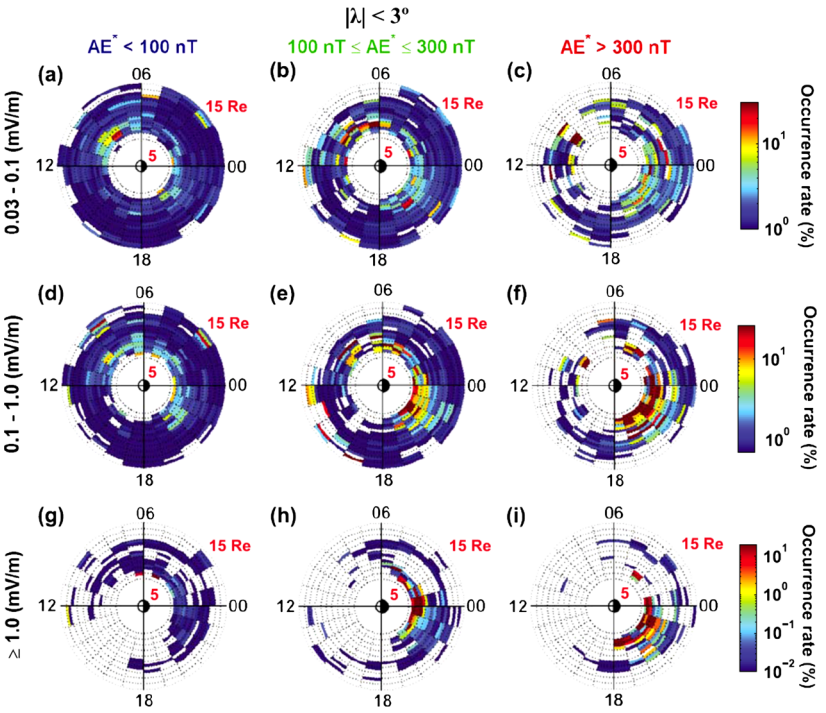

Fig. 10 Adapted from Fig. 2 of Ni et al. (2011b). Global occurrence rates of ECH waves within $|\lambda| < 3°$ under different geomagnetic conditions (*from left to right*: quiet, moderate, and active) for three different wave amplitude levels: (**a**), (**b**), (**c**) relatively weak with 0.03 mV/m $\leq E_w <$ 0.1 mV/m, (**d**), (**e**), (**f**) moderate with 0.1 mV/m $\leq E_w <$ 1 mV/m, and (**g**), (**h**), (**i**) strong with $E_w \geq$ 1 mV/m, obtained from a survey of THEMIS Filter Bank (FBK) wave data

within $7R_e$ with a pronounced gap in the pre-noon sector for $L > 5$. Using THEMIS Filter Bank (FBK) wave data for two years (2008–2009), Ni et al. (2011b) conducted a detailed statistical analysis of ECH waves to examine the global distribution of averaged ECH electric field amplitude and its occurrence rate as a function of L-shell, MLT, magnetic latitude, and geomagnetic activity level. As shown in Fig. 10, their results confirmed the high occurrence of <1 mV/m ECH emissions throughout the outer magnetosphere ($L > 5$). Relatively weak (0.03–0.1 mV/m) ECH waves exhibit an occurrence rate up to ∼40 %. The occurrence rates of moderate (0.1–1 mV/m) and strong (≥1 mV/m) ECH waves have a pronounced MLT asymmetry. The strongest (≥1 mV/m) ECH waves are enhanced during geomagnetically disturbed periods, and are mainly confined close to the magnetic equator ($|\lambda| < 3°$) over the region $L \leq 10$ in the night and dawn MLT sector. ECH wave intensities within $3° \leq |\lambda| < 6°$ are generally much weaker but not negligible, especially for $L <$ ∼12 on the midnight side.

In principle, ECH waves propagate at very large angles with respect to the ambient magnetic field, e.g., ∼90° (e.g., Gurnett and Bhattacharjee 2005). ECH waves are generally thought to be driven by a loss cone instability of the source electron velocity distribution (e.g., Young et al. 1973; Ashour-Abdalla and Kennel 1978; Horne 1989; Horne et al. 2003). The occurrence rate of ECH waves with different wave amplitudes under various geomagnetic activity levels revealed in existing studies suggests that triggering of ECH waves does not necessarily require dramatic intensification of geomagnetic activity, supporting the idea that a loss cone distribution (which is present under most circumstances)

is the major mechanism for ECH wave generation. However, the disturbed conditions associated with enhanced convection and/or substorm activity can lead to ECH wave amplification (Zhang and Angelopoulos 2014), as a consequence of more dipolarized magnetic field configuration (Zhang et al. 2014) and/or increased free energy in the electron loss cone distribution, which requires further theoretical investigation.

3.3 Electromagnetic Ion Cyclotron (EMIC) Waves

The importance of EMIC waves to the magnetospheric particle dynamics has been long recognized, since they are capable of causing thermal plasma heating (e.g., Thorne and Horne 1992, 1997; Zhang et al. 2010, 2011) and also driving losses of both ring current protons (e.g., Cornwall et al. 1970; Summers 2005; Liang et al. 2014) and relativistic electrons (e.g., Thorne and Kennel 1971; Summers and Thorne 2003; Summers et al. 2007; Ma et al. 2015; Ni et al. 2015) via resonant pitch angle scattering. EMIC wave-driven scattering loss of magnetospheric protons is regarded as an effective candidate accounting for the occurrence of the proton aurora.

Propagating at frequencies below the proton gyrofrequency (f_{cp}), EMIC waves have been extensively observed in the inner magnetosphere in the frequency range of 0.1–5.0 Hz, i.e., the ultra-low-frequency (ULF) Pc1-2 band (e.g., Anderson et al. 1992a, 1992b; Fraser et al. 1992, 1996; Fraser and Nguyen 2001; Meredith et al. 2003b, 2014; Zhang et al. 2014). Partially controlled by the ion composition and anisotropy (e.g., Kozyra et al. 1984; Horne and Thorne 1994) and by the location with respect to the plasmapause (Fraser and Nguyen 2001), EMIC waves can be generated at three distinct frequency bands below the hydrogen (H^+), helium (He^+), and oxygen (O^+) ion gyrofrequencies. Compared to the frequently measured H^+-band and He^+-band EMIC waves, O^+-band EMIC waves are rarely observed but were recently reported in the outer plasmasphere at $L = 2$–5 from the Van Allen Probes EMFISIS and EFW data (Yu et al. 2015).

While EMIC waves are present during geomagnetically quiet periods, they can be more common and more intense during geomagnetic storms and substorms (Bräysy et al. 1998; Erlandson and Ukhorskiy 2001; Meredith et al. 2014). Observed over a broad range of L-shell from $L = 3$ to $L = 10$, EMIC waves have typical amplitudes in the range of ~0.1–10 nT (Fraser et al. 1996; Erlandson and Ukhorskiy 2001). These waves occur characteristically over a broad range of magnetic local time (MLT) from the post-noon to dawn side, approximately 14–07 MLT, with the maximum of occurrence probability in the afternoon sector (e.g., Meredith et al. 2003b; Min et al. 2012). Using the AMPTE CCE data, Anderson et al. (1992a) reported that the occurrence rate of intense EMIC waves (i.e., peak-to-peak amplitudes >0.8 nT) increases monotonically with L in the region $L = 3$–9, peaking at 10 %–20 % in the spatial region of 11–15 MLT within $L = 7$–9. Analyzing the THEMIS FGM data between May 2007 and December 2011 with an automated EMIC Pc1 wave detection algorithm, Usanova et al. (2012) investigated the occurrence rate of EMIC Pc1 waves as a function of L-shell, MLT, P_{dyn}, AE, and SYMH. They found that the dayside outer magnetosphere is a preferential location for EMIC activity, with the occurrence rate in this region being strongly controlled by solar wind dynamic pressure. High EMIC occurrence, preferentially at 12–15 MLT, is also associated with high AE. Specifically, EMIC wave occurrence rate increases with L in the dawn, noon, dusk, and midnight sectors, showing the highest occurrence rate (5 %–8 %) in the noon and dusk sectors and reaching its maximum at $L \sim 9$, as shown in Fig. 11. Such an MLT dependence of EMIC wave occurrence is consistent with the westward drift of energetic ions, which are commonly regarded as the free-energy source population for EMIC wave excitation. Usanova et al. (2012) also found

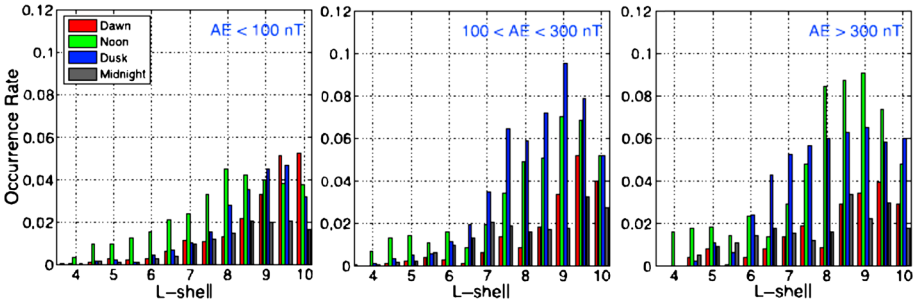

Fig. 11 Adapted from Fig. 9 of Usanova et al. (2012). EMIC wave event occurrence as a function of L for the dawn (*red*), noon (*green*), dusk (*blue*), and midnight (*black*) sectors and three ranges of AE (AE <100, 100 < AE < 300, and AE > 300 nT), obtained from the THEMIS observations

that P_{dyn} is a major factor affecting the occurrence of EMIC waves during quiet geomagnetic conditions, along with a ~15 % probability of observing dayside EMIC waves beyond geosynchronous orbit during increased P_{dyn} or positive SYMH (both are signatures of magnetospheric compression). Analysis of 26 magnetic storms with $D_{st} < 50$ nT showed that EMIC probability during the storm main phase is ~20 % (seen in only 6 out of 26 storms). For those storm events, EMIC waves were observed both outside and inside the geosynchronous orbit. While H^+-band EMIC waves are most common in the outer magnetosphere ($L = 7$–9) on the afternoon side regardless of geomagnetic activity, He^+-band EMIC waves occur most frequently in the inner magnetosphere ($L = 4$–7) on the prenoon to dusk side during active times (Keika et al. 2013).

Using THEMIS wave data from 2007 to 2010, Min et al. (2012) further studied the global distribution of EMIC waves in a broad range of the terrestrial magnetosphere. They found that there are two major peaks in the EMIC wave occurrence probability, i.e., one at dusk and 8–12 RE where the helium band dominates over the hydrogen band waves, and the other at dawn and 10–12 RE where the hydrogen band dominates over the helium band waves (left panels of Fig. 12). In terms of wave spectral power, the dusk EMIC wave events are stronger (≈10 nT^2/Hz) than the dawn events (≈3 nT^2/Hz); the average normalized wave frequency for the hydrogen band is relatively high (≈0.5 f_{cp}) at dawn and low (≈0.35 f_{cp}) at noon and dusk, while that for the helium band lies just below the helium ion gyrofrequency (≈0.17 f_{cp}) for most MLT values (right panels of Fig. 12). In addition, the hydrogen band waves at dawn are weakly left-hand polarized near the equator, become linearly polarized with increasing latitude and eventually weakly right-hand polarized at high latitudes whereas the helium band waves at dawn are linearly polarized at all latitudes. Dusk waves in both bands are strongly left-hand polarized over a wide range of latitudes. A statistical analysis of EMIC waves in the inner magnetosphere was conducted by Meredith et al. (2014) using CRRES wave measurements. They found that the average intensity of H^+-band and He^+-band EMIC waves in the region $L^* = 4$–7 (where L^* is the Roederer parameter related to the third adiabatic invariant (Roederer 1970)) in the afternoon sector under actively disturbed conditions is 0.5 nT^2 and 2 nT^2, respectively. Furthermore, Fig. 13 demonstrates that during active conditions the average peak frequency and width of the moderate and strong wave events ($B_W^2 > 0.1$ nT^2) in the afternoon sector, where the waves are most frequent, is 0.4 f_{cp} and 0.05 f_{cp} respectively for the H^+-band emissions, and 0.15 f_{cp} and 0.02 f_{cp} respectively for the He^+-band emissions.

Primarily generated by the anisotropic distribution of 1–100 keV ring current protons that are formed by the earthward ion convection from the magnetotail during geomagneti-

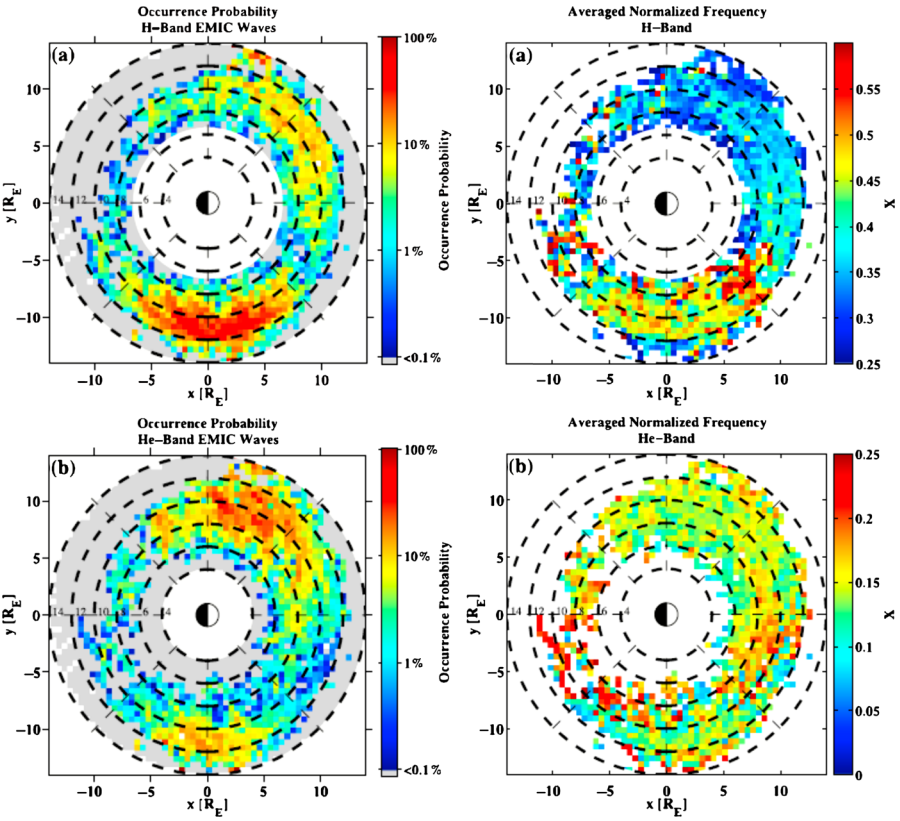

Fig. 12 Modified from Figs. 4 and 5 of Min et al. (2012). *Left*: EMIC wave occurrence probability for (**a**) H^+- and (**b**) He^+-band waves projected on the magnetic equatorial plane along the dipole magnetic field. The regions with occurrence probability less than 0.1 % are *colored gray*. *Right*: average normalized wave frequency, $X = f/f_{H^+}$, for (**a**) H^+- and (**b**) He^+-band waves. The THEMIS observations are adopted for the analysis

cally disturbed periods (e.g., Cornwall et al. 1970; Jordanova et al. 2001; Zhang et al. 2014), EMIC waves prefer to take place in the regions of high density either localized along the duskside plasmapause (e.g., Pickett et al. 2010) or within dayside drainage plumes (e.g., Morley et al. 2009). The compression of the magnetopause is suggested as another possible source of EMIC waves (e.g., McCollough et al. 2012). While it is frequently thought that EMIC emissions are generated along the field line at the equatorial source region particularly in the inner magnetosphere, information about the wave normal angle of EMIC waves is very limited. Anderson et al. (1992b) showed that near the equator the waves are a mixture ranging from left-hand circularly polarized waves to highly elliptical or linearly polarized waves, while at higher latitudes the waves become more linearly polarized. Such wave properties suggest that EMIC emissions can deviate from parallel or quasi-parallel propagation after the generation and become more oblique as they propagate to higher latitudes (Horne and Thorne 1994). Min et al. (2012) reported that at dawn EMIC waves emitted in the H^+-band have large normal angles ($>45°$) and the waves in the He^+-band have even larger normal angles ($>60°$) than the H^+-band waves, while at dusk waves are propagating with small normal angles ($\leq 30°$) and dominated by the He^+-band emissions.

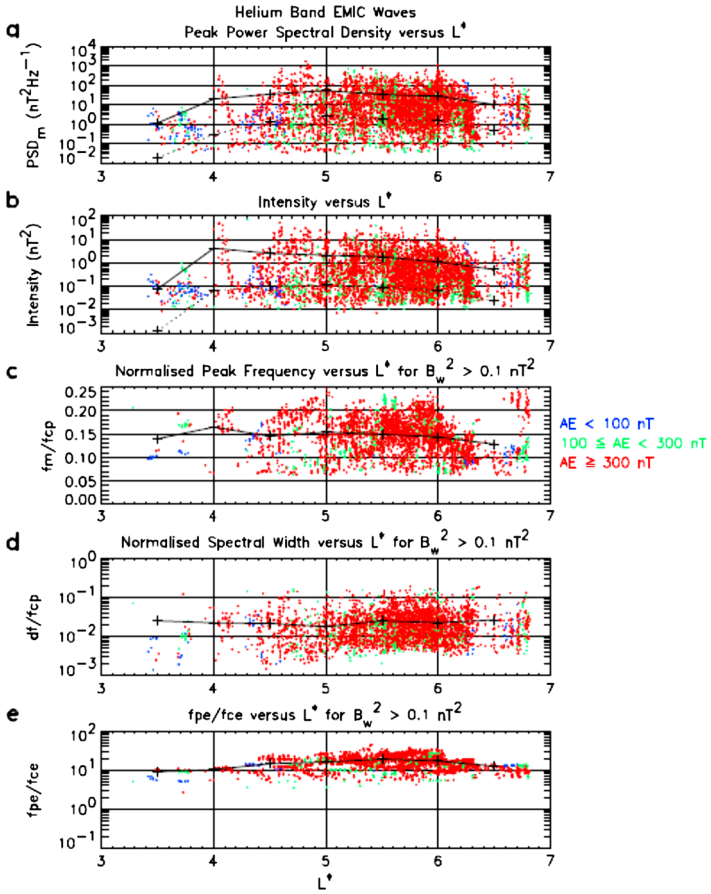

Fig. 13 Adapted from Fig. 9 of Meredith et al. (2014). Scatter plot of the spectral properties of the helium band EMIC waves and the ratio f_{pe}/f_{ce} as a function of L^* in the afternoon sector. (**a**) The power spectral density, (**b**) the intensity, (**c**) the normalized peak position, (**d**) the spectral width, and (**e**) the ratio f_{pe}/f_{ce}, color-coded according to the geomagnetic activity as monitored by the AE index. The CRRES observations are adopted for the analysis

4 Wave-Induced Rates of Particle Scattering

Detailed information of magnetospheric waves including the wave power spectral profile, the wave normal angle distribution, and the latitudinal extent provides the required basic inputs to quantify wave-induced scattering rates of magnetospheric particles, which can act as a feasible indicator of precipitation efficiency via pitch angle scattering by waves (e.g., Shprits et al. 2006a). Lyons (1974b) applied the quasi-linear diffusion theory of Kennel and Engelmann (1966) and derived general expressions for the resonant diffusion coefficients, valid for cyclotron resonance with any wave mode and any distribution of wave energy and wave normal angle. In quasi-linear theory the effects of wave diffusion on the particle distribution function are included by assuming particle scattering is stochastic and caused by a succession of small amplitude waves with random phase. Quasi-linear theory is expected to provide an effective overall description of the average properties of the diffusion process but omits particle trapping and highly nonlinear effects.

4.1 General Formulation for Quasi-linear Bounce-Averaged Diffusion Coefficients

Following Lyons et al. (1972), the general form for bounce-averaged quasi-linear diffusion coefficients in any ambient magnetic field can be written as

$$\langle D_{\alpha\alpha}\rangle = \frac{1}{\tau_B}\int_0^{\tau_B} D_{\alpha\alpha}(\alpha)\left(\frac{\partial\alpha_{eq}}{\partial\alpha}\right)^2 dt, \tag{4.1}$$

$$\langle D_{\alpha p}\rangle = \frac{1}{\tau_B}\int_0^{\tau_B} D_{\alpha p}(\alpha)\left(\frac{\partial\alpha_{eq}}{\partial\alpha}\right) dt, \tag{4.2}$$

$$\langle D_{pp}\rangle = \frac{1}{\tau_B}\int_0^{\tau_B} D_{pp}(\alpha) dt, \tag{4.3}$$

where $\langle D_{\alpha\alpha}\rangle$, $\langle D_{\alpha p}\rangle$ and $\langle D_{pp}\rangle$ are bounce-averaged rates of pitch-angle diffusion, (pitch-angle, momentum)-mixed diffusion and momentum diffusion, respectively, $D_{\alpha\alpha}$, $D_{\alpha p}$ and D_{pp} are local diffusion coefficients, α and α_{eq} are local and equatorial pitch-angle, respectively, and τ_B is the electron bounce period. For the geomagnetic field line that lies in a plane perpendicular to the magnetic equator plane, which is a good approximation under most geomagnetic conditions, Eqs. (4.1)–(4.3) can be rewritten as follows (e.g., Orlova and Shprits 2010; Ni et al. 2011e, 2012b)

$$\langle D_{\alpha\alpha}\rangle = \frac{\int_{\lambda_{m,s}}^{\lambda_{m,n}} \frac{D_{\alpha\alpha}(\alpha)}{\cos\alpha}\left(\frac{\tan\alpha_{eq}}{\tan\alpha}\right)^2\sqrt{r^2+\left(\frac{\partial r}{\partial\lambda}\right)^2}d\lambda}{\int_{\lambda_{m,s}}^{\lambda_{m,n}}\sec\alpha\sqrt{r^2+\left(\frac{\partial r}{\partial\lambda}\right)^2}d\lambda}, \tag{4.4}$$

$$\langle D_{\alpha p}\rangle = \frac{\int_{\lambda_{m,s}}^{\lambda_{m,n}} \frac{D_{\alpha p}(\alpha)}{\cos\alpha}\frac{\tan\alpha_{eq}}{\tan\alpha}\sqrt{r^2+\left(\frac{\partial r}{\partial\lambda}\right)^2}d\lambda}{\int_{\lambda_{m,s}}^{\lambda_{m,n}}\sec\alpha\sqrt{r^2+\left(\frac{\partial r}{\partial\lambda}\right)^2}d\lambda}, \tag{4.5}$$

$$\langle D_{pp}\rangle = \frac{\int_{\lambda_{m,s}}^{\lambda_{m,n}} \frac{D_{pp}(\alpha)}{\cos\alpha}\sqrt{r^2+\left(\frac{\partial r}{\partial\lambda}\right)^2}d\lambda}{\int_{\lambda_{m,s}}^{\lambda_{m,n}}\sec\alpha\sqrt{r^2+\left(\frac{\partial r}{\partial\lambda}\right)^2}d\lambda}, \tag{4.6}$$

where r is radial distance to the Earth's center, λ is magnetic latitude, and $\lambda_{m,s}$ and $\lambda_{m,n}$ are mirror latitude of particles on the southern and northern hemisphere, respectively. For the special case of a dipole field, the above equations of quasi-linear bounce-averaged diffusion coefficients reduce to (e.g., Glauert and Horne 2005; Shprits et al. 2006b)

$$\langle D_{\alpha\alpha}\rangle = \frac{1}{S(\alpha_{eq})}\int_0^{\lambda_m} D_{\alpha\alpha}(\alpha)\frac{\cos\alpha\cos^7\lambda}{\cos^2\alpha_{eq}}d\lambda, \tag{4.7}$$

$$\langle D_{\alpha p}\rangle = \frac{1}{S(\alpha_{eq})}\int_0^{\lambda_m} D_{\alpha p}(\alpha)\frac{\sin\alpha\cos^7\lambda}{\sin\alpha_{eq}\cos\alpha_{eq}}d\lambda, \tag{4.8}$$

$$\langle D_{pp}\rangle = \frac{1}{S(\alpha_{eq})}\int_0^{\lambda_m} D_{pp}(\alpha)\frac{\sin^2\alpha\cos^7\lambda}{\sin^2\alpha_{eq}\cos\alpha}d\lambda, \tag{4.9}$$

where $S(\alpha_{eq}) = 1.3 - 0.56\sin\alpha_{eq}$ (Hamlin et al. 1961), α_{eq} is associated with local pitch angle α by $\sin^2\alpha = \frac{\sqrt{1+3\sin^2\lambda}}{\cos^6\lambda}\sin^2\alpha_{eq}$, and λ_m is the upper limit of magnetic latitude deter-

mined either by the mirror latitude of the particles or the maximum latitude of the wave occurrence. Note that $S(\alpha_{eq})$ is related to the bounce period τ_B. Its expression can be quite different for non-dipolar magnetic field, and readers are referred to Orlova and Shprits (2011) for detailed discussions on approximate equations of $S(\alpha_{eq})$ in various geomagnetic field models. To avoid the singularity at the mirror point associated with Eqs. (4.7)–(4.9), the upper limit of the intergrade is generally set as $0.999\lambda_m$ (e.g., Glauert and Horne 2005).

Following Albert (2007), for electromagnetic plasma waves, the local pitch angle diffusion rate $D_{\alpha\alpha}$ can be written as

$$D_{\alpha\alpha} = \frac{\Omega_\sigma}{\gamma^2}\frac{B_W^2}{B_0^2}\sum_{N=-\infty}^{\infty}\sum_{\omega} D_{\alpha\alpha}^N, \tag{4.10}$$

$$D_{\alpha\alpha}^N = \int_{\theta_{LC}}^{\theta_{UC}} \sin\theta d\theta \Delta_N G_1 G_2, \tag{4.11}$$

with

$$\Delta_N(\omega,\theta) = \frac{\pi}{2}\frac{\sec\theta}{|v_{||}/c|^3}\Phi_N^2\frac{(-\sin^2\alpha + N\Omega_\sigma/\omega\gamma)^2}{|1-(\partial\omega/\partial k_{||})_\theta/v_{||}|}, \tag{4.12}$$

$$G_1(\omega) = \frac{|\Omega_\sigma|B^2(\omega)}{\int_{\omega_{LC}}^{\omega_{UC}} B^2(\omega')d\omega'}, \qquad G_2(\omega,\theta) = \frac{g_\omega(\theta)}{\chi(\omega)}, \tag{4.13}$$

$$\chi(\omega) = \int_{\theta_{LC}}^{\theta_{UC}} d\theta' \sin\theta' \Gamma g_\omega(\theta'), \quad \Gamma = \mu^2\left|\mu + \omega\frac{\partial\mu}{\partial\omega}\right|, \tag{4.14}$$

$$\begin{aligned}\Phi_N^2 = &\left[\left(\frac{D}{\mu^2-S}\right)^2\left(\frac{\mu^2\sin^2\theta - P}{\mu^2}\right)^2 + \left(\frac{P\cos^2\theta}{\mu^2}\right)^2\right]^{-1}\\ &\times\left[\frac{\mu^2\sin^2\theta - P}{2\mu^2}\left(1+\frac{D}{\mu^2-S}\right)J_{N+1} + \frac{\mu^2\sin^2\theta - P}{2\mu^2}\left(1-\frac{D}{\mu^2-S}\right)J_{N-1}\right.\\ &\left.+\cot\alpha\sin\theta\cos\theta J_N\right]^2.\end{aligned} \tag{4.15}$$

Here B_W is the wave amplitude, μ is the refractive index, kc/ω, given as a function of (ω,θ) by cold plasma theory, and D, S, P are the usual Stix coefficients (Stix 1962). The term Φ_N^2 accounts for the relationships between the components of wave electric and magnetic fields as well as the gyro-averaging of the resonant wave-particle phase, containing Bessel functions J_N, $J_{N\pm1}$ with argument $k_\perp P_\perp/m_\sigma\Omega_\sigma$. The function $B^2(\omega)$ describes the frequency distribution of wave power, and is taken to be zero unless ω lies between the lower and upper frequency cutoffs ω_{lc} and ω_{uc}. By default, a Guassian frequency distribution is adopted, i.e.,

$$B^2(\omega) = A'\exp\left[-\left(\frac{\omega-\omega_m}{\delta\omega}\right)^2\right], \quad (\omega_{lc} < f < \omega_{uc}) \tag{4.16}$$

where ω_m and $\delta\omega$ are the frequency of maximum wave power and bandwidth, respectively, and A' is a normalization constant given by

$$A' = \frac{B_W^2}{\delta\omega}\frac{2}{\pi^{1/2}}\left[erf\left(\frac{\omega_m-\omega_{lc}}{\delta\omega}\right) + erf\left(\frac{\omega_{uc}-\omega_m}{\delta\omega}\right)\right]^{-1}. \tag{4.17}$$

Similarly, the function $g_\omega(\theta)$ describes the wave normal angle distribution of wave power, and is taken to be zero unless θ lies between the lower and upper wave normal angle cutoffs θ_{lc} and θ_{uc}. Commonly, the wave normal angle distribution is assumed to be Gaussian, i.e.,

$$g_\omega(\theta) = \exp\left[-\left(\frac{\tan\theta - \tan\theta_m}{\tan\theta_w}\right)^2\right] \quad (\theta_{lc} \le \theta \le \theta_{uc}) \tag{4.18}$$

where θ_m is the peak wave normal angle and θ_w is the angular width. $G_2(\omega, \theta)$ and $\Delta_N(\omega, \theta)$ are computed at the resonant frequency ω corresponding to θ and N. There may be several such values of ω, as simultaneous solutions of the resonance condition (Eq. (2.1)) and the cold-plasma wave dispersion relation

$$A\mu^4 + B\mu^2 + C = 0 \tag{4.19}$$

with

$$A = S\sin^2\theta + P\cos^2\theta, \qquad B = -\left[RL\sin^2\theta + PS\left(1+\cos^2\theta\right)\right], \qquad C = PRL, \tag{4.20}$$

where R, L, S, P are the usual Stix coefficients (Stix 1962). Local cross diffusion rate $D_{\alpha p}$ and momentum diffusion rate D_{pp} can be subsequently obtained by (e.g., Lyons 1974b; Glauert and Horne 2005; Albert 2007)

$$D_{\alpha p} = D_{\alpha\alpha}\left[\frac{\sin\alpha\cos\alpha}{N\Omega_e/(\gamma\omega_k) - \sin^2\alpha}\right], \qquad D_{pp} = D_{\alpha\alpha}\left[\frac{\sin\alpha\cos\alpha}{N\Omega_e/(\gamma\omega_k) - \sin^2\alpha}\right]^2. \tag{4.21}$$

Equations (4.10)–(4.21) are appropriate for use to evaluate the particle scattering rates induced by electromagnetic waves in space including chorus and EMIC waves considered in this review.

However, a new method is required to quantify pitch angle scattering of plasma sheet electrons by highly oblique, broadband electrostatic ECH emissions. Theoretically, quantification of diffusion rates requires integration over the entire ECH frequency band. Ni et al. (2011a) developed the weighting method to calculate the ECH wave-induced diffusion rates at a number of representative frequencies and introducing reasonable weighting factors at each wave frequency to obtain the overall diffusion coefficients efficiently and reasonably. The major procedure is outlined here.

The local pitch angle diffusion coefficient for electrons due to single-frequency electrostatic ECH waves (in units of s^{-1}) is given by

$$D_{\alpha\alpha} = \sum_{N=-\infty}^{+\infty} \int k_\perp dk_\perp \cdot \left[\Psi_{N,k}\left(\frac{N\Omega_e/\omega - \sin^2\alpha}{\sin\alpha\cos\alpha}\right)^2\right]_{k_{||}=k_{||,res}} \tag{4.22}$$

with

$$\Psi_{N,k} = \frac{1}{4\pi}\frac{e^2}{m_e^2}\frac{|E_k|^2}{V}\left(\frac{\omega}{|k|}\right)^2 \frac{J_N^2(k_\perp v_\perp/\Omega_e)}{v^4|v_{||} - \partial\omega/\partial k_{||}|}, \tag{4.23}$$

where $k_\perp$ and $k_{||}$ are the components of the wave vector perpendicular and parallel to the ambient magnetic field $\mathbf{B}_0$, respectively, $k_{||,res} = (\omega_k - N\Omega_e/\gamma)/v_{||}$ is the resonant parallel wave number, $\Omega_e = |eB_0/m_e|$ is the angular electron gyrofrequency, ω_k is the wave frequency as a function of $\mathbf{k}$, $\gamma = (1 - v^2/c^2)^{-1/2}$ is the Lorentz factor with v as the electron

velocity and c the speed of light, α is the electron pitch angle, V is the plasma volume, e/m_e is the electron charge to mass ratio, and J_N is the Bessel function of order N. Assuming that the parallel group velocity is small compared to the electron parallel velocity (i.e., $\partial\omega_k/\partial k_{||} \ll v_{||}$) and that the electric field spectrum has the form of

$$|E_k|^2 = C' k_\perp^2 \exp\left[-\left(\frac{k_\perp}{k_{0,\perp}}\right)^2\right] \cdot \left\{\exp\left[-\left(\frac{k_{||}-k_{0,||}}{\delta k_{||}}\right)^2\right] + \exp\left[-\left(\frac{k_{||}+k_{0,||}}{\delta k_{||}}\right)^2\right]\right\} \tag{4.24}$$

with a normalization constant

$$C' = \frac{4\pi^{3/2}}{k_{0,\perp}^4 \delta k_{||}} V |E_w|^2 \tag{4.25}$$

obtained from $\int |E_w|^2 dr = \frac{1}{8\pi^3} \int |E_k|^2 dk$, Horne and Thorne (2000) developed Eq. (4.22) into a modified version

$$D_{\alpha\alpha} = \frac{\sqrt{\pi}}{2} \frac{e^2}{m_e^2} \frac{|E_w|^2 \sin^2\varphi}{k_{0,\perp}^2 \delta k_{||}} \frac{\exp(-\mu)}{v^5 \cos\alpha} \times \sum_{N=-\infty}^{+\infty} \left(\frac{N\Omega_e/\omega_k - \sin^2\alpha}{\sin\alpha\cos\alpha}\right)^2 I_N(\mu)\left\{\exp\left[-\left(\zeta_N^-\right)^2\right] + \exp\left[-\left(\zeta_N^+\right)^2\right]\right\}, \tag{4.26}$$

where $k_{0,\perp}$ and $k_{0,||}$ are the wave number perpendicular and parallel to the ambient magnetic field $\mathbf{B}_0$, respectively, corresponding to the peak of the wave power, $\delta k_{||}$ is the width of the wave spectrum distribution over parallel wave number, $I_N(\mu)$ is the modified Bessel function with the argument $\mu = k_{0,\perp}^2 v_\perp^2/(2\Omega_e^2)$, and $\zeta_N^\pm = \frac{\omega_k - N\Omega_e}{\delta k_{||} v \cos\alpha} \pm \frac{k_{0,||}}{\delta k_{||}}$.

Based on Eq. (4.26) for $D_{\alpha\alpha}$, local pitch angle-momentum mixed diffusion rate $D_{\alpha p}$ and momentum diffusion rate D_{pp} can be obtained from Eq. (4.21). Bounce-averaging the local diffusion rates over the electron bounce trajectory follows Eqs. (4.4)–(4.6).

The above equations can be readily applied to evaluate the bounce-averaged resonant diffusion coefficients for ECH waves at any specified frequency once the wave electric field spectrum and wave normal angle distribution are available (Horne and Thorne 2000). Theoretically, quantification of diffusion rates requires integration over the entire ECH frequency band, which is dependent on solving the complicated hot plasma dispersion relation with expensive CPU time. Alternatively, Ni et al. (2011a) have developed a feasible approximate method to use observed ECH wave power spectrum to introduce reasonable weighting factors for the diffusion rates at each wave frequency and to calculate the overall diffusion coefficients by ECH waves efficiently. Specifically, for each ECH harmonic band, the overall bounce-averaged diffusion rates are computed by

$$\langle D \rangle_{overall} = \sum_{j=1}^{M} R_j \langle D \rangle_j \tag{4.27}$$

with the weighting factor for the jth wave frequency given by

$$R_j = \frac{(I_E)_j}{\sum_{j=1}^{M} (I_E)_j}. \tag{4.28}$$

Here M is the number of frequency considered in each band, $\langle D \rangle_j$ is the bounce-averaged diffusion rate due to the jth wave frequency, and $(I_E)_j$ is the electric field intensity for the jth wave frequency.

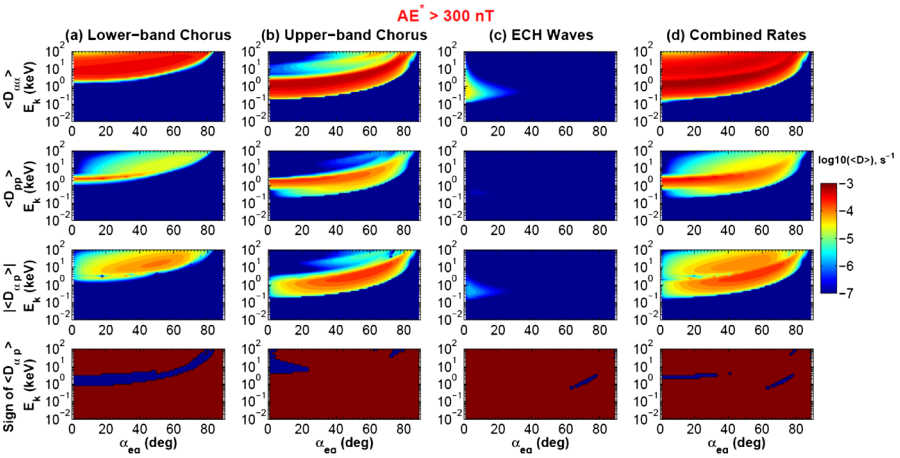

Fig. 14 Modified from Fig. 5 of Ni et al. (2011c). Bounce-averaged diffusion coefficients ($\langle D_{\alpha\alpha}\rangle$, $\langle D_{pp}\rangle$, and $\langle D_{\alpha p}\rangle$) in (equatorial pitch angle, electron kinetic energy) space for (**a**) lower band chorus, (**b**) upper band chorus, (**c**) ECH waves, and (**d**) combined diffusion at $L = 6$ under geomagnetically active conditions ($AE^* > 300$ nT). The sign of mixed diffusion $\langle D_{\alpha p}\rangle$ is shown *on the bottom*

4.2 Electron Scattering Rates by Whistler-Mode Chorus and ECH Waves

When the wave information (e.g., frequency spectrum and wave normal angle distribution) and the background plasma density and magnetic field is available, quasi-linear bounce-averaged scattering rates by various plasma waves can be numerically quantified to evaluate the efficiency of waves in resonant scattering energetic particles.

Using the statistical wave power spectral profiles obtained from CRRES wave data within the 00:00–06:00 MLT sector under different levels of geomagnetic activity and a modeled latitudinal variation of wave normal angle distribution, Ni et al. (2011a, 2011c) quantitatively evaluated the effects of lower-band and upper-band chorus and ECH waves on resonant diffusion of plasma sheet electrons for diffuse auroral precipitation in the inner magnetosphere. They found that resonant scattering of plasma sheet electrons by both wave modes is strongly geomagnetic activity dependent. Specifically, for whistler-mode chorus the rates of scattering vary from above the strong diffusion limit (timescale of an hour) during active times ($AE^* > 300$ nT) with peak wave amplitudes of >50 pT to weak scattering (timescale of a day) during quiet conditions ($AE^* < 100$ nT) with typical wave amplitudes of ≤10 pT. ECH wave scattering of plasma sheet electrons varies from near the strong diffusion rate (timescale of an hour or less) during active times with peak wave amplitudes on the order of 1 mV/m to very weak scattering (on the timescale of >1 day) during quiet conditions with typical wave amplitudes of tenths of mV/m.

Figure 14 shows the bounce-averaged diffusion rates of electrons between 10 eV and 100 keV due to lower band chorus, upper band chorus, and ECH waves at $L = 6$ on the nightside (00:00–06:00 MLT) and the total diffusion rates due to combined diffusion by all three waves for geomagnetically active conditions ($AE^* > 300$ nT, where AE^* is the maximum AE in the previous 3 h). Contributions from cyclotron harmonic resonances between $N = -5$ and $N = 5$ and the Landau resonance $N = 0$ are included. The nightside lower-band chorus and upper-band chorus is confined to 15^0 and 10^0 of the magnetic equator, respectively, while ECH waves are confined within 3^0 of the magnetic equator. Near

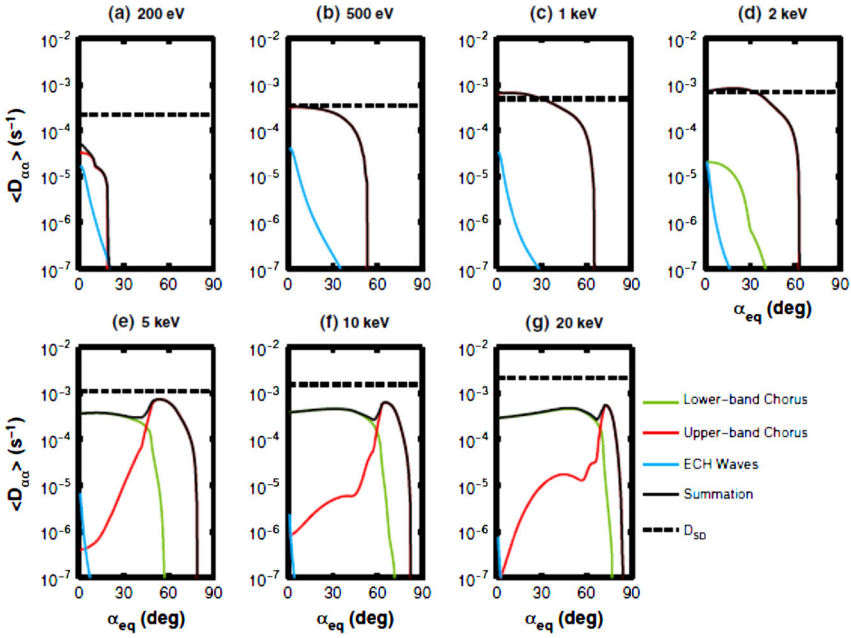

Fig. 15 Adapted from Fig. 2 of Thorne et al. (2013b). Bounce-averaged pitch angle scattering coefficients $\langle D_{\alpha\alpha} \rangle$ as a function of equatorial pitch angle for electrons interacting with each of the three wave modes at $L = 6$ and the net diffusion rates at the specified energies from 200 eV to 20 keV, under geomagnetically active conditions ($AE^* > 300$ nT). The *horizontal dashed line in each plot* represents the strong diffusion rate D_{sd} for comparison

the loss cone, upper-band chorus is the controlling scattering process for electrons from ~100 eV to ~2 keV, and lower-band chorus is most effective for precipitating the higher energy (>~2 keV) plasma sheet electrons in the inner magnetosphere, consistent with the previous study (Ni et al. 2008). ECH waves can also cause scattering loss of plasma sheet electrons from ~100 eV to ~5 keV, but at a rate at least an order of magnitude smaller than that of upper band chorus. ECH waves are only responsible for rapid pitch angle diffusion (occasionally near the limit of strong diffusion) for a small portion of the electron population with pitch angles $\alpha_{eq} < 20^0$, depending on the electron energy. The combined effect of pitch angle scattering by lower band chorus, upper band chorus and ECH waves, obtained under the assumption that individual wave processes are additive and independent, demonstrates that under active conditions the combination of all three waves produce rapid precipitation losses of plasma sheet electrons over a broad range of both energy and pitch angle, namely, from ~100 eV to 100 keV with equatorial pitch angle α_{eq} from the loss cone to up to ~80° depending on the electron energy. Compared to the effects of chorus waves, ECH wave-induced resonant diffusion coefficients are at least an order of magnitude smaller and are negligible in the inner magnetosphere. Chorus-driven momentum diffusion and mixed diffusion are also important. Lower band and upper band chorus can cause strong momentum diffusion of plasma sheet electrons in the energy ranges of ~500 eV to ~2 keV and ~2 keV to ~3 keV, respectively, which can result in significant electron energization and wave attenuation. In contrast, ECH emissions have little effect on local electron acceleration.

Figure 15 shows the line plots of bounce-averaged pitch angle diffusion rate as a function of equatorial pitch angle for electrons interacting with ECH waves and upper and lower band chorus at $L = 6$ for seven specific energies between 200 eV and 20 keV, under geomagnetically active conditions ($AE^* > 300$ nT). The horizontal dashed line in each plot represents the strong diffusion rate D_{sd} for comparison. The computed scattering rates near the edge of the loss cone are comparable to or within a factor of 3 of the strong diffusion limit over a broad range of energies between 0.3 and 10 keV, which contains the dominant portion of injected plasma sheet electrons. Consequently, under geomagnetically active conditions (i.e., geomagnetic storms or intense substorms), the loss cone should be substantially filled and the precipitation flux should be comparable to the trapped flux as measured by low altitude spacecraft. For less disturbed conditions the scattering rates can fall substantially (typically more than an order of magnitude) below the strong diffusion level, the loss cone will only be partially filled and the diffuse auroral precipitation flux should fall below the strong diffusion limit. The dependence of the wave scattering rates and resultant loss timescales of plasma sheet electrons on geomagnetic activity is consistent with the analyses of Chen and Schulz (2001a, 2001b), which showed that pitch angle diffusion less than everywhere strong is needed to better simulate the global MLT distribution of diffuse auroral precipitation and also account for the observed decrease in trapped electron flux on the dayside. The dominance of chorus wave scattering over ECH wave scattering has been found to hold true in the inner magnetosphere ($L < \sim 8$) under any level of geomagnetic activity when both wave modes are present (Thorne et al. 2010; Ni et al. 2011c; Tao et al. 2011).

4.3 Proton Scattering Rates by EMIC Waves

Scattering by EMIC waves has been long proposed as a viable mechanism for the precipitation loss of central plasma sheet protons that contributes to the proton aurora (e.g., Jordanova et al. 1996; Usanova et al. 2010; Zhang et al. 2011; Liang et al. 2014), which, however, received insufficient attention in the existing literature compared to the mechanism of field line curvature (FLC) scattering. In principle, for the individual role of the EMIC wave scattering precipitation mechanism to be discerned from practical observations, the mechanism should desirably operate in different energy range and/or in different spatial region from the FLC scattering.

Commonly, the three bands of EMIC emissions, i.e., H^+-band, He^+-band, and O^+-band, are assumed to follow a Gaussian frequency distribution described by Eq. (4.16) and a Gaussian wave normal angle distribution described by Eq. (4.18). In addition, the effect of the ion concentration should be taken into account in a cold, multi-ion (H^+, He^+, and O^+) plasma defined by the ratio of each ion, say, $\rho_1 = n_1/N_0$, $\rho_2 = n_2/N_0$, and $\rho_3 = n_3/N_0$ where N_0 is the total electron density, and n_1, n_2 and n_3 denote the hydrogen (H^+), helium (He^+), and oxygen (O^+) ion number densities, respectively. In a multi-ion plasma, for obliquely propagating EMIC waves, resonant frequencies are obtained by the simultaneous solution of the Doppler-shifted resonance condition and the cold plasma dispersion relation, which turns out to satisfy a 14th-order polynomial equation (see the Appendix of Ni et al. 2015).

By adopting the representative parameters below for each wave band: (1) H^+ band: $\omega_{lc} = 0.5\Omega_1$, $\omega_{uc} = 0.7\Omega_1$, $\omega_m = 0.6\Omega_1$, $\delta\omega = 0.1\Omega_1$, $\rho_1 = 0.85$, $\rho_2 = 0.1$, $\rho_3 = 0.05$, where Ω_1 is the proton gyrofrequency in radian; (2) He^+ band: $\omega_{lc} = 2.5\Omega_3$, $\omega_{uc} = 3.5\Omega_3$, $\omega_m = 3\Omega_3$, $\delta\omega = 0.5\Omega_3$, $\rho_1 = 0.7$, $\rho_2 = 0.2$, $\rho_3 = 0.1$, where Ω_3 is the O^+ gyrofrequency in radian; (3) O^+ band: $\omega_{lc} = 0.85\Omega_3$, $\omega_{uc} = 0.95\Omega_3$, $\omega_m = 0.9\Omega_3$, $\delta\omega = 0.05\Omega_3$, $\rho_1 = 0.6$, $\rho_2 = 0.2$, $\rho_3 = 0.2$, the bounce-averaged scattering rates due to EMIC waves in the realistic

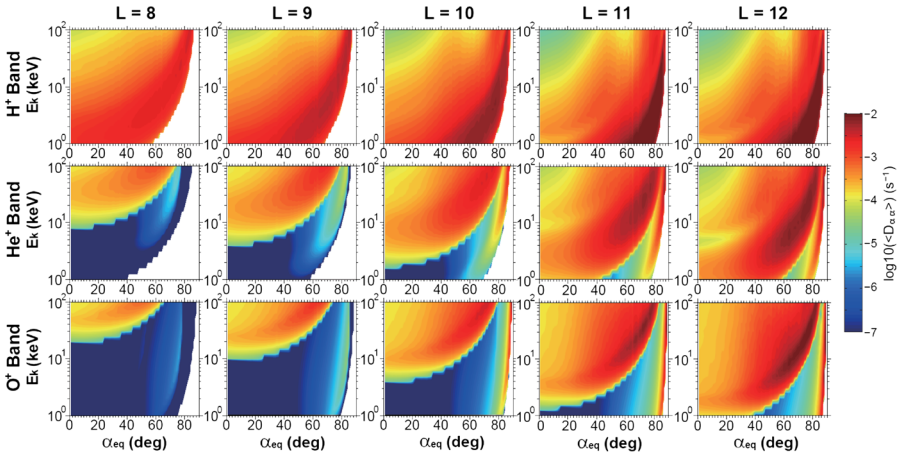

Fig. 16 2-D plots of bounce-averaged pitch angle diffusion rates $\langle D_{\alpha\alpha}\rangle$ as a function of equatorial pitch angle α_{eq} and proton kinetic energy E_k (1–100 keV) for the T01 geomagnetic field model at $L = 8$–12 (*from left to right*) for the three bands of EMIC waves (*from top to bottom*: H^+, He^+, and O^+). The nominal wave amplitude is set as 1 nT

magnetosphere modeled by the Tsyganenko 2001 model (Tsyganenko 2002b) other than a simple dipole field can be computed (using Eqs. (4.4)–(4.6)) for the central plasma sheet with a spatial coverage of $L = 8$–12. Further assumptions include that the waves have a maximum latitudinal coverage of 40° with a nominal wave amplitude of 1 nT and that the wave normal angle distribution varies from the quasi-parallel propagation at the equatorial region to highly oblique direction at high latitudes (Ni et al. 2015). EMIC wave-induced quasi-linear proton scattering coefficients, including contributions from the $N = -5$ to $N = 5$ cyclotron harmonic resonances and the Landau resonance $N = 0$, are shown in Fig. 16 as a function of equatorial pitch angle and proton kinetic energy within 1–100 keV.

Clearly, EMIC waves at various bands can induce intense scattering of central plasma sheet electrons with rates varying from well below 10^{-5} s^{-1} to above 10^{-2} s^{-1}. While H^+-band EMIC waves can strongly resonate with protons at the energy from 1 keV to 100 keV in the central plasma sheet, He^+-band and O^+-band EMIC waves can only scatter less than a few keV protons efficiently. As proton energy increases, EMIC waves tend to resonantly interact with a larger population of the central plasma sheet protons and the resultant scattering rates tend to peak at larger equatorial pitch angles, regardless of the EMIC wave bands. In addition, given the value of EMIC wave amplitude, the rates of proton scattering increase largely with L-shell. In addition, especially for He^+-band and O^+-band EMIC waves, there can occur a second peak of scattering rates at very high equatorial pitch angles close to 90°, which is mainly due to the contribution of the Landau resonance. Figure 17 shows the line plots of bounce-averaged pitch angle scattering rates as a function of equatorial pitch angle for 1, 3, 10, 30, and 100 keV protons at $L = 8$, 10 and 12 corresponding to the three EMIC wave bands (H^+, He^+, and O^+) in the Tsyganenko 2001 model geomagnetic field. The horizontal black-dashed line denotes the strong diffusion rate D_{sd}. Pitch angle diffusion rates of protons due to H^+-band EMIC waves are much stronger than D_{sd} at higher energies. For both He^+-band and O^+-band EMIC waves, pitch angle diffusion rates at $L = 8$ are much smaller than the rate of strong diffusion. However, when L-shell increases, the rate of strong diffusion decreases and the proton scattering rates can exceed it at tens of keV.

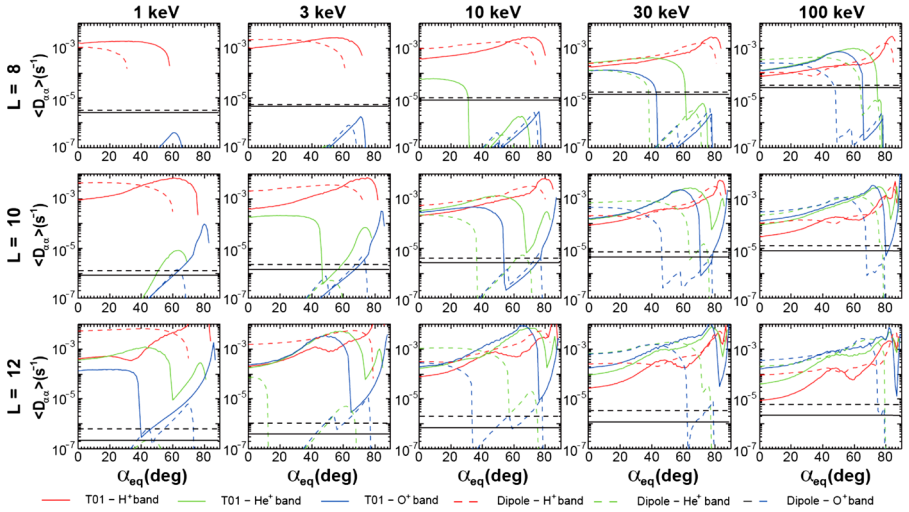

Fig. 17 Corresponding to Fig. 16, line plots of bounce-averaged pitch angle scattering rates as a function of equatorial pitch angle for 1, 3, 10, 30, and 100 keV protons at $L = 8$, 10, and 12, corresponding to the three EMIC wave bands (H^+, He^+, and O^+) and the dipolar and T01 geomagnetic field models

5 Quantitative Understanding of the Origins of the Diffuse Aurora

5.1 Contributions of Whistler-Mode Chorus Waves

The importance of whistler-mode chorus wave scattering to the occurrence of the diffuse auroral precipitation dates back to 1960's. After over five decades of extensive and intensive studies, chorus waves have been recognized as a dominantly important player to drive the most intense electron diffuse auroral precipitation (in the inner magnetosphere) at energies of 100's eV to a few keV and pulsating auroral precipitation at energies of several to tens of keV.

5.1.1 Chorus Scattering as the Major Source for the Nightside Electron Diffuse Aurora in the Inner Magnetosphere

Here "nightside" means the MLT coverage from ~23 MLT to 6 MLT; the inner magnetosphere refers to the region with the equatorial crossings from $\sim 4R_e$ to $\sim 8R_e$, corresponding to the magnetic latitudes (mapped to the surface of the Earth) from ~60° through ~67°. The electron diffuse auroral activity is most intense within this spatial coverage, as shown in Fig. 1. Very interestingly, the nightside electron diffuse auroral precipitation has a distribution and geomagnetic activity dependence similar to that of chorus waves in the inner magnetosphere, as shown in Fig. 18, which leads to a natural connection between the activities of wave emissions and diffuse auroral precipitation on the nightside (e.g., Meredith et al. 2009).

It was Inan et al. (1992) that suggested that lower-band chorus could cause scattering loss of high energy (10–50 keV) electrons, often related to the pulsating aurora, while upper-band chorus could scatter the lower energy (1–10 keV) electrons responsible for the dominant energy input of the diffuse aurora. Villalón and Burke (1995) also presented a test particle theory as well as numerical calculations for the interactions of whistler-mode chorus with

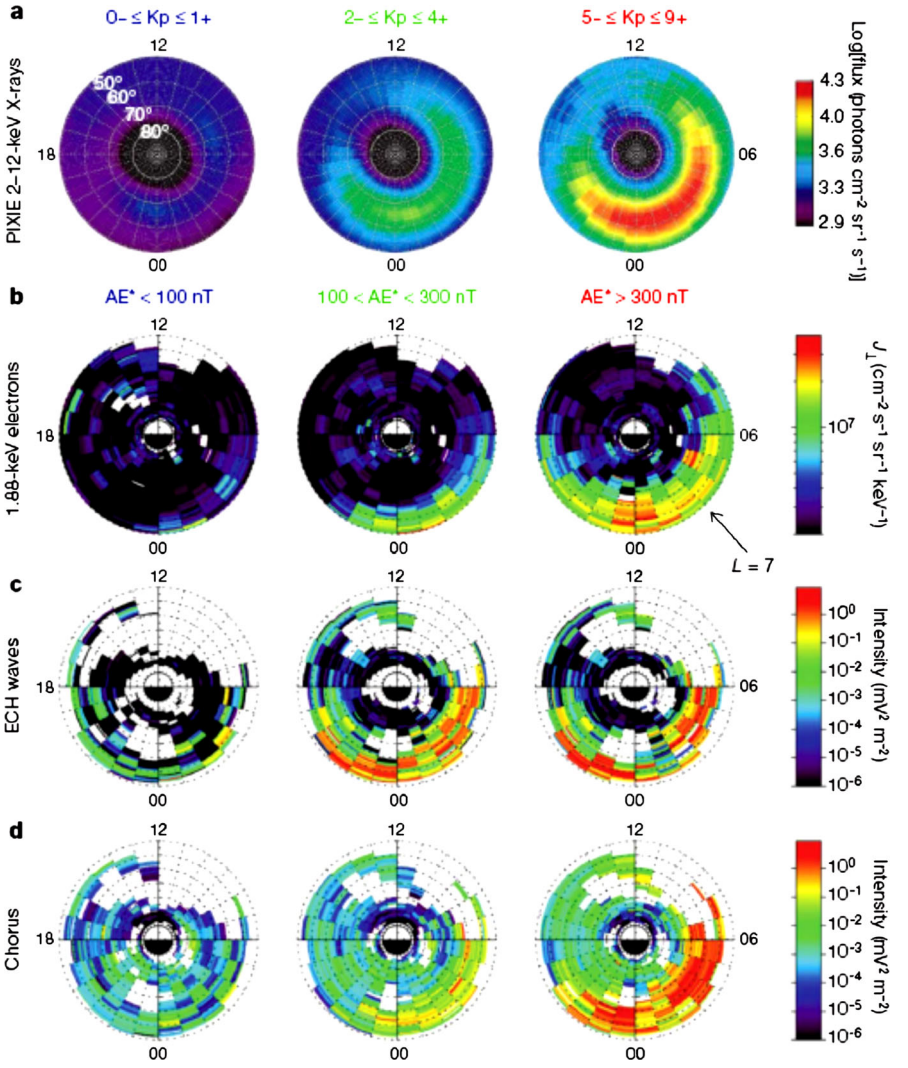

Fig. 18 Adapted from Fig. 1 of Thorne et al. (2010). Global distribution and variability of diffuse auroral emissions, the electron source population, and plasma waves

<10 keV electrons near the equatorial plasma sheet and found that upper-band chorus could scatter plasma sheet electrons into the atmospheric loss cone very efficiently to form the diffuse aurora. Ni et al. (2008) performed a quantitative analysis of the resonant scattering of plasma sheet electrons at $L = 6$ using empirical wave power distributions for lower-band and upper-band chorus. They suggested that upper-band chorus is the dominant scattering process for electrons below ~5 keV, while lower-band chorus is more effective at higher energies, especially near the loss cone. Furthermore, they concluded that chorus scattering could be a major contributor to the origin of diffuse aurora and should also control the MLT distribution of the injected plasma sheet electrons. Based on a high density approximation and an assumed exponentially time-decaying model of chorus wave amplitude, Su et al.

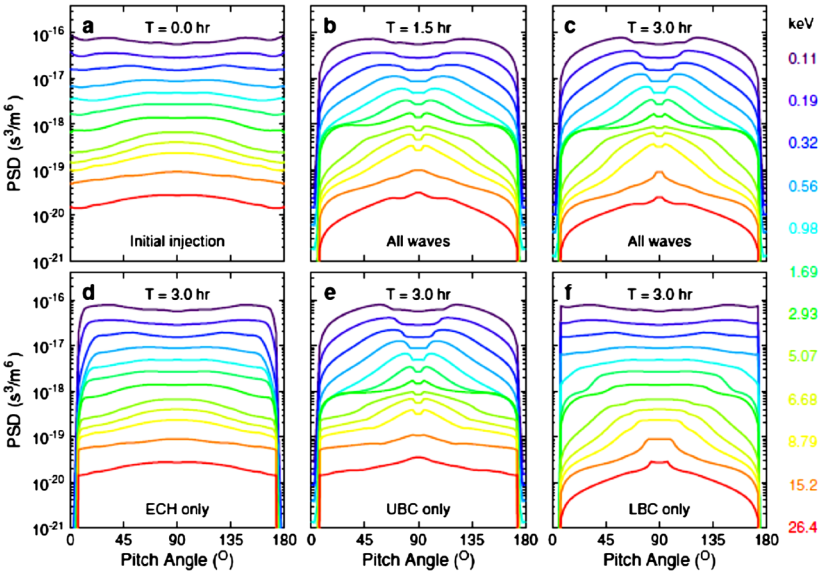

Fig. 19 Adapted from Fig. 3 of Thorne et al. (2013a). Starting with an initial condition representative of an electron injection event (**a**), the evolution of the electron distribution after 3.0 h due to scattering by ECH waves alone (**d**), UBC alone (**e**), LBC alone (**f**) and a combination of all three types of wave at 1.5 h (**b**) and 3.0 h (**c**)

(2009) investigated the evolution of plasma sheet electron pitch angle distribution due to resonant interactions with the double-band chorus emissions by solving the two-dimensional bounce-averaged Fokker-Planck equation.

To model the lifetime of outer zone electrons in a realistic magnetic field, Orlova and Shprits (2014) used realistic chorus wave parameters to compute the lifetime of 1 keV–2 MeV electrons in the Tsyganenko 89 magnetic field model for the night, dawn, prenoon and postnoon MLT sectors for different levels of geomagnetic activity and distances, which can be used in 2-D/3-D/4-D convection and particle tracing codes. The dominance of scattering by chorus waves to account for the occurrence of the nightside electron diffuse aurora in the inner magnetosphere was unambiguously concluded by Thorne et al. (2010), together with the correction (Thorne et al. 2013b). They performed comprehensive theoretical and modeling studies in combination with CRRES observations to compute the bounce-averaged quasi-linear diffusion coefficients by ECH waves, upper band chorus, and lower band chorus and to simulate the temporal evolution of plasma sheet electron pitch angle distribution at $L = 5$ (a representative location where both the activities of nightside diffuse aurora and chorus waves are strongest). The results (Fig. 19) confirm that the combination of upper and lower band chorus can drastically modify the entire population of electrons injected into the inner magnetosphere, leading to the strong electron precipitation to the atmosphere and the formation of pancake distributions at energies below a few keV. The dominant features of Fig. 19(c) are very similar to the CRRES observations of electron distribution a couple of hours after the low energy electron injection from the plasma sheet, and are similar to electron distributions observed by THEMIS satellites following convective electron transport to the dayside. Significantly and conclusively, the studies of Thorne et al. (2010, 2013b) resolved the mystery, concluding that chorus waves are the dominant contributor to the production of the nightside electron diffuse aurora in the inner magnetosphere ($<\sim 8R_e$), and

only chorus waves can explain the remnant pancake electron distribution left behind in space and the pronounced depletion of trapped electrons on the dayside.

Using magnetospheric wave-induced resonant scattering rates of plasma sheet electrons under different geomagnetic conditions, which were computed by Ni et al. (2011a, 2011c) (see Figs. 14 and 15) based on the statistical wave power spectral profiles obtained from CRRES, Tao et al. (2011) investigated the temporal evolution of the phase space density of plasma sheet electron (100 eV–30 keV) injected into the nightside at $L = 6$ during moderate geomagnetic activity. By comparing the simulation results with observations from the THEMIS spacecraft, they demonstrated that the formation of the observed electron pitch angle distributions is mainly due to resonant interactions with a combination of upper and lower band chorus waves. They also pointed out that the pancake distributions at lower energies <2 keV, the flattened pitch angle distributions at medium energies of 2–3 keV, and the distributions with enhanced pitch angle anisotropy at high energies >3 keV can be explained using the banded chorus wave structure with a power minimum at half the electron gyrofrequency. Compared to the effects of chorus waves, ECH wave-induced resonant diffusion coefficients (electron loss timescales) are at least 1 order of magnitude smaller (larger), and their corresponding effects are negligible under any geomagnetic condition. To conclude, chorus wave scattering acts as the major contributor dominantly responsible for the most intense nightside electron diffuse auroral precipitation in the inner magnetosphere.

5.1.2 Chorus Scattering as the Major Source for the Dayside Electron Diffuse Auroral Precipitation

Compared to the intensity of nightside diffuse aurora, the dayside diffuse auroral activity is constantly weaker, which is related to the transport and loss of plasma sheet electrons during the eastward drift after being injected from the nightside plasma sheet. This feature of the global morphology of diffuse auroral precipitation is distinct from the statistics (e.g., Figs. 1 and 2) (Petrinec et al. 1999; Newell et al. 2009). However, the dayside diffuse aurora can become very intense occasionally, and its effect on the dayside magnetosphere-ionosphere coupling is also important. Observational studies by Hu et al. (2009, 2012), using the ground-based all-sky imager (ASI) measurements at the Chinese Yellow River Station (YSR) in Ny-Ålesund, Svalbard, surveyed the synoptic distribution of dayside aurora emissions and their potential correlation with interplanetary magnetic field (IMF). They investigated the auroras at 3 wavelengths (exhibiting blue, green, and red color), which mainly correspond to the precipitating electrons with energies above a few keV, 0.5 to a few keV, and less than 500 eV, respectively. The results indicated a prenoon (07:30–09:30 MLT) "warm spot" characterized uniquely by an increase of 557.7 nm emissions, which is contributed by emissions of the discrete and diffuse aurora, and a midday (09:30–13:00 MLT) gap in relatively weak green line emissions of the discrete and diffuse aurora. Despite intensively improved understanding of the origin of the nightside electron diffuse aurora, the mechanism(s) responsible for dayside diffuse aurora remains unresolved. One main reason is that dayside auroral measurements have an intrinsic limitation (i.e., imager observations require that the background sky be dark) for identification of good conjunctions with in situ wave measurements. Due to the persistent presence of dayside chorus waves as reported by Li et al. (2009), dayside chorus has been thought as a potential major contributor to the dayside electron diffuse auroral precipitation.

Shi et al. (2012) presented a representative event of intense dayside diffuse aurora observed by the Chinese YRS ASI near local noon at $L \sim 9.5$. In principle, the observed intensification of YRS ASI green-line diffuse auroral precipitation was related to the variations of solar wind parameters manifested by fluctuations in the three components of IMF and

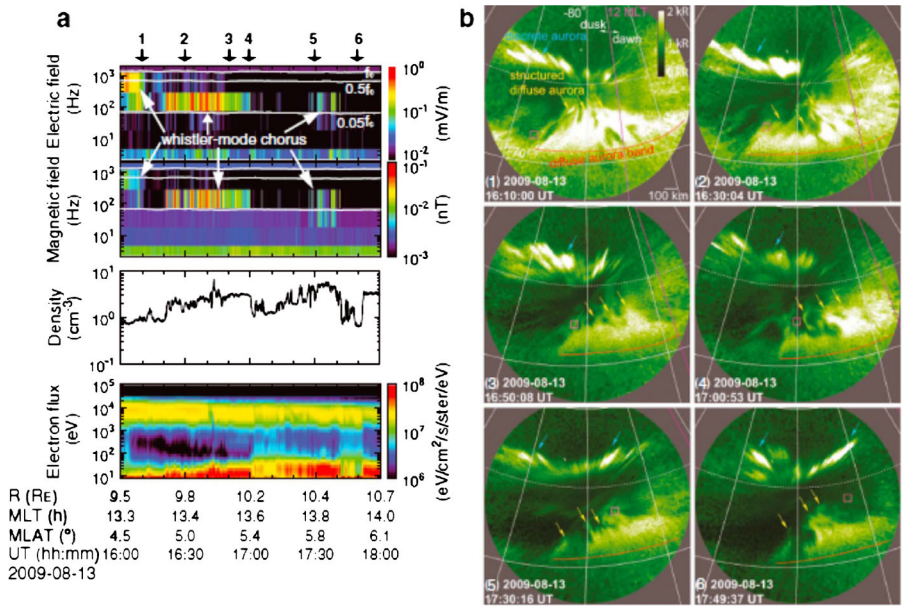

Fig. 20 Adapted from Fig. 1 of Ni et al. (2014). Coordinated observation of the diffuse aurora by the South Pole ASI and whistler mode waves by THEMIS-D spacecraft during 16:00 to 18:00 UT on 13 August 2009. (**a**) THEMIS-D FBK measurements of wave electric and magnetic fields, the ambient plasma density inferred from the spacecraft potential, and the electron flux energy distribution obtained by combining THEMIS-D ESA and SST data (*from top to bottom*). (**b**) South Pole ASI snapshots of the aurora at 557.7 nm wavelength for the six time stamps denoted 1–6 on Fig. 1(a)

noticeable increases in solar wind velocity and solar wind dynamic pressure. Such change of solar wind condition can facilitate the excitation and amplification of magnetospheric whistler-mode chorus waves (e.g., Li et al. 2011b, 2011c), which consequently favors resonant wave-particle interactions. Using a statistical model of dayside chorus waves at high L-shells based upon the THEMIS survey (Li et al. 2009, 2011a), Shi et al. (2012) further computed dayside chorus driven bounce-averaged pitch angle diffusion coefficients for plasma sheet electrons in realistic magnetic field models, which are important for quantifying the role of dayside chorus in driving dayside diffuse auroral precipitation. Their results demonstrated that dayside chorus scattering can produce intense precipitation losses of plasma sheet electrons on timescales of hours (even approaching the strong diffusion limit) over a broad range of both energy and pitch angle, namely, from ∼1 keV to 50 keV with α_{eq} from the loss cone up to ∼85° depending on the electron energy. The resultant loss cone filling by dayside chorus pitch angle scattering may explain the YRS ASI observed green-line diffuse auroral intensification that originated from the enhanced precipitation loss of 0.5 to a few keV plasma sheet electrons. However, lack of simultaneous, conjugate wave measurements in space for the event challenges the quality of the dayside chorus wave model adopted in their study for numerical calculations.

A more detailed and comprehensive study of the role of chorus wave scattering in producing the dayside electron diffuse aurora was performed by Ni et al. (2014) using conjugate satellite wave and particle observations on 13 August 2009 from THEMIS spacecraft and ground-based all-sky imager (ASI) measurements at the South Pole station (Ebihara et al. 2007) on the dayside (13–14 MLT) at $L \sim 9$–10 (Fig. 20). As reported by Nishimura et al.

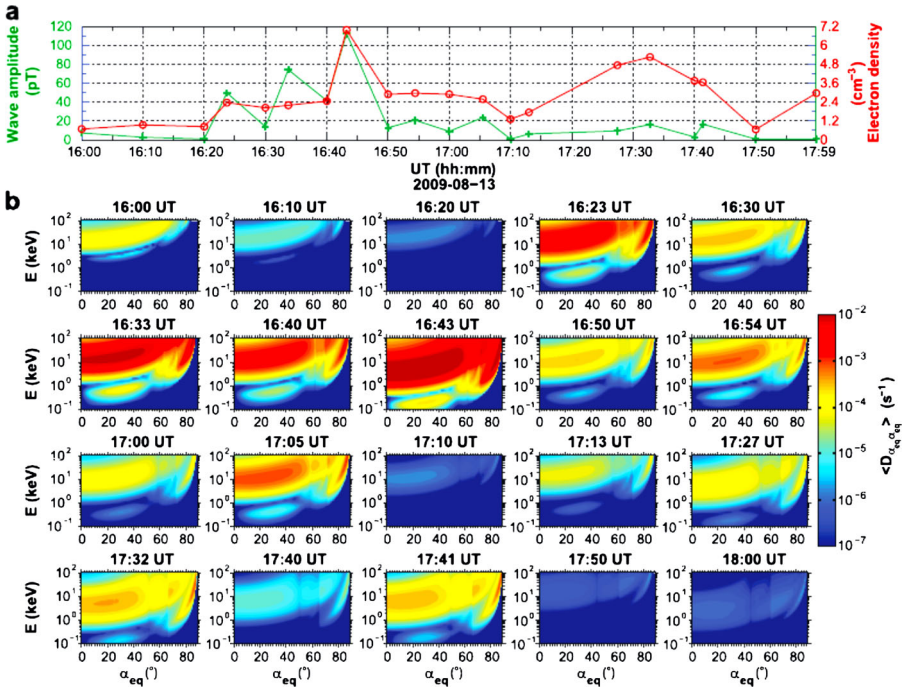

Fig. 21 Adapted from Fig. 2 of Ni et al. (2014). (**a**) Chorus wave amplitude (*green*) obtained by integrating over the two FBK frequency channels, 80–227 Hz and 320–904 Hz, and ambient electron density (*red*) inferred from the spacecraft potential. (**b**) Two-dimensional plots of bounce-averaged pitch angle scattering rates ($\langle D_{\alpha eq \alpha eq} \rangle$) as a function of electron energy (E) and equatorial pitch angle (α_{eq}) at each of the considered 20 times

(2013), clear simultaneous measurements of the dayside electron diffuse aurora and whistler mode waves were registered for that event, and a close correlation between the auroral intensity and wave activity was identified with a high correlation coefficient value of 0.72. Using the in situ wave, particle, and density measurements, Ni et al. (2014) computed the bounce-averaged scattering rates of diffuse auroral electrons by dayside chorus waves using realistic THEMIS-D data and the T01 magnetic field configuration (Tsyganenko 2002a), and then quantitatively analyzed the electron precipitation flux based on diffusion rate results. By comparing the model converted diffuse auroral intensity with the South Pole ASI observations, they finally evaluated the exact role of chorus-induced scattering in triggering the dayside diffuse aurora. Figure 21 displays the profiles of integrated dayside chorus wave amplitude and ambient electron density for the 2-hour period of interest, and the two-dimensional plots of bounce-averaged pitch angle scattering rates as a function of electron energy and equatorial pitch angle for the selected representative 20 times during the period of ground-space conjugate observation. Chorus driven pitch angle scattering is strongly dependent on wave intensity, being most intense during 16:33–16:43 UT when the chorus waves were strongest with amplitudes between 40 and ∼120 pT. Although the peak scattering rates generally occurred at energies of ∼3–20 keV, increases in ambient electron density occasionally led to chorus resonance with plasma sheet electrons at energies down to a few hundred eV. By computing the index of loss cone filling and evaluating the electron precipitation spectrum for Maxwellian-type fits, Ni et al. (2014) subsequently estimated the characteristic energy of the spectrum and total electron precipitation flux which can be

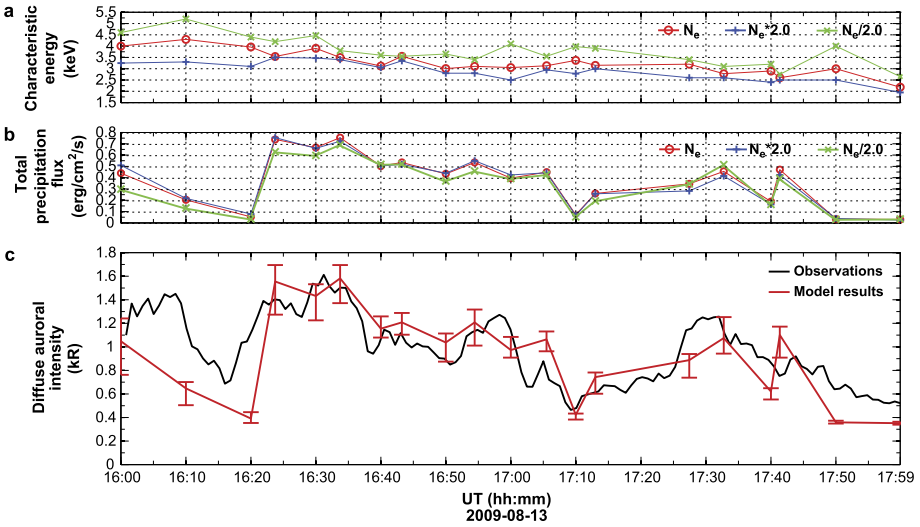

Fig. 22 Adapted from Fig. 6 of Ni et al. (2014). (**a**) Characteristic energy of precipitation electron spectrum and (**b**) total energy flux of electron precipitation inside the loss cone due to chorus scattering during the period of observation, obtained from Maxwellian-type fits to the electron precipitation energy spectrum as shown in Fig. 5. The sensitivity of the results is tested by analyzing the cases of double (*blue curves*) and half (*green curves*) of the nominal electron density. (**c**) Comparisons between the South Pole ASI observed 557.7 nm diffuse aurora intensity (*black*) and model predicted diffuse aurora intensity (*red*)

empirically converted to the 557.7 nm diffuse auroral intensity (Winningham et al. 1978). Figure 22 shows the profiles of computed characteristic energy and total electron precipitation flux, the quantitative comparison between models and observations of dayside electron diffuse aurora, and the sensitivity of modeling results to the ambient electron density with an uncertainty factor of 2. While the characteristic energy of precipitating electrons is considerably dependent on the ambient electron density, the total electron precipitation flux necessary to drive the dayside electron diffuse auroral emissions is much less sensitive to it, indicating that magnetospheric wave intensity rather than background plasma density plays the major role in controlling the intensification of the dayside electron diffuse aurora. Comparisons between the modeled and observed 557.7 nm electron diffuse auroral brightness on the dayside during 16:00–18:00 UT on 13 August 2009 exhibit good agreement with each other, in both the temporal trend of the auroral brightness and the absolute values of the auroral intensity. This provides convincing evidence that for this particular conjugate event, dayside chorus scattering was the dominant driver of the dayside electron diffuse auroral electron precipitation and that the temporal change of the electron diffuse auroral brightness was primarily attributed to the variation of the chorus wave amplitude. The detailed case study of Ni et al. (2014) demonstrated that dayside chorus can primarily contribute to the intensification of dayside green-line diffuse auroral precipitation.

Recently, Shi et al. (2014) reported the modulation of the dayside electron diffuse auroral intensity by the solar wind dynamic pressure using the ASI measurements of Chinese Arctic Yellow River Station in the time interval of 2–10 UT (5–13 MLT) on 2 January 2006. The intensity of dayside electron diffuse aurora was highly correlated with the solar wind dynamic pressure with a maximum coefficient of 0.89. The observation also indicates that changes in solar wind dynamic pressure could efficiently modulate the magnitude of the dayside diffuse aurora, except when the interplanetary magnetic field is southward. It was suggested that the

enhancement of the solar wind dynamic pressure could provide favorable circumstances for dayside chorus wave generation so that the dayside chorus could be a candidate for the production of the dayside electron diffuse aurora and the compressional Pc4-Pc5 pulsations, associated with the solar wind dynamic pressure variations, could simultaneously modulate the intensity of whistler mode chorus waves and its induced scattering process.

It is worthwhile to note that all the above studies are case investigations. While they have provided convincing evidence to support the scenario that chorus wave scattering plays a dominant role in generating the dayside electron diffuse aurora, further quantitative investigations are required for comprehensive analyses of multiple dayside electron diffuse auroral precipitation events under different solar wind conditions and geomagnetic situations to bring closure to the origin of the dayside electron diffuse aurora. Since moderate (>10 pT) dayside chorus emissions have been reported to occur with a high rate and persist even during geomagnetically quiet periods (e.g., Li et al. 2009, 2011a), the overall contribution of dayside chorus scattering to the dayside electron diffuse auroral precipitation is very likely to be significant. Such a proposed explanation of the origin of the dayside electron diffuse aurora, together with previous theoretical studies of the nightside electron diffuse aurora (Ni et al. 2008, 2011a, 2011c, 2011e, 2012b; Thorne et al. 2010, 2013b; Tao et al. 2011; Ma et al. 2012), have improved the current understanding of the roles of resonant wave-particle interactions in the global morphology of the electron diffuse aurora. Since whistler mode chorus waves tend to dominantly control the occurrence of the electron diffuse aurora on the night within $\sim 8 R_e$ and on the dayside, extensive and intensive ground-based observations of the electron diffuse aurora have the potential for use to infer the global distribution of geophysically important chorus waves in space on various temporal and spatial scales.

5.1.3 Chorus Scattering as an Important Source for the Pulsating Aurora

As the more dynamic structure embedded in the diffuse aurora, the pulsating aurora has also received intensive investigations in recent years. The pulsating aurora (PsA) is present as irregular patches of brightness with quasi-periodic (2–20 s or longer) temporal fluctuations (Jones et al., 2009, 2011; Lessard 2012). The intensity variations of the PsA are characterized by a series of rapid on–off switching (Yamamoto 1988), which are caused by the intermittent precipitation of a few to tens of keV electrons (e.g., Miyoshi et al. 2010). In addition, fast modulations embedded in the pulsation, i.e., quasi-3 Hz modulations, can also occur in the precipitation electrons (e.g., Yau et al. 1981).

Samara and Michell (2010) compared the observed feature of lower band chorus (LBC) with the characteristics of the luminosity variations of the PsA. Using coordinated satellite and ground-based all-sky imager observations from the THEMIS mission, Nishimura et al. (2010) provided direct evidence that lower-band chorus can drive pulsating aurora which is known to be excited by modulated, downward-streaming electrons. Figure 23 shows the simultaneous observations of pulsating aurora and chorus waves on 15 February 2009. The auroral pulsations had an almost one-to-one correspondence with each burst of chorus (Fig. 23(d)) with a high cross-correlation coefficient of 0.88, supporting the idea that intensity-modulated lower-band chorus waves drive that pulsating aurora. A later multi-event study by Nishimura et al. (2011) using conjugate measurements of the THEMIS spacecraft and an all-sky imager supported their previous finding that the intensity modulation of lower-band chorus near the magnetic equator is remarkably well correlated with quasi-periodic pulsating auroral emissions near the spacecraft magnetic footprint, indicating that lower-band chorus is the driver of the pulsating aurora. Ground measurements also support the good correspondence between the optical on-off

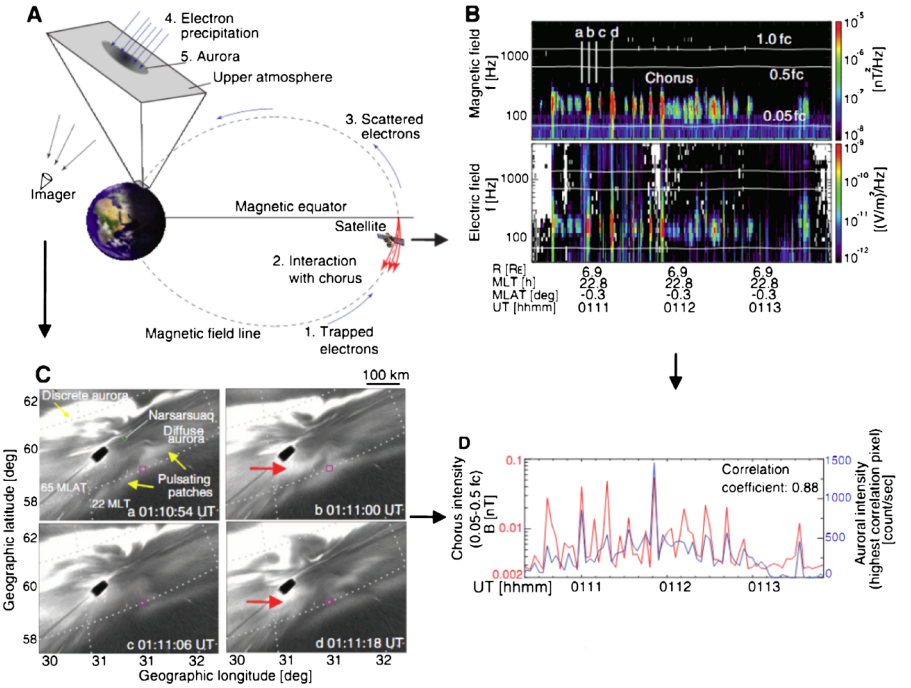

Fig. 23 Adapted from Fig. 1 of Nishimura et al. (2010). Coordinated observation of the pulsating aurora (PsA) by the Narsarsuaq ASI and THEMIS-A spacecraft during 01:10:20 to 01:13:50 UT on 15 February 2009. (**A**) Schematic diagram showing the geometry of chorus wave propagation (*red arrows*), electron precipitation (blue arrows), and PsA. (**B**) THEMIS-A observation of bursts of lower-band chorus shown in electromagnetic field spectra. (**C**) Snapshots of imager data projected onto the geographic coordinates at 110-km altitude. The pulsating patch correlating with chorus is indicated by the *red arrows*. ASI snapshot times are also marked in (**B**) by *white vertical lines*. The *pink square* shows the magnetic footprint of the THEMIS-A spacecraft. *Dashed lines* give magnetic coordinates every 3° in latitude and 1 hour in local time. (**D**) Correlation of lower-band chorus integrated magnetic field intensity over 0.05 to 0.5 fc (*red*) and auroral intensity (*blue*) at the highest cross-correlation pixel

modulations of the PsA and the time variations of chorus bursts (Tsuruda et al. 1981; Ozaki et al. 2012). Miyoshi et al. (2010) reported on a time-of-flight analysis of precipitating electrons associated with pulsating aurora observed by the REIMEI satellite and suggested that the modulation region of the pitch angle scattering is near the magnetic equator. Their estimated parameters, such as wave-frequency and latitudinal distribution of the modulation region, are consistent with previous statistical studies of whistler waves in the magnetosphere. Miyoshi et al. (2010, 2015) proposed a model of wave-induced pitch angle scattering to account for the PsA: chorus waves propagating along the field line resonate with electrons over a wide energy range. They reported that the observed energy dispersion of precipitating electrons was able to be well explained by their model (Miyoshi et al. 2010; Nishiyama et al. 2011), suggesting that the modulation regions that cause the pitch-angle scattering are distributed along the field line.

While the pitch angle scattering of electrons by magnetospheric chorus waves has been regarded as a primary cause for the PsA, some other processes without wave-particle interactions have been also proposed as potential drivers of the PsA. For instance, Sato et al. (2004) discussed that the time-variations of the field-aligned potential drop may cause the pulsating

aurora. Liang et al. (2010) studied multi-probe, multi-instrument THEMIS observations of ECH emissions at $L \sim 11$ and established a potential connection with the concurrent ground-based PsA on 4 January 2009. Nakajima et al. (2012) showed that the Fermi-acceleration associated with the dipolarization can cause the pulsating aurora based on THEMIS and ground-based optical observations. It is expected that more careful and comprehensive analyses should be carried out to fully resolve the major cause(s) of the pulsating aurora and its spatio-temporal dynamics.

5.2 Contributions of Electrostatic Electron Cyclotron Harmonic (ECH) Waves

5.2.1 ECH Wave Scattering as a Minor Cause of the Nightside Electron Diffuse Auroral Precipitation in the Inner Magnetosphere

Besides chorus emissions, ECH waves can also resonate with plasma sheet electrons when the resonance condition is satisfied. While the earliest work by Lyons (1974a) regarding the quantification of ECH wave scattering was argued due to the adopted extremely large ECH wave amplitude that is rarely observed, a careful analysis of CRRES wave data by Meredith et al. (2000) led to a resurgence in the interest of ECH scattering, when they established that wave amplitude following substorm activity were typically above 1 mV/m, whenever the spacecraft was close to the magnetic equator. Adopting a representative amplitude of 1 mV/m for active conditions, Horne and Thorne (2000) found that the substorm-associated ECH waves have sufficient power to cause scattering near the loss cone at a rate comparable to the strong diffusion limit for electrons below 500 eV, which was later confirmed by Horne et al. (2003) based on the analysis of wave propagation and resonant electron scattering for a weak substorm injection event.

In contrast, a number of studies (e.g., Thorne et al. 2010, 2013b; Ni et al. 2011a, 2011c; Tao et al. 2011) have concluded that ECH waves, compared to chorus, play a much less or negligible role in the production of the inner magnetospheric electron diffuse aurora. Readers are referred to Sect. 5.1.1 and Figs. 14, 15 and 19 for more details.

5.2.2 ECH Wave Scattering as the Major Source of the Nightside Electron Diffuse Auroral Precipitation in the Outer Magnetosphere

The statistical study by Newell et al. (2009) revealed contradictory observational evidence regarding the propensity and importance of ECH wave emissions at high L-shells. The electron diffuse auroral precipitation is both statistically significant and energetically efficient at higher latitudes, since about half the emissions are contributed by precipitation at magnetic latitudes from $>65^\circ$ to $\sim 70^\circ$ across ~ 17 hours of MLT centered at ~ 3 MLT (see Fig. 2). Those latitudes are expected to map outside the inner magnetosphere from $L \sim 8$ to beyond $L \sim 15$. On the other hand, according to Ni et al. (2011b), ECH waves at $L >\sim 12$ (Fig. 10) are relatively scarce. Other free energy sources for electron scattering, such as whistler-mode chorus, are also absent at high L-shells (Li et al. 2009, 2011a). The observations therefore suggest that although electron scattering into the loss cone persists at high L-shells, the wave mode, excitation mechanism and amplitude responsible for filling the loss cone and loss-cone properties resulting in the observed precipitation rates are far from understood. Since the electron loss cone still exists in the outer magnetosphere, providing free energy for ECH wave excitation, it is reasonable to assume that these electrostatic waves still exist there.

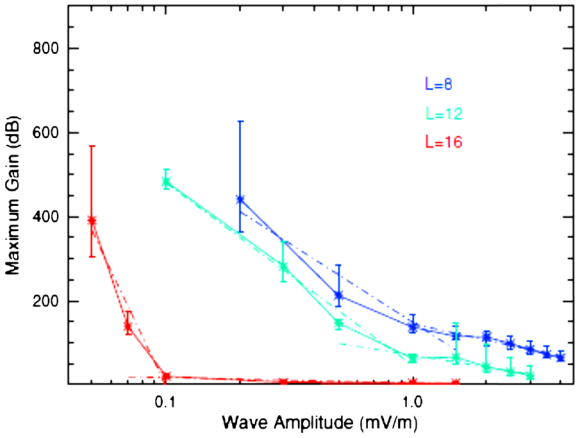

Fig. 24 Adapted from Fig. 5 of Zhang et al. (2013). ECH wave amplification corresponding to different wave electric field amplitudes at $L = 8$, $L = 12$, and $L = 16$. *Dashed lines* were fitted to determine the inflection point corresponding to the quasi-steady state

Zhang et al. (2013) conducted a comprehensive study of wave growth and quasi-linear diffusion to estimate the amplitude of loss-cone-driven ECH waves once diffusion and growth balance but before convection or losses alter the background hot plasma sheet population, which was expected to the most common state of the plasma sheet between episodes of fast convection. For any given wave amplitude, they modeled electron diffusion caused by interaction with ECH waves using a 2-D bounce-averaged Fokker-Planck equation. After fitting the resultant electron distributions as a superposition of multicomponent subtracted bi-Maxwellians, they estimated the maximum path-integrated gain using the HOTRAY ray-tracing code, and argued that the wave amplitude during quasi-steady state is the inflection point on a gain-amplitude curve. As shown in Fig. 24, it was found that during quasi-steady state ECH wave amplitudes can be significant ($\sim$1 mV/m) at $L \sim 8$ but drop to very low values ($<\sim$0.1 mV/m) in the outer magnetotail ($L \sim 16$) and likely fall below the sensitivity of typical instrumentation relatively close to Earth mainly because of the smallness of the loss cone. The study of Zhang et al. (2013) suggested that ECH emissions at high L-shells ($L > \sim 12$) are likely to be present, and can thus be responsible for the observed plasma sheet electron precipitation, even though evidence of those waves may be scarce at current datasets due to their small amplitude.

The scenario that ECH waves may play a leading role in driving the nightside electron diffuse aurora at $L > \sim 8$ has been pointed out by a number of recent studies. To investigate the diffuse aurora and its conjunction to plasma wave activity in the outer central plasma sheet, Liang et al. (2011a) performed a detailed event study using the simultaneous in situ wave and particle observations by three THEMIS inner probes and ground-based NORSTAR optical auroral observations during 08–09 UT on 5 February 2009. Their analysis of the THEMIS FBK and FFT wave data showed either an absence of chorus activity or very weak chorus activity and captured an unambiguous positive correlation between the simultaneously observed intensities of the diffuse auroral precipitation and ECH emissions. To validate their proposed scenario that ECH wave scattering was responsible for the NORSTAR MSP observed green-line auroral intensities, Liang et al. (2011a) assessed the precipitating energy fluxes under a rough assumption that the loss cone is fully filled for all electron energies. Their estimate was qualitatively comparable to but larger than actually observed values.

A more comprehensive theoretical and numerical analysis was performed by Ni et al. (2012a) to quantify the role of ECH emissions in scattering the outer central plasma sheet

electrons and driving the postmidnight diffuse auroral precipitation at $L = 11.5$ reported by Liang et al. (2011a). To achieve a credible magnetosphere-ionosphere mapping in the outer central plasma sheet and high-quality ambient magnetic field geometry for diffusion rate calculations, the event-adaptive AM-03 magnetic field model (Kubyshkina et al. 2009, 2011) was adopted to perform a high fidelity numerical analysis. Through a systematic combination of quasi-linear theory, realistic non-dipolar magnetic field mapping and the concept of strong and weak diffusion, Ni et al. (2012a) found that the observed ECH wave activity can cause intense pitch angle scattering of plasma sheet electrons between 100 eV and 5 keV at a rate of $>10^{-4}$ s^{-1} for equatorial pitch angles $\alpha_{eq} < 30°$. The scattering approaches the strong diffusion limit in the realistic ambient magnetic field to produce efficient precipitation loss of $<\sim$5 keV electrons on a timescale of a few hours or less. Using the electron differential energy flux inside the loss cone estimated based upon the energy-dependent efficiency of ECH wave scattering, they found that the auroral electron transport model developed by Lummerzheim (1987) produced an intensity of $\sim$2.3 kR for the green-line diffuse aurora, and separately Maxwellian fitting to the electron differential flux spectrum produced a green-line auroral intensity of $\sim$2.6 kR, both in good agreement with the observed $\sim$2.4 kR green-line auroral intensity (as shown in Fig. 25). Ni et al. (2012a) was the first attempt to quantify the scattering rates of CPS electrons by electrostatic ECH emissions and to simulate the subsequent ionospheric precipitation flux and resulting auroral brightness to study the magnetospheric cause of diffuse aurora in the outer central plasma sheet. While it was a case study, those results support the scenario that enhanced ECH emissions in the central plasma sheet can be an important or even dominant driver of the nightside electron diffuse aurora in the outer magnetosphere. Their study also acts as an important complement to other studies (Thorne et al. 2010, 2013b; Ni et al. 2011a, 2011c; Tao et al. 2011) that have shown lower band and upper band chorus to be mainly responsible for the occurrence of the nightside electron diffuse aurora in the inner magnetosphere.

According to Liang et al. (2011b), ECH emissions may intensify upon the arrival of fast earthward flows in the plasma sheet. Electron injections, rapid increases in energetic particle fluxes at energies from tens to hundreds of keV, are important contributors to particle acceleration and transport in Earth's magnetotail and are observed over a long portion of the magnetotail in association with flow bursts (Sergeev et al. 2009). Injections are typically associated with substorms and are correlated with dipolarization fronts (Moore et al. 1981) in the near-Earth plasma sheet. A number of possible reasons may intensify ECH waves during injections and dipolarization fronts, e.g., a smaller field curvature than in a nominally stretched magnetotail after the dipolarization front passage and enhanced electron fluxes during injections. Higher-amplitude ECH waves can scatter plasma sheet electrons into the loss cone and precipitate them at a higher rate (occasionally even approaching the strong diffusion limit), which can consequently affect the electron diffuse auroral energy flux. Using three comprehensive THEMIS databases of ECH wave events, substorm injections, and dipolarization fronts, Zhang and Angelopoulos (2014) statistically investigated the temporal correlation between those three activities in the magnetotail, finding that 71 % of ECH events are correlated with injections and 52 % are correlated with dipolarization fronts.

To better resolve the exact contribution of ECH waves to the production of the nightside electron diffuse aurora, Zhang et al. (2015) further evaluated quantitatively the ECH wave-induced plasma sheet electron precipitation systematically throughout the entire magnetotail from $6R_e$ to $31R_e$ (the THEMIS apogee). They first modeled the global pattern of diffuse auroral precipitation in the ionosphere using the OVATION Prime model, which is based on 22 years (1984–2005) of energetic particle measurements from the Defense Meteorlogical Satellite Program (DMSP) and develops an empirical relationship between the solar wind

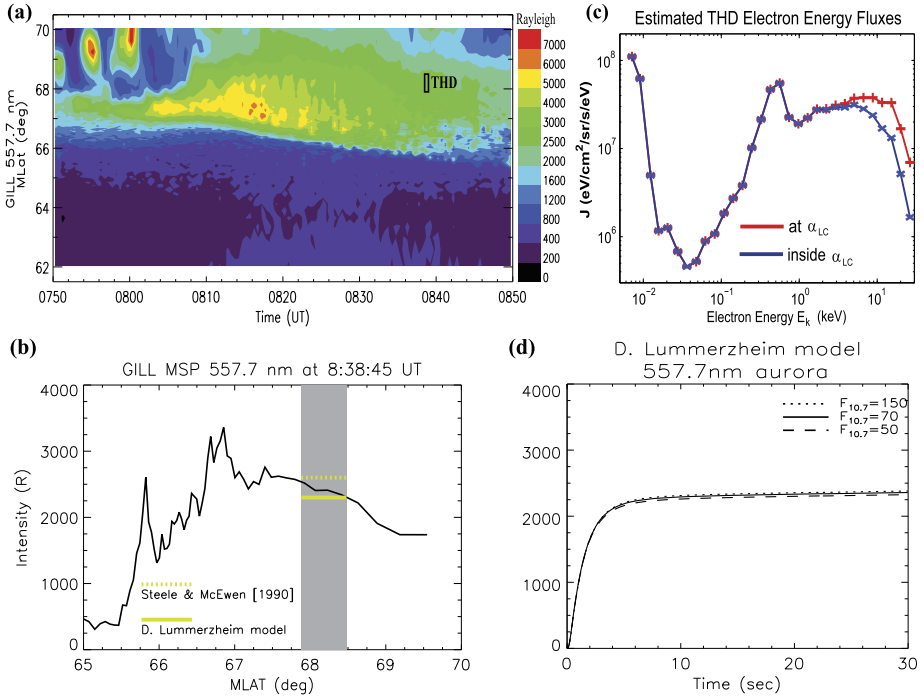

Fig. 25 Adapted from Fig. 6 of Ni et al. (2012a). (**a**) NORSTAR GILL MSP green-line (557.7 nm) auroral observations from 07:50 UT to 08:50 UT on February 5, 2009. The superimposed rectangle denotes the footprint of THD for the time interval of interest, 08:38:43–08:38:51 UT. (**b**) The latitudinal variation of MSP green-line auroral intensity for the time stamp centered at 08:38:45 UT. The *gray band* shows the THD footprint in magnetic latitude, plus/minus 0.3°. The *solid and dotted yellow horizontal lines* represent respectively the modeled green-line auroral intensity using the auroral electron transport model developed by Lummerzheim (1987) and the Maxwellian-type fitting to electron precipitation flux following Steele and McEwen (1990). (**c**) Electron energy flux at the equatorial loss cone (*red curve*) and electron precipitation flux inside the equatorial loss cone (*blue curve*) estimated based upon the index of loss cone filling due to ECH wave scattering. (**d**) Lummerzheim (1987) model results of the 557.7 nm auroral brightness for 3 different profiles of the neutral atmosphere with the solar F10.7 flux of 150, 70 and 50

conditions and the aurora location and intensity (Newell et al. 2010). Subsequently, they modeled the quasi-linear diffusion of electrons with realistic parameters for the magnetic field, loss cone size, and wave intensity (obtained from THEMIS observations as a function of magnetospheric location) and estimated the loss cone filling ratio and ECH wave-induced electron precipitation systematically. By comparing the wave-induced precipitation directly with the equatorially mapped energy flux distribution of the electron diffuse aurora from ionospheric observations (OVATION Prime model) at low altitudes (Fig. 26), they quantified the contribution of auroral energy flux precipitated due to ECH wave scattering. Although the wave amplitudes decrease, as expected, with distance from the Earth, due to the smaller loss cone size and stretched magnetic field topology, ECH waves are still capable of causing sufficient scattering of plasma sheet electrons to account for the observed nightside electron diffuse auroral dissipation, unambiguously demonstrate that ECH waves are the dominant driver of the nightside electron diffuse aurora in the outer magnetosphere, beyond $\sim 8R_e$. Strictly speaking, the study of Zhang et al. (2015) is representative of quiet geomagnetic times, however, given the absence of chorus wave emissions and a free energy source for

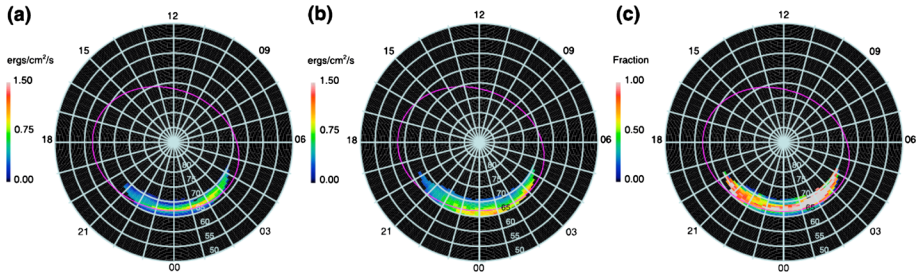

Fig. 26 Adapted from Fig. 11 of Zhang et al. (2015). Ionospheric distribution of (**a**) ECH wave-induced electron precipitation energy flux (obtained by mapping the result in Fig. 10(b) to the ionosphere using T89 magnetic field model), (**b**) diffuse auroral precipitation from OVATION Prime model under median solar wind driving condition during ECH wave measurement intervals (only regions with wave measurements are shown, in order to better compare with Fig. 11(a)), and (**c**) fraction of diffuse auroral precipitation contributed by ECH wave scattering (determined by the ratio of data in Fig. 11(a) over Fig. 11(b)). The magenta ovals mark the latitudes which map to equatorial radial distance of $8R_e$ in T89 magnetic field model

them in the outer magnetosphere ($>8R_e$) at all times (Li et al. 2009, 2010, 2011a), it is naturally expected that ECH waves should be an important or even dominant driver of the nightside electron diffuse aurora at higher latitudes during active times.

5.2.3 ECH Wave Scattering as a Possible Cause of the Pulsating Aurora

As mentioned in Sect. 5.1.3, while chorus wave scattering has been regarded as the most likely dominant driver of the pulsating aurora, scattering by ECH waves can also connect to the occurrence of the pulsating aurora.

Liang et al. (2010) presented an event study of THEMIS multi-probe, multi-instrument observations of ECH waves and explored their potential linkage to the concurrent ground-observed pulsating auroras (a more dynamic auroral form embedded in the diffuse aurora) on 4 January 2009. They identified strong ECH wave activities at $L \sim 11$, but with no evidence of whistler mode chorus from available observations. The ECH emissions were present as discrete packets modulated by the ULF flapping motion of the neutral sheet around the probes, and the overall activeness of the PsA correlated with the in situ measured energetic electron fluxes and ECH wave intensities. A synthesized scenario threading all the case observations was proposed as follows: the enhancement of energetic electron fluxes resulted in an intensification of ECH waves; the fluctuating ECH wave intensities primarily accounted for the PsA generation; the ULF waves structured the ambient plasma sheet, which might play a certain role in modulating the growth rate of the instability and in turn impose a macroscopic control over the spatial distribution of the PsA, particularly along the azimuthal direction.

While the results of Liang et al. (2010) provided some new insights into the relationship between the magnetospheric ECH emissions, the ULF waves, and the PsA, there are a number of deficiencies that prevent them from further exploring the characteristics and the underlying mechanisms of the PsA in more detail. As they pointed out, higher resolution ASIs, better magnetosphere-ionosphere conjugate geometry, and more ideal satellite configurations both in the equatorial magnetosphere and above the topside ionosphere constitute the desirable instrumental combinations to direct toward a definitive answer of the exact contribution of ECH wave scattering to the generation mechanism of the PsA.

5.3 Contribution of Electromagnetic Ion Cyclotron (EMIC) Waves to the Proton Aurora

While electron precipitation plays a dominant role in driving the diffuse auroral activity, ion precipitation, which can drive the proton aurora, is an indivisible portion of the global-scale diffuse auroral precipitation. Low Earth orbit (LEO) satellite observations have clearly shown that the ion precipitation usually manifests as a steep transition from a near-isotropic distribution (except for an up-going loss cone) at higher latitudes to an empty down-going loss cone at lower latitudes, when the satellites traverse the earthward portion of the auroral oval. This transition constitutes the basis of the definition of the isotropic boundary (IB) (Sergeev et al. 1983). The latitudinal profile of ion precipitation fluxes and, in turn, the IB latitudes are dependent upon the ion energies, MLT, and magnetospheric conditions. Such an energy-latitude dependence can offer useful clues on the magnetospheric/ionospheric processes that contribute to the ion precipitation.

In general, according to the energy-latitude dispersion patterns of the precipitating ion flux spectrum, two types of plasma sheet ion precipitation events are classified: "normal-type" events for which the IBs tend to be at lower latitudes for higher-energy protons and increase in latitudes toward lower energies and "reversed-type" events for which the trend is distinctly opposite. The two examples of normal-type and reversed-type events of the ion precipitation, shown in Fig. 27, also indicate that at a fixed latitude the isotropy ratio tends to be lower and higher, respectively, for ions at lower energies during the normal-type and reversed-type events. Using over a few months' FAST data, Donovan et al. (2003) statistically investigated the MLT distribution of normal-type events and reversed-type events. Their results (Fig. 28) captured that while the normal-type events preferentially occur in the evening-morning sector, the occurrence of reversed-type events is heavily biased toward the midnight-morning sector and minimal in the evening sector.

The normal-type ion precipitation events are well explained by the field line curvature scattering mechanism in which the curved field line geometry in the magnetotail causes the protons in the central plasma sheet to be pitch angle scattered into the loss cone and subsequently precipitate into the ionosphere (e.g., Sergeev et al. 1983; Ashour-Abdalla et al. 1990; Liang et al. 2013). The efficiency of this scattering process is controlled by a ratio between the radius of curvature of the magnetic field line and the proton gyroradius. The scattering rate becomes stronger when the ratio is smaller. When such a ratio exceeds certain threshold level (e.g., $\sim$8), the scattering rate is so weak that the loss cone becomes nearly empty, constituting the IB in the ionosphere. Under a normal topology of the magnetosphere, both the curvature radius of the magnetic field line and the equatorial magnetic field strength increase toward the Earth. As a consequence, the IB would extend to lower latitudes for higher-energy ions; at a fixed point in the magnetosphere, the field line curvature scattering rate would be stronger for ions at higher energies, which favorably interprets the major features of the normal-type events. However, the field line curvature scattering mechanism fails to explain the reversed-type ion precipitation events. Scattering by EMIC waves has been proposed to play an important role since EMIC waves can efficiently resonate with plasma sheet and ring current low-energy protons (e.g., Summers 2005).

By studying the proton precipitation from the ring current during the 14–16 May 1997 geomagnetic storm, Jordanova et al. (2001) found that the global patterns of proton precipitation are very dynamic: located at larger L shells under prestorm conditions, moving to lower L shells as geomagnetic activity increases during the storm main phase, and receding back toward larger L shells during the storm recovery phase. In addition, the most intense fluxes were observed along the duskside plasmapause during the main and early recovery

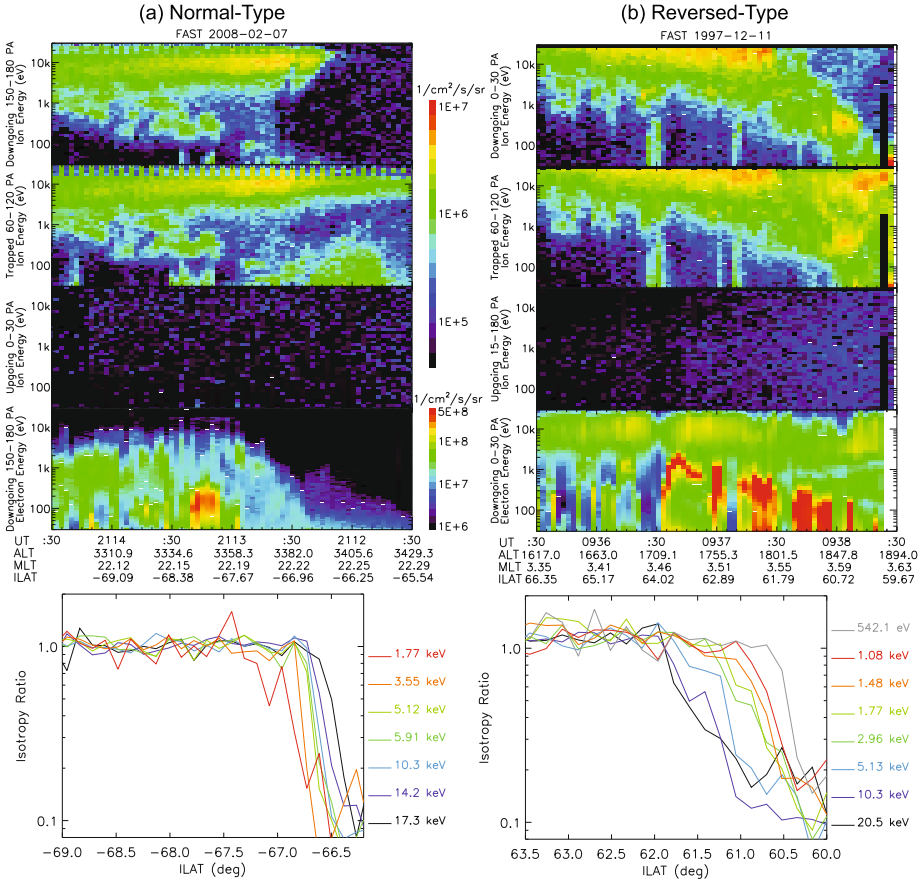

Fig. 27 Adapted from Fig. 1 of Liang et al. (2014). Examples of (**a**) normal-type event and (**b**) reversed-type event. In *each subfigure*, the *first to third panels* show the ion energy flux spectrogram in downgoing, perpendicular, and upgoing directions observed by FAST satellite. The *fourth panel* shows the electron energy flux spectrogram in downgoing direction. The *fifth panel of each subfigure* shows the variation of isotropy ratio versus ILAT for different ion energies; a sharp drop of the isotropy ratio indicates a crossing of the IB of ions at the corresponding energy level

phase of the storm, primarily due to scattering by EMIC waves. Via investigating a number of THEMIS observed ion precipitation events with reversed energy-latitude dependence of precipitation boundaries, Liang et al. (2014) explored viable mechanisms of ion precipitation other than the field line curvature scattering. By raising the mechanism of pitch angle scattering by EMIC waves, they first demonstrated theoretically that in situ observed H^+-band EMIC wave can effectively resonate with keV protons in the central plasma sheet (Fig. 29(a)) and lead to strong pitch angle diffusion of them, at places where the local field line curvature no longer supported their scattering. The EMIC-proton scattering rates were found to have a tendency to decrease with increasing proton energies (Fig. 29(c)), which is contrary to the trend of field line curvature scattering. The H^+-band EMIC wave thus looms as one viable mechanism leading to the precipitation of central plasma sheet thermal protons and to the reversed energy-latitude dependence of the precipitation boundaries, which was

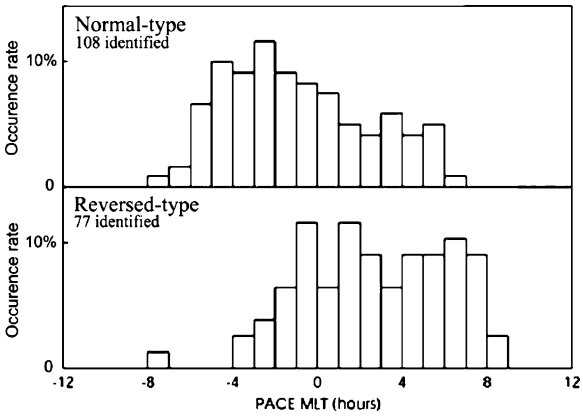

Fig. 28 Adapted from Fig. 2 of Donovan et al. (2003). Statistical MLT distribution of normal-type events and reversed-type events of ion precipitation based upon a statistical survey over a few months' FAST data

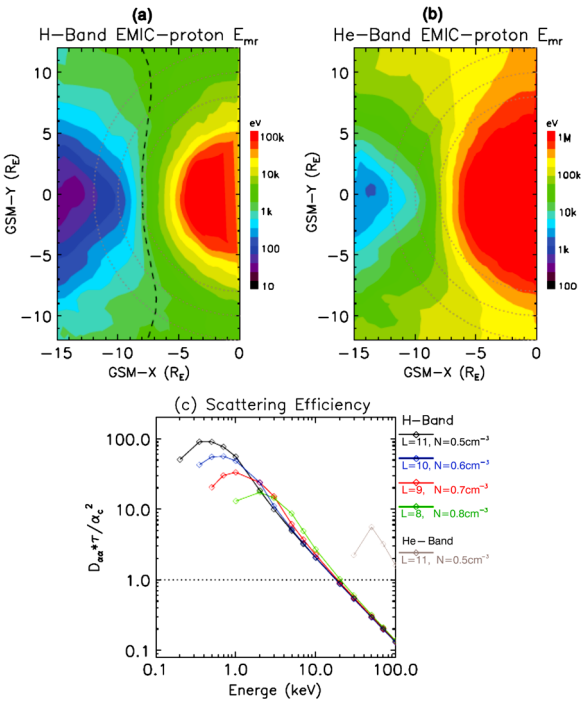

Fig. 29 Adapted from Fig. 3 of Liang et al. (2014). (**a**) Minimum resonant energy for protons interacting with H^+-band EMIC waves. A *dashed line* marks the 12 keV ion isotropic boundary; *dotted circles* indicate radial distances $R = 8$, 10, and $12R_e$, respectively. (**b**) Similar to Fig. 29a but for He^+-band EMIC waves. (**c**) The scattering efficiency of EMIC waves as a function of proton energy at different L shells

strongly supported by multi-case analyses of the reversed-type events based on conjunctive observations from THEMIS.

The theoretical and observational results of Liang et al. (2014) have positioned the EMIC wave scattering mechanism with a high possibility as the leading candidate responsible for the ion precipitation (especially the reversed-type events) in certain regions of the inner central plasma sheet. However, as an initiative step toward the exploration of the non-field-line-curvature-scattering precipitation of central plasma sheet ions, their study could not bring closure to the question. Instead, it has raised useful insights for following investigations. For instance, a more quantitative investigation on EMIC wave-driven proton precipitation fluxes and their comparisons with actual LEO observations should be carefully examined via an

event-oriented approach. In addition, more realistic models and/or information of ambient magnetospheric conditions and key parameters of EMIC waves is critical to quantify the exact role that EMIC waves play in the ion precipitation for the occurrence of the proton aurora.

6 Conclusions and Discussions

Diffuse precipitation of energetic electrons from the magnetosphere is a consequence of pitch angle scattering by a variety of plasma waves. Both magnetospheric ions and electrons undergo the precipitation to the atmosphere and contribute to the occurrence of the diffuse aurora, but the precipitation of energetic electrons constitutes a dominant source of ionizing energy input to the ionosphere and the middle atmosphere. Statistical studies of the global morphology of the diffuse auroral precipitation have indicated both the nightside-dayside asymmetry and the difference between the inner and outer magnetosphere in diffuse auroral intensity, which are not yet fully understood. Here we have reviewed the recent literature on the (possible) mechanisms that can be responsible for the occurrences of diffuse auroral precipitation and can explain the main features of the global distribution of diffuse auroral precipitation. While resonant wave-particle interactions have been long proposed as a fundamental process contributing to the formation of diffuse aurora, understanding the relative importance of various magnetospheric waves, including whistler-mode chorus, ECH emissions, and EMIC waves, to the electron/proton auroral scattering, has been intensively advanced in recent years.

The major scientific findings achieved concerning the roles of various magnetospheric waves in driving the diffuse auroral precipitation can be summarized as follows:

(1) While previous theoretical studies indicated that both whistler-mode chorus and ECH waves can resonate with plasma sheet electrons and contribute to the diffuse auroral precipitation, recent advances have confirmed that electromagnetic chorus waves rather than electrostatic ECH waves act as the dominant contributor to the most intense nightside electron diffuse auroral precipitation in the inner magnetosphere $<8R_e$.
(2) Persistently present on the dayside with a moderate amplitude (>10 pT) even during quiet geomagnetic conditions, whistler-mode chorus is very likely to play a major role in the production of the dayside electron diffuse aurora.
(3) Pulsating auroras, the dynamic auroral structures embedded in the diffuse aurora, can be to a large extent explained by modulation of the excitation of lower band chorus due to macroscopic density variations in the magnetosphere. Field line curvature scattering may also contribute to the occurrence of pulsating auroras.
(4) While scattering by ECH waves acts as a minor or negligible cause of the nightside electron diffuse auroral precipitation in the inner magnetosphere, ECH waves, which can extend to $\sim 12R_e$ or beyond on the nightside, are an important or even dominant driver of the nightside electron diffuse auroral precipitation at high invariant latitudes in the outer magnetosphere. ECH wave scattering can also contribute to the occurrence of the pulsating aurora at high L-shells.
(5) The mechanism of EMIC wave scattering can quite possibly be the leading candidate responsible for the ion precipitation (especially the reversed-type events) in the regions of the central plasma sheet and ring current.

On the other hand, a number of outstanding questions remain concerning the origins of the diffuse aurora and the contributions of wave-particle interactions, including but not limited to,

(1) What is the exact role of ECH waves in driving the nightside electron diffuse auroral precipitation and modifying the global morphology of plasma sheet electrons under different geomagnetic conditions? While Zhang et al. (2015) have dealt with the investigation representative of quiet geomagnetic times, quantitative evaluations of ECH wave-induced precipitation relative to the entire diffuse aurora under various geomagnetic activity levels remain scarce. An improved global distribution of ECH waves with detailed information on wave amplitude, frequency spectrum, and wave normal angle distribution is required to be developed with respect to geomagnetic activity level. To reasonably estimate the latitudinal variations of wave normal angle distribution of ECH wave power, HOTRAY simulations using reliable source electron distributions need to be performed to model the propagation properties of ECH waves at various wave frequencies.

(2) What is the exact role of dayside chorus in driving the dayside electron diffuse auroral precipitation? Systematic correlations between these two phenomena need to be developed based upon conjunction observations. Also, quantitative analyses of chorus-induced scattering rates and resultant ionospheric precipitation fluxes are required to better understand the effect of dayside chorus in driving the dayside diffuse auroral precipitation.

(3) What is the relationship between the pulsating aurora and substorms? What is the total energy involved in pulsating aurora events? What is the spatial extent of the pulsating aurora? And what is the exact role of nonlinear wave-particle interactions in driving the pulsating aurora? Integrated studies that combine ground-based observations, satellite observations, and computer simulations are required to tackle the causal relationship between the micro-process of the wave-particle interactions in the magnetosphere and pulsating aurora (PsA) in the ionosphere. While modulations of the pulsating aurora have been considerably regarded as a manifestation of the nonlinear wave-particle interactions of chorus waves, how to fully establish the one-to-one correspondence from perspectives of both observations and simulations and how to properly evaluate the contribution of ECH waves at higher latitudes remains unresolved.

(4) Can we model the observed global distribution of diffuse auroral precipitation and plasma sheet electron distribution by taking into account the effect of resonant wave-particle interactions as a function of L-shell, MLT, and geomagnetic activity level? This is a particularly interesting and challenging question that can help fully resolve the formation of diffuse aurora and its global morphology. On one hand, appropriate methodology should be adopted. On the other hand, it remains not fully resolved how the evolvement of source electron distribution in association with background magnetic field fluctuations and density variations can account for the excitation and amplification of dayside whistler-mode chorus, especially its persistent presence under any geomagnetic condition.

While theoretical understandings have been greatly advanced to uncover the mystery of the wave origins of the Earth's diffuse auroral precipitation, an essential linkage between the magnetosphere and high-latitude upper atmosphere, more accumulated data from space and ground are required to comprehend accurately the global morphology of the diffuse auroral precipitation and the role of resonant wave-particle interactions. For instance, large-size, high-quality in situ wave data is necessary to establish a reliable model of plasma waves for determination of electron scattering rates. Combinations of wave data from different satellite sources are also needed to construct the global wave distribution as a function of L-shell, MLT, and magnetic latitude under different geomagnetic conditions. In situ particle observations are required to establish the statistical global model of plasma sheet source electron distribution for modeling the wave propagation properties and for comparisons with modeled particle distribution results. In addition, ground-based and low-altitude satellite measurements of diffuse auroral intensity should be analyzed statistically to build up a reliable

global model of diffuse auroral precipitation for quantitative comparisons with model results. Overall, future work on diffuse auroral precipitation should incorporate data as much as possible to develop a more complete and accurate picture of the global distribution of plasma waves and a better understanding of the exact role of each of the major wave modes, including chorus, ECH waves, EMIC emissions and even magnetosonic waves, in driving diffuse auroral scattering at various (L, MLT)-space during different solar wind, geomagnetic, and magnetospheric plasma conditions. With a better understanding of the origin of the diffuse aurora, we will be able to better identify and simulate the electron precipitation into the upper atmosphere and the resultant coupling process between the magnetosphere and the ionosphere, which is urgently needed for incorporation as a critical ingredient into the development of self-consistent global models such as the Geospace General Circulation Models (GGCM), which requires detailed information on the global distribution of ionospheric conductivity that is strongly influenced by the diffuse auroral precipitation. Such studies will also have broader applications for incorporation into the global modeling efforts such as Chen and Schulz (2001a, 2001b), Chen et al. (2005), the Versatile Electron Radiation Belt (VERB) code (Shprits et al. 2009), the Radiation Belt Environment (RBE) model (Fok et al. 2008), or the ring current-atmosphere interactions model (RAM) (Jordanova et al. 2010) to obtain improved simulations of plasma sheet electron dynamics, diffuse auroral precipitation, and associated wave excitation processes. Therefore, to fully understand the occurrences of the diffuse aurora as well as its global morphology is critical to our science community's interests in understanding the dynamic responses of the geo-space environment to solar activity and the complex magnetosphere-upper atmosphere coupling processes.

Acknowledgements We acknowledge the support from the NSFC grants 41204120, 41474141, 41474139 and 41274167, from the Fundamental Research Funds for the Central Universities grant 2042014kf0251 and 2042014kf0269, from the Project funded by the SOA Key Laboratory for Polar Science, and from the Project Supported by the Specialized Research Fund for State Key Laboratories. B. Ni thanks Jun Liang, Xing Cao, Vassilis Angelopoulos, Yuri Shprits, Richard Horne, Nigel Meredith, Eric Donovan, Wen Li, Yukitoshi Nishimura, Emma Spanswick, Marina Kubyshkina, Dirk Lummerzheim, Yusuke Ebihara, Allan Weatherwax, and Yoshizumi Miyoshi for valuable discussions and comments. BN also thanks Xing Cao for helping with the production of Figs. 16 and 17.

References

S.-I. Akasofu, Auroral morphology: a historical account and major auroral features during auroral substorms, in *Auroral Phenomenology and Magnetospheric Processes: Earth and Other Planets*, ed. by A. Keiling, E. Donovan, F. Bagenal, T. Karlsson. AGU Monograph (2012)

J.M. Albert, Nonlinear interaction of outer zone electrons with VLF waves. Geophys. Res. Lett. **29**(8), 1275 (2002). doi:10.1029/2001GL013941

J.M. Albert, Simple approximations of quasi-linear diffusion coefficients. J. Geophys. Res. **112**, A12202 (2007). doi:10.1029/2007JA012551

R.R. Anderson, K. Maeda, VLF emissions associated with enhanced magnetospheric electrons. J. Geophys. Res. **82**(1), 135–146 (1977)

B.J. Anderson, R.E. Erlandson, L.J. Zanetti, A statistical study of Pc1-2 magnetic pulsations in the equatorial magnetosphere: 1. Equatorial occurrence distributions. J. Geophys. Res. **97**, 3075 (1992a)

B.J. Anderson, R.E. Erlandson, L.J. Zanetti, A statistical study of Pc1-2 magnetic pulsations in the equatorial magnetosphere: 2. Wave properties. J. Geophys. Res. **97**, 3089 (1992b)

M. Ashour-Abdalla, C.F. Kennel, Nonconvective and convective electron cyclotron harmonic instabilities. J. Geophys. Res. **83**, 1531–1543 (1978)

M. Ashour-Abdalla, J. Berchem, J. Buchner, L.M. Zelenyi, Chaotic scattering and acceleration of ions in Earth's magnetotail. Geophys. Res. Lett. **17**, 2317–2320 (1990). doi:10.1029/GL017i013p02317

G. Belmont, D. Fontaine, P. Canu, Are equatorial electron cyclotron waves responsible for diffuse auroral electron precipitation? J. Geophys. Res. **88**(A11), 9163–9170 (1983)

T.J. Birmingham, T.G. Northrop, C.G. Falthammar, Charged particle diffusion by violation of the third adiabatic invariant. Phys. Fluids **10**, 660 (1968)
J. Bortnik, R.M. Thorne, N.P. Meredith, Modeling the propagation characteristics of chorus using CRRES suprathermal electron fluxes. J. Geophys. Res. **112**, A08204 (2007). doi:10.1029/2006JA012237
J. Bortnik, R.M. Thorne, U.S. Inan, Nonlinear interaction of energetic electrons with large amplitude chorus. Geophys. Res. Lett. **35**, L21102 (2008). doi:10.1029/2008GL035500
T. Bräysy, K. Mursula, G. Marklund, Ion cyclotron waves during a great magnetic storm observed by Freja double-probe electric field instrument. J. Geophys. Res. **103**, 4145 (1998)
A.W. Breneman, C.A. Kletzing, J. Pickett, J. Chum, O. Santolik, Statistics of multispacecraft observations of chorus dispersion and source location. J. Geophys. Res. **114**, A06202 (2009). doi:10.1029/2008JA013549
N.L. Bunch, M. Spasojevic, Y.Y. Shprits, X. Gu, F. Foust, The spectral extent of chorus in the off-equatorial magnetosphere. J. Geophys. Res. Space Phys. **118**, 1–6 (2013). doi:10.1029/2012JA018182
J.L. Burch, Diagnosis of auroral acceleration mechanisms by particle measurements, in *Auroral Physics*, ed. by C.-I. Meng, M.J. Rycroft, L.A. Frank (Cambridge University Press, Cambridge, 1991), pp. 97–109
W.J. Burtis, R.A. Helliwell, Banded chorus—a new type of VLF radiation observed in the magnetosphere by OGO 1 and OGO 3. J. Geophys. Res. **74**(11), 3002–3010 (1969). doi:10.1029/JA074i011p03002
W. Burtis, R. Helliwell, Magnetospheric chorus: amplitude and growth rate. J. Geophys. Res. **80**(22), 3265–3270 (1975). doi:10.1029/JA080i022p03265
W.J. Burtis, R.A. Helliwell, Magnetospheric chorus: occurrence patterns and normalized frequency. Planet. Space Sci. **24**, 1007–1010 (1976). doi:10.1016/0032-0633(76)90119-7
R.K. Burton, R.E. Holzer, The origin and propagation of chorus in the outer magnetosphere. J. Geophys. Res. **79**(7), 1014–1023 (1974). doi:10.1029/JA079i007p01014
C. Cattell et al., Discovery of very large amplitude whistler-mode waves in Earth's radiation belts. Geophys. Res. Lett. **35**, L01105 (2008). doi:10.1029/2007GL032009
M.W. Chen, M. Schulz, Simulations of storm time diffuse aurora with plasmasheet electrons in strong pitch angle diffusion. J. Geophys. Res. **106**(A2), 1873–1886 (2001a)
M.W. Chen, M. Schulz, Simulations of diffuse aurora with plasma sheet electrons in pitch angle diffusion less than everywhere strong. J. Geophys. Res. **106**(A12), 28949–28966 (2001b)
M.W. Chen, M. Schulz, P.C. Anderson, G. Lu, G. Germany, M. Wüest, Storm time distributions of diffuse auroral electron energy and X-ray flux: comparison of drift-loss simulations with observations. J. Geophys. Res. **110**, A03210 (2005). doi:10.1029/2004JA010725
J.M. Cornwall, F.V. Coroniti, R.M. Thorne, Turbulent loss of ring current protons. J. Geophys. Res. **75**, 4699 (1970)
F.V. Coroniti, Space plasma turbulent dissipation: reality of myth? Space Sci. Rev. **42**, 399–410 (1985)
C.M. Cully, J.W. Bonnell, R.E. Ergun, THEMIS observations of long-lived regions of large-amplitude whistler waves in the inner magnetosphere. Geophys. Res. Lett. **35**, L17S16 (2008). doi:10.1029/2008GL033643
G.T. Davidson, Pitch angle diffusion in morningside aurorae 1. The role of the loss cone in the formation of impulsive bursts of precipitation. J. Geophys. Res. **91**(A4), 4413–4427 (1985)
G.T. Davidson, Pitch-angle diffusion and the origin of temporal and spatial structures in morningside aurorae. Space Sci. Rev. **53**, 45–82 (1990)
E. Donovan, B. Jackel, D. Klumpar, R. Strangeway, Energy dependence of the isotropy boundary latitude, in *Proc. of Atmos. Studies by Optical Methods*, vol. 92 (Sodankylä Geophysical Observatory Publications, Finland, 2003), pp. 11–14
Y. Ebihara, Y.-M. Tanaka, S. Takasaki, A.T. Weatherwax, M. Taguchi, Quasi-stationary auroral patches observed at the South Pole station. J. Geophys. Res. **112**, A01201 (2007). doi:10.1029/2006JA012087
R.E. Erlandson, A.J. Ukhorskiy, Observations of electromagnetic ion cyclotron waves during geomagnetic storms: wave occurrence and pitch angle scattering. J. Geophys. Res. **106**, 3883 (2001)
Y.I. Feldstein, Some problems concerning the morphology of auroras and magnetic disturbances at high latitudes. Geomagn. Aeron. **3**, 183–192 (1963)
M.-C. Fok, R.B. Horne, N.P. Meredith, S.A. Glauert, Radiation belt environment model: application to space weather nowcasting. J. Geophys. Res. **113**, A03S08 (2008). doi:10.1029/2007JA012558
D. Fontaine, M. Blanc, A theoretical approach to the morphology and the dynamics of diffuse auroral zones. J. Geophys. Res. **88**(A9), 7171–7184 (1983)
L.A. Frank, K.L. Ackerson, Observations of charged particle precipitation into the auroral zone. J. Geophys. Res. **76**, 3612 (1971). doi:10.1029/JA076i016p03612
B.J. Fraser, T.S. Nguyen, Is the plasmapause a preferred source region of electromagnetic ion cyclotron waves in the magnetosphere? J. Atmos. Sol.-Terr. Phys. **63**, 1225 (2001)
B.J. Fraser, J.C. Samson, Y.D. Hu, R.L. McPherron, C.T. Russell, Electromagnetic ion cyclotron waves observed near the oxygen cyclotron frequency by ISEE 1 and 2. J. Geophys. Res. **97**, 3063 (1992)

B.J. Fraser, H.J. Singer, W.J. Hughes, J.R. Wygant, R.R. Anderson, Y.D. Hu, CRRES Poynting vector observations of electromagnetic ion cyclotron waves near the plasmapause. J. Geophys. Res. **101**, 15331 (1996)
R.W. Fredricks, F.L. Scarf, Recent studies of magnetospheric electric field emissions above the electron gyrofrequency. J. Geophys. Res. **78**(1), 310–314 (1973). doi:10.1029/JA078i001p00310
H. Fritz, *Polarlichter* (L. Gerold's Sohn, Vienna, 1873). 255 pp.
R. Gendrin, General relationships between wave amplification and particle diffusion in a magnetoplasma. Rev. Geophys. **19**(1), 171–184 (1981). doi:10.1029/RG019i001p00171
M.L. Gilson, J. Raeder, E. Donovan, Y.S. Ge, L. Kepko, Global simulation of proton precipitation due to field line curvature during substorms. J. Geophys. Res. **117**, A05216 (2012). doi:10.1029/2012JA017562
S.A. Glauert, R.B. Horne, Calculation of pitch angle and energy diffusion coefficients with the PADIE code. J. Geophys. Res. **110**, A04206 (2005). doi:10.1029/2004JA010851
B.E. Goldstein, B.T. Tsurutani, Wave normal directions of chorus near the equatorial source region. J. Geophys. Res. **89**(A5), 2789–2810 (1984). doi:10.1029/JA089iA05p02789
M.P. Gough, P.J. Christiansen, G. Martelli, E.J. Gershuny, Interaction of electrostatic waves with warm electrons at the geomagnetic equator. Nature **279**, 515–517 (1979). doi:10.1038/279515a0
D.A. Gurnett, A. Bhattacharjee, *Introduction to Plasma Physics: With Space and Laboratory Applications* (Cambridge University Press, Cambridge, 2005)
D.A. Hamlin, R. Karplus, R.C. Vik, K.M. Watson, Mirror and azimuthal drift frequencies for geomagnetically trapped particles. J. Geophys. Res. **66**(1), 1–4 (1961)
D. Han, X. Chen, J. Liu, Q. Qiu, K. Keika, Z. Hu, J. Liu, H. Hu, H. Yang, An extensive survey of dayside diffuse aurora based on optical observations at Yellow River Station. J. Geophys. Res. Space Phys. **120** (2015). doi:10.1002/2015JA021699
N. Haque, M. Spasojevic, O. Santolík, U.S. Inan, Wave normal angles of magnetospheric chorus emissions observed on the polar spacecraft. J. Geophys. Res. **115**, A00F07 (2010). doi:10.1029/2009JA014717
D.A. Hardy, M.S. Gussenhoven, E. Holeman, A statistical model of auroral electron precipitation. J. Geophys. Res. **90**(A5), 4229–4248 (1985). doi:10.1029/JA090iA05p04229
D.A. Hardy, M.S. Gussenhoven, D. Brautigam, A statistical model of auroral ion precipitation. J. Geophys. Res. **94**, 370–392 (1989). doi:10.1029/JA094iA01p00370
M. Hayakawa, Y. Yamanaka, M. Parrot, F. Lefeuvre, The wave normals of magnetospheric chorus emissions observed on board GEOS 2. J. Geophys. Res. **89**(A5), 2811–2821 (1984). doi:10.1029/JA089iA05p02811
M. Hayakawa, K. Ohta, S. Shimakura, Spaced direction finding of nighttime whistlers at low and equatorial latitudes and their propagation mechanism. J. Geophys. Res. **95**(A9), 15091–15102 (1990). doi:10.1029/JA095iA09p15091
R.B. Horne, Path-integrated growth of electrostatic waves: the generation of terrestrial myriametric radiation. J. Geophys. Res. **94**(A7), 8895–8909 (1989)
R.B. Horne, R.M. Thorne, Convective instabilities of electromagnetic ion cyclotron waves in the outer magnetosphere. J. Geophys. Res. **99**, 17259–17273 (1994)
R.B. Horne, R.M. Thorne, Electron pitch angle diffusion by electrostatic electron cyclotron harmonic waves: the origin of pancake distributions. J. Geophys. Res. **105**(A3), 5391–5402 (2000)
R.B. Horne, R.M. Thorne, N.P. Meredith, R.R. Anderson, Diffuse auroral electron scattering by electron cyclotron harmonic and whistler mode waves during an isolated substorm. J. Geophys. Res. **108**(A7), 1290 (2003). doi:10.1029/2002JA009736
R.B. Horne, R.M. Thorne, S.A. Glauert, J.M. Albert, N.P. Meredith, R.R. Anderson, Timescale for radiation belt electron acceleration by whistler mode chorus waves. J. Geophys. Res. **110**, A03225 (2005). doi:10.1029/2004JA010811
G.B. Hospodarsky, T.F. Averkamp, W.S. Kurth, D.A. Gurnett, M. Dougherty, U. Inan, T. Wood, Wave normal and Poynting vector calculations using the Cassini radio and plasma wave instrument. J. Geophys. Res. **106**(A12), 30253–30269 (2001). doi:10.1029/2001JA900114
Z.-J. Hu et al., Synoptic distribution of dayside aurora: multiple-wavelength all-sky observation at Yellow River Station in Ny-Ålesund, Svalbard. J. Atmos. Sol.-Terr. Phys. **71**, 794–804 (2009). doi:10.1016/j.jastp.2009.02.010
Z.-J. Hu, H.-G. Yang, D. Han, D.-H. Huang, B. Zhang, H.-Q. Hu, R.-Y. Liu, Dayside auroral emissions controlled by IMF: a survey for dayside auroral excitation at 557.7 and 630.0 nm in Ny-Ålesund, Svalbard. J. Geophys. Res. **117**, A02201 (2012). doi:10.1029/2011JA017188
W.L. Imhof, J.B. Reagan, E.E. Gaines, Studies of the sharply defined L dependent energy threshold for isotropy at the midnight trapping boundary. J. Geophys. Res. **84**, 6371–6384 (1979)
U. Inan, Y. Chiu, G. Davidson, Whistler-mode chorus and morning-side aurorae. Geophys. Res. Lett. **19**, 653–656 (1992)

A.D. Johnstone, D.M. Walton, R. Liu, D. Hardy, Pitch angle diffusion of low-energy electrons by whistler mode waves. J. Geophys. Res. **98**, 5959–5967 (1993)
S.L. Jones et al., PFISR and ROPA observations of pulsating aurora. J. Atmos. Sol.-Terr. Phys. **71**, 708 (2009)
S.L. Jones, M.R. Lessard, K. Rychert, E. Spanswick, E. Donovan, Large scale aspects and temporal evolution of pulsating aurora. J. Geophys. Res. **116**, A03214 (2011). doi:10.1029/2010JA015840
V.K. Jordanova, J.U. Kozyra, A.F. Nagy, Effects of heavy ions on the quasi-linear diffusion coefficients from resonant interactions with electromagnetic ion cyclotron waves. J. Geophys. Res. **101**(A9), 19771–19778 (1996). doi:10.1029/96JA01641
V.K. Jordanova, C.J. Farrugia, R.M. Thorne, G.V. Khazanov, G.D. Reeves, M.F. Thomsen, Modeling ring current proton precipitation by electromagnetic ion cyclotron waves during the May 14–16, 1997, storm. J. Geophys. Res. **106**, 7 (2001)
V.K. Jordanova, R.M. Thorne, W. Li, Y. Miyoshi, Excitation of whistler mode chorus from global ring current simulations. J. Geophys. Res. **115**, A00F10 (2010). doi:10.1029/2009JA014810
Y. Katoh, Y. Omura, Computer simulation of chorus wave generation in the Earth's inner magnetosphere. Geophys. Res. Lett. **34**, L03102 (2007). doi:10.1029/2006GL028594
K. Keika, K. Takahashi, A.Y. Ukhorskiy, Y. Miyoshi, Global characteristics of electromagnetic ion cyclotron waves: occurrence rate and its storm dependence. J. Geophys. Res. Space Phys. **118**, 4135–4150 (2013). doi:10.1002/jgra.50385
C.F. Kennel, Consequences of a magnetospheric plasma. Rev. Geophys. **7**(1,2), 379–419 (1969)
C.F. Kennel, M. Ashour-Abdalla, Electrostatic waves and the strong diffusion of magnetospheric electrons, in *Magnetospheric Plasma Physics*, ed. by A. Nishida (Center for Academic Publications, Tokyo, 1982), pp. 245–344
C.F. Kennel, F. Engelmann, Velocity space diffusion from weak plasma turbulence in a magnetic field. Phys. Fluids **9**(12), 2377–2388 (1966)
C.F. Kennel, H. Petschek, Limit on stably trapped particle fluxes. J. Geophys. Res. **71**(1), 1–28 (1966)
C.F. Kennel, F.L. Scarf, R.W. Fredricks, J.H. McGehee, F.V. Coroniti, VLF electric field observations in the magnetosphere. J. Geophys. Res. **75**(31), 6136–6152 (1970)
H.C. Koons, J.L. Roeder, A survey of equatorial magnetospheric wave activity between 5 and 8 RE. Planet. Space Sci. **38**(10), 1335–1341 (1990). doi:10.1016/0032-0633(90)90136-E
J.U. Kozyra, T.E. Cravens, A.F. Nagy, E.G. Fontheim, R.S.B. Ong, Effects of energetic heavy ions on electromagnetic ion cyclotron wave generation in the plasmapause region. J. Geophys. Res. **89**, 2217–2233 (1984)
M. Kubyshkina, V. Sergeev, N. Tsyganenko, V. Angelopoulos, A. Runov, H. Singer, K.H. Glassmeier, H.U. Auster, W. Baumjohann, Toward adapted time-dependent magnetospheric models: a simple approach based on tuning the standard model. J. Geophys. Res. **114**, A00C21 (2009). doi:10.1029/2008JA013547
M. Kubyshkina, V. Sergeev, N. Tsyganenko, V. Angelopoulos, A. Runov, E. Donovan, H. Singer, U. Auster, W. Baumjohann, Time-dependent magnetospheric configuration and breakup mapping during a substorm. J. Geophys. Res. **116**, A00I27 (2011). doi:10.1029/2010JA015882
D.S. Lauben, U.S. Inan, T.F. Bell, D.A. Gurnett, Source characteristics of ELF/VLF chorus. J. Geophys. Res. **107**(A12), 1429 (2002). doi:10.1029/2000JA003019
M. Lessard, A review of pulsating aurora, in *Auroral Phenomenology and Magnetospheric Processes: Earth and Other Planets*, ed. by A. Keiling, E. Donovan, F. Bagenal, T. Karlsson. AGU Monograph (2012)
W. Li, R.M. Thorne, V. Angelopoulos, J. Bortnik, C.M. Cully, B. Ni, O. LeContel, A. Roux, U. Auster, W. Magnes, Global distribution of whistler-mode chorus waves observed on the THEMIS spacecraft. Geophys. Res. Lett. **36**, L09104 (2009). doi:10.1029/2009GL037595
W. Li et al., THEMIS analysis of observed equatorial electron distributions responsible for the chorus excitation. J. Geophys. Res. **115**, A00F11 (2010). doi:10.1029/2009JA014845
W. Li, J. Bortnik, R.M. Thorne, Y. Nishimura, V. Angelopoulos, O. Le Contel, J.B. Bonnell, Global distribution of wave amplitudes and wave normal distributions of chorus waves with high-resolution THEMIS wave observations. J. Geophys. Res. **116**, A12205 (2011a). doi:10.1029/2011JA017035
W. Li, J. Bortnik, R.M. Thorne, Y. Nishimura, V. Angelopoulos, L. Chen, Modulation of whistler-mode chorus waves: 2 role of density variations. J. Geophys. Res. **116**, A06206 (2011b). doi:10.1029/2010JA016313
W. Li, R.M. Thorne, J. Bortnik, Y. Nishimura, V. Angelopoulos, Modulation of whistler mode chorus waves: 1. Role of compressional Pc4–5 pulsations. J. Geophys. Res. **116**, A06205 (2011c). doi:10.1029/2010JA016312
W. Li, R.M. Thorne, J. Bortnik, Y.Y. Shprits, Y. Nishimura, V. Angelopoulos, C. Chaston, O. Le Contel, J.W. Bonnell, Typical properties of rising and falling tone chorus waves. Geophys. Res. Lett. **38**, L14103 (2011d). doi:10.1029/2011GL047925
J. Liang, V. Uritsky, E. Donovan, B. Ni, E. Spanswick, T. Trondsen, J. Bonnell, A. Roux, U. Auster, D. Larson, THEMIS observations of electron cyclotron harmonic emissions, ULF waves, and pulsating auroras on January 4 2009. J. Geophys. Res. **115**, A10235 (2010). doi:10.1029/2009JA015148

J. Liang, B. Ni, E. Spanswick, M. Kubyshkina, E.F. Donovan, V.M. Uritsky, R.M. Thorne, V. Angelopoulos, Fast earthward flows, electron cyclotron harmonic waves, and diffuse auroras: conjugate observations and synthesized scenario. J. Geophys. Res. **116**, A12220 (2011a). doi:10.1029/2011JA017094

J. Liang, E. Spanswick, M.J. Nicolls, E.F. Donovan, D. Lummerzheim, W. Liu, (2011b), Multi-instrument observations of soft-electron precipitation and its association with magnetospheric flows. J. Geophys. Res. **116**. doi:10.1029/2010JA015867

J. Liang, E. Donovan, E. Spanswick, V. Angelopoulos, Multiprobe estimation of field line curvature radius in the equatorial magnetosphere and the use of proton precipitations in magnetosphere-ionosphere mapping. J. Geophys. Res. Space Phys. **118**, 4924–4945 (2013). doi:10.1002/jgra.50454

J. Liang, E. Donovan, B. Ni, C. Yue, F. Jiang, V. Angelopoulos, On an energy-latitude dispersion pattern of ion precipitation potentially associated with magnetospheric EMIC waves. J. Geophys. Res. Space Phys. **119**, 8137–8160 (2014). doi:10.1002/2014JA020226

E. Loomis, On the geographic distribution of auroras in the northern hemisphere. Am. J. Sci. Arts **30**, 89–94 (1860)

A.T.Y. Lui, C.D. Anger, A uniform belt of diffuse auroral emissions seen by the ISIS-2 scanning photometer. Planet. Space Sci. **21**, 809 (1973)

A.T.Y. Lui, D. Venkatesan, C.D. Anger, S.-I. Akasofu, W.J. Heikkila, J.D. Winningham, J.R. Burrows, Simultaneous observations of particle precipitations and auroral emissions by the isis 2 satellite in the 19-24 MLT sector. J. Geophys. Res. **82**(16), 2210–2226 (1977)

D. Lummerzheim, Electron transport and optical emissions in the aurora. Ph.D. thesis, Univ. of Alaska, Fairbanks (1987)

L.R. Lyons, Electron diffusion driven by magnetospheric electrostatic waves. J. Geophys. Res. **79**(4), 575–580 (1974a)

L.R. Lyons, General relations for resonant particle diffusion in pitch angle and energy. J. Plasma Phys. **12**, 45–49 (1974b). doi:10.1017/S0022377800024910

L. Lyons, R. Thorne, C. Kennel, Pitch-angle diffusion of radiation belt electrons within the plasmasphere. J. Geophys. Res. **77**(19), 3455–3474 (1972)

Q. Ma, B. Ni, X. Tao, R.M. Thorne, Evolution of the plasma sheet electron pitch angle distribution by whistler-mode chorus waves in non-dipolar magnetic fields. Ann. Geophys. **30**, 751–760 (2012). doi:10.5194/angeo-30-751-2012

Q. Ma et al., Modeling inward diffusion and slow decay of energetic electrons in the Earth's outer radiation belt. Geophys. Res. Lett. **42**, 987–995 (2015). doi:10.1002/2014GL062977

J.P. McCollough, S.R. Elkington, D.N. Baker, The role of Shabansky orbits in compression-related electromagnetic ion cyclotron wave growth. J. Geophys. Res. **117**, A01208 (2012). doi:10.1029/2011JA016948

C.-I. Meng, B. Mauk, C.E. McIlwain, Electron precipitation of evening diffuse aurora and its conjugate electron fluxes near the magnetospheric equator. J. Geophys. Res. **84**(A6), 2545–2558 (1979)

N.P. Meredith, R.B. Horne, A.D. Johnstone, R.R. Anderson, The temporal evolution of electron distributions and associated wave activity following substorm injections in the inner magnetosphere. J. Geophys. Res. **105**(A6), 12907–12917 (2000)

N.P. Meredith, R.B. Horne, R.R. Anderson, Substorm dependence of chorus amplitudes: implications for the acceleration of electrons to relativistic energies. J. Geophys. Res. **106**(A7), 13165–13178 (2001). doi:10.1029/2000JA900156

N.P. Meredith, M. Cain, R.B. Horne, R.M. Thorne, D. Summers, R.R. Anderson, Evidence for chorus-driven electron acceleration to relativistic energies from a survey of geomagnetically disturbed periods. J. Geophys. Res. **108**(A6), 1248 (2003a). doi:10.1029/2002JA009764

N.P. Meredith, R.M. Thorne, R.B. Horne, D. Summers, B.J. Fraser, R.R. Anderson, Statistical analysis of relativistic electron energies for cyclotron resonance with EMIC waves observed on CRRES. J. Geophys. Res. **108**(A6), 1250 (2003b). doi:10.1029/2002JA009700

N.P. Meredith, R.B. Horne, R.M. Thorne, R.R. Anderson, Survey of upper band chorus and ECH waves: implications for the diffuse aurora. J. Geophys. Res. **114**, A07218 (2009). doi:10.1029/2009JA014230

N.P. Meredith, R.B. Horne, T. Kersten, B.J. Fraser, R.S. Grew, Global morphology and spectral properties of EMIC waves derived from CRRES observations. J. Geophys. Res. Space Phys. **119**, 5328–5342 (2014). doi:10.1002/2014JA020064

K. Min, J. Lee, K. Keika, W. Li, Global distribution of EMIC waves derived from THEMIS observations. J. Geophys. Res. **117**, A05219 (2012). doi:10.1029/2012JA017515

Y. Miyoshi et al., Time of flight analysis of pulsating aurora electrons, considering wave-particle interactions with propagating whistler mode waves. J. Geophys. Res. **115**, A10312 (2010). doi:10.1029/2009JA015127

Y. Miyoshi et al., Energetic electron precipitation associated with pulsating aurora: EISCAT and Van Allen Probes observations. J. Geophys. Res. **120** (2015). doi:10.1029/2014JA020690

T.E. Moore, R.L. Arnoldy, J. Feynman, D.A. Hardy, Propagating substorm injection fronts. J. Geophys. Res. **86**, 6713–6726 (1981). doi:10.1029/JA086iA08p06713
S.K. Morley, S.T. Ables, M.D. Sciffer, B.J. Fraser, Multipoint observations of Pc1-2 waves in the afternoon sector. J. Geophys. Res. **114**, A09205 (2009). doi:10.1029/2009JA014162
H. Muto, M. Hayakawa, M. Parrot, F. Lefeuvre, Direction finding of half-gyrofrequency VLF emissions in the off-equatorial region of the magnetosphere and their generation and propagation. J. Geophys. Res. **92**(A7), 7538–7550 (1987). doi:10.1029/JA092iA07p07538
A. Nakajima et al., Electron and wave characteristics observed by the THEMIS satellites near the magnetic equator during a pulsating aurora. J. Geophys. Res. **117**, A03219 (2012). doi:10.1029/2009JA015127
P.T. Newell, Reconsidering the inverted-V particle signature: relative frequency of large-scale electron acceleration events. J. Geophys. Res. **105**, 15779 (2000). doi:10.1029/1999JA000051
P.T. Newell, T. Sotirelis, S. Wing, Diffuse, monoenergetic, and broadband aurora: the global precipitation budget. J. Geophys. Res. **114**, A09207 (2009). doi:10.1029/2009JA014326
P.T. Newell, T. Sotirelis, S. Wing, Seasonal variations in diffuse, monoenergetic, and broadband aurora. J. Geophys. Res. **115**, A03216 (2010). doi:10.1029/2009JA014805
B. Ni, R.M. Thorne, Y.Y. Shprits, J. Bortnik, Resonant scattering of plasma sheet electrons by whistler-mode chorus: contribution to diffuse auroral precipitation. Geophys. Res. Lett. **35**, L11106 (2008). doi:10.1029/2008GL034032
B. Ni, R.M. Thorne, R.B. Horne, N.P. Meredith, Y.Y. Shprits, L. Chen, W. Li, Resonant scattering of plasma sheet electrons leading to diffuse auroral precipitation: 1. Evaluation for electrostatic electron cyclotron harmonic waves. J. Geophys. Res. **116**, A04218 (2011a). doi:10.1029/2010JA016232
B. Ni, R.M. Thorne, J. Liang, V. Angelopoulos, C. Cully, W. Li, X. Zhang, M. Hartinger, O. LeContel, A. Roux, Global distribution of electrostatic electron cyclotron harmonic waves observed on THEMIS. Geophys. Res. Lett. **38**, L17105 (2011b). doi:10.1029/2011GL048793
B. Ni, R.M. Thorne, N.P. Meredith, R.B. Horne, Y.Y. Shprits, Resonant scattering of plasma sheet electrons leading to diffuse auroral precipitation: 2. Evaluation for whistler mode chorus waves. J. Geophys. Res. **116**, A04219 (2011c). doi:10.1029/2010JA016233
B. Ni, R.M. Thorne, N.P. Meredith, Y.Y. Shprits, R.B. Horne, Diffuse auroral scattering by whistler mode chorus waves: dependence on wave normal angle distribution. J. Geophys. Res. **116**, A10207 (2011d). doi:10.1029/2011JA016517
B. Ni, R.M. Thorne, Y.Y. Shprits, K.G. Orlova, N.P. Meredith, Chorus-driven resonant scattering of diffuse auroral electrons in nondipolar magnetic fields. J. Geophys. Res. **116**, A06225 (2011e). doi:10.1029/2011JA016453
B. Ni, J. Liang, R.M. Thorne, V. Angelopoulos, R.B. Horne, M. Kubyshkina, E. Spanswick, E.F. Donovan, D. Lummerzheim, Efficient diffuse auroral electron scattering by electrostatic electron cyclotron harmonic waves in the outer magnetosphere: a detailed case study. J. Geophys. Res. **117**, A01218 (2012a). doi:10.1029/2011JA017095
B. Ni, R.M. Thorne, Q. Ma, Bounce-averaged Fokker-Planck diffusion equation in non-dipolar magnetic fields with applications to the Dungey magnetosphere. Ann. Geophys. **30**, 733–750 (2012b). doi:10.5194/angeo-30-733-2012
B. Ni, J. Bortnik, Y. Nishimura, R.M. Thorne, W. Li, V. Angelopoulos, Y. Ebihara, A.T. Weatherwax, Chorus wave scattering responsible for the Earth's dayside diffuse auroral precipitation: a detailed case study. J. Geophys. Res. Space Phys. **19**, 897–908 (2014). doi:10.1002/2013JA019507
B. Ni, X. Cao, Z. Zou, C. Zhou, X. Gu, J. Bortnik, J. Zhang, S. Fu, Z. Zhao, R. Shi, L. Xie, Resonant scattering of outer zone relativistic electrons by multi-band EMIC waves and resultant electron loss timescales. J. Geophys. Res. Space Phys. **120** (2015). doi:10.1002/2015JA021466
Y. Nishimura et al., Identifying the driver of pulsating aurora. Science **330**, 81–84 (2010). doi:10.1126/science.1193186
Y. Nishimura, J. Bortnik, W. Li, R.M. Thorne, L. Chen, L.R. Lyons, V. Angelopoulos, S.B. Mende, J. Bonnell, O. Le Contel, C. Cully, R. Ergun, U. Auster, Multi-event study of the correlation between pulsating aurora and whistler-mode chorus emissions. J. Geophys. Res. **116**, A11221 (2011). doi:10.1029/2011JA016876
Y. Nishimura et al., Structures of dayside whistler-mode waves deduced from conjugate diffuse aurora. J. Geophys. Res. Space Phys. **118**, 664–673 (2013). doi:10.1029/2012JA018242
T. Nishiyama et al., The source region and its characteristic of pulsating aurora based on the Reimei observations. J. Geophys. Res. **116**, A03226 (2011). doi:10.1029/2010JA015507
D. Nunn, Y. Omura, H. Matsumoto, I. Nagano, S. Yagitani, The numerical simulation of VLF chorus and discrete emissions observed on the Geotail satellite using a Vlasov code. J. Geophys. Res. **102**(A12), 27083–27097 (1997). doi:10.1029/97JA02518
Y. Omura, Y. Katoh, D. Summers, Theory and simulation of the generation of whistler-mode chorus. J. Geophys. Res. **113**, A04223 (2008). doi:10.1029/2007JA012622

K.G. Orlova, Y.Y. Shprits, Dependence of pitch-angle scattering rates and loss timescales on the magnetic field model. Geophys. Res. Lett. **37**, L05105 (2010). doi:10.1029/2009GL041639

K.G. Orlova, Y.Y. Shprits, On the bounce-averaging of scattering rates and the calculation of bounce period. Phys. Plasmas **18**, 092904 (2011). doi:10.1063/1.3638137

K. Orlova, Y.Y. Shprits, Model of lifetimes of the outer radiation belt electrons in a realistic magnetic field using realistic chorus wave parameters. J. Geophys. Res. Space Phys. **119**(2), 770–780 (2014). doi:10.1002/2013JA019596

M. Ozaki et al., Observed correlation between pulsating aurora and chorus wave at Syowa station in Antarctica: a case study. J. Geophys. Res. **117**, A08211 (2012). doi:10.1029/2011JA017478

C. Paranicas, W.J. Hughes, H.J. Singer, R.R. Anderson, Banded electrostatic emissions observed by the CRRES plasma wave experiment. J. Geophys. Res. **97**(A9), 13889–13898 (1992)

M. Parrot, C.A. Gaye, A statistical survey of ELF waves in a geostationary orbit. Geophys. Res. Lett. **21**(23), 2463–2466 (1994). doi:10.1029/94GL01700

S.M. Petrinec, D.L. Chenette, J. Mobilia, M.A. Rinaldi, W.L. Imhof, Statistical X ray auroral emissions—PIXIE observations. Geophys. Res. Lett. **26**(11), 1565–1568 (1999)

J.S. Pickett et al., Cluster observations of EMIC triggered emissions in association with Pc1 waves near Earth's plasmapause. Geophys. Res. Lett. **37**, L09104 (2010). doi:10.1029/2010GL042648

J.L. Roeder, H.C. Koons, A survey of electron cyclotron waves in the magnetosphere and the diffuse auroral electron precipitation. J. Geophys. Res. **94**(A3), 2529–2541 (1989)

J.G. Roederer, *Dynamics of Geomagnetically Trapped Radiation* (Springer, New York, 1970)

M. Samara, R.G. Michell, Ground-based observations of diffuse auroral frequencies in the context of whistler mode chorus. J. Geophys. Res. **115**, A00F18 (2010). doi:10.1029/2009JA014852

M. Samara, R.G. Michell, K. Asamura, M. Hirahara, D.L. Hampton, H.C. Stenbaek-Nielsen, Ground-based observations of diffuse auroral structures in conjunction with Reimei measurements. Ann. Geophys. **28**, 873–881 (2010)

B.P. Sandford, Variations of auroral emissions with time, magnetic activity and the solar cycle. J. Atmos. Terr. Phys. **30**, 1921–1942 (1968)

O. Santolík, D.A. Gurnett, J.S. Pickett, M. Parrot, N. Cornilleau-Wehrlin, Spatio-temporal structure of storm-time chorus. J. Geophys. Res. **108**(A7), 1278 (2003). doi:10.1029/2002JA009791

O. Santolík, D.A. Gurnett, J.S. Pickett, J. Chum, N. Cornilleau-Wehrlin, Oblique propagation of whistler mode waves in the chorus source region. J. Geophys. Res. **114**, A00F03 (2009). doi:10.1029/2009JA014586

N. Sato, D.M. Wright, C.W. Carlson, Y. Ebihara, M. Sato, T. Saemundsson, S.E. Milan, M. Lester, Generation region of pulsating aurora obtained simultaneously by the FAST satellite and a Syowa-Iceland conjugate pair of observatories. J. Geophys. Res. **109**, A10201 (2004). doi:10.1029/2004JA010419

M. Schulz, Particle drift and loss rates under strong pitch angle diffusion in Dungey's model magnetosphere. J. Geophys. Res. **103**(A1), 61–67 (1998)

M. Schulz, L.J. Lanzerotti, *Particle Diffusion in the Radiation Belts*. Physics and Chemistry in Space (Springer, New York, 1974)

V.A. Sergeev, E. Sazhina, N. Tsyganenko, J. Lundblad, F. Soraas, Pitch-angle scattering of energetic protons in the magnetotail current sheet as the dominant source of their isotropic precipitation into the nightside ionosphere. Planet. Space Sci. **31**, 1147–1155 (1983)

V. Sergeev, V. Angelopoulos, S. Apatenkov, J. Bonnell, R. Ergun, R. Nakamura, J. McFadden, D. Larson, A. Runov, Kinetic structure of the sharp injection/dipolarization front in the flow-braking region. Geophys. Res. Lett. **36**, L21105 (2009). doi:10.1029/2009GL040658

R.R. Shaw, D.A. Gurnett, Electrostatic noise bands associated with the electron gyrofrequency and plasma frequency in the outer magnetosphere. J. Geophys. Res. **80**(31), 4259–4271 (1975). doi:10.1029/JA080i031p04259

R. Shi, D. Han, B. Ni, Z.-J. Hu, C. Zhou, X. Gu, Intensification of dayside diffuse auroral precipitation: contribution of dayside whistler-mode chorus waves in realistic magnetic fields. Ann. Geophys. **30**, 1297–1307 (2012). doi:10.5194/angeo-30-1297-2012

R. Shi, Z.-J. Hu, B. Ni, D. Han, X. Chen, C. Zhou, X. Gu, Modulation of the dayside diffuse auroral intensity by the solar wind dynamic pressure. J. Geophys. Res. Space Phys. **119**, 10092–10099 (2014). doi:10.1002/2014JA020180

Y.Y. Shprits, B. Ni, Dependence of the quasi-linear scattering rates on the wave normal distribution of chorus waves. J. Geophys. Res. **114**, A11205 (2009). doi:10.1029/2009JA014223

Y.Y. Shprits, W. Li, R.M. Thorne, Controlling effect of the pitch-angle scattering rates near the edge of the loss cone on electron lifetimes. J. Geophys. Res. **111**, A12206 (2006a). doi:10.1029/2006JA011758

Y.Y. Shprits, R.M. Thorne, R.B. Horne, D. Summers, Bounce-averaged diffusion coefficients for field-aligned chorus waves. J. Geophys. Res. **111**, A10225 (2006b). doi:10.1029/2006JA011725

Y.Y. Shprits, S. Elkington, N.P. Meredith, D.A. Subbotin, Review of modeling of losses and sources of relativistic electrons in the outer radiation belt I: radial transport. J. Atmos. Sol.-Terr. Phys. **70**, 1679–1693 (2008a). doi:10.1016/j.jastp.2008.06.008

Y.Y. Shprits, D.A. Subbotin, N.P. Meredith, S. Elkington, Review of modeling of losses and sources of relativistic electrons in the outer radiation belt II: local acceleration and loss. J. Atmos. Sol.-Terr. Phys. **70**, 1694–1713 (2008b). doi:10.1016/j.jastp.2008.06.014

Y.Y. Shprits, D. Subbotin, B. Ni, Evolution of electron fluxes in the outer radiation belt computed with the VERB code. J. Geophys. Res. **114**, A11209 (2009). doi:10.1029/2008JA013784

A.R. Soto-Chavez, G. Wang, A. Bhattacharjee, G.Y. Fu, H.M. Smith, A model for falling-tone chorus. Geophys. Res. Lett. **41**, 1838–1845 (2014). doi:10.1002/2014GL059320

D. Steele, D. McEwen, Electron auroral excitation efficiencies and intensity ratios. J. Geophys. Res. **95**(A7), 10321–10336 (1990)

T.H. Stix, *The Theory of Plasma Waves* (McGraw-Hill, New York, 1962)

Z. Su, H. Zheng, S. Wang, Evolution of electron pitch angle distribution due to interactions with whistler mode chorus following substorm injections. J. Geophys. Res. **114**, A08202 (2009). doi:10.1029/2009JA014269

D. Summers, Quasi-linear diffusion coefficients for field-aligned electromagnetic waves with applications to the magnetosphere. J. Geophys. Res. **110**, A08213 (2005). doi:10.1029/2005JA011159

D. Summers, R.M. Thorne, Relativistic electron pitch angle scattering by electromagnetic ion cyclotron waves during geomagnetic storms. J. Geophys. Res. **108**(A4), 1143 (2003). doi:10.1029/2002JA009489

D. Summers, R.M. Thorne, F. Xiao, Relativistic theory of wave-particle resonant diffusion with application to electron acceleration in the magnetosphere. J. Geophys. Res. **103**(A9), 20487–20500 (1998). doi:10.1029/98JA01740

D. Summers, B. Ni, N.P. Meredith, Timescales for radiation belt electron acceleration and loss due to resonant wave-particle interactions: 2. Evaluation for VLF chorus, ELF hiss, and electromagnetic ion cyclotron waves. J. Geophys. Res. **112**, A04207 (2007). doi:10.1029/2006JA011993

D.W. Swift, Mechanisms for auroral precipitation: a review. Rev. Geophys. **19**(1), 185–211 (1981)

X. Tao, R.M. Thorne, W. Li, B. Ni, N.P. Meredith, R.B. Horne, Evolution of electron pitch angle distributions following injection from the plasma sheet. J. Geophys. Res. **116**, A04229 (2011). doi:10.1029/2010JA016245

R.M. Thorne, R. Horne, The contribution of ion-cyclotron waves to electron heating and SAR-arc excitation near the stormtime plasmapause. Geophys. Res. Lett. **19**, 417–420 (1992). doi:10.1029/92GL00089

R.M. Thorne, R. Horne, Modulation of electromagnetic ion cyclotron instability due to interaction with ring current O+ during magnetic storms. J. Geophys. Res. **102**(A7), 14155–14163 (1997). doi:10.1029/96JA04019

R.M. Thorne, C.F. Kennel, Relativistic electron precipitation during magnetic storm main phase. J. Geophys. Res. **76**(19), 4446–4453 (1971). doi:10.1029/JA076i019p04446

R.M. Thorne, B. Ni, X. Tao, R.B. Horne, N.P. Meredith, Scattering by chorus waves as the dominant cause of diffuse auroral precipitation. Nature **467** (2010). doi:10.1038/nature09467

R.M. Thorne, W. Li, B. Ni, Q. Ma, J. Bortnik, L. Chen, D.N. Baker, H.E. Spence, G.D. Reeves, M.G. Henderson, C.A. Kletzing, W.S. Kurth, G.B. Hospodarsky, J.B. Blake, J.F. Fennell, S.G. Claudepierre, Rapid local acceleration of relativistic radiation-belt electrons by magnetospheric chorus. Nature **504**, 411–414 (2013a). doi:10.1038/nature12889

R.M. Thorne, B. Ni, X. Tao, L. Chen, W. Li, N.P. Meredith, R.B. Horne, Y.Y. Shprits, Correction to "Resonant scattering of plasma sheet electrons leading to diffuse auroral precipitation: 1. Evaluation for electrostatic electron cyclotron harmonic waves", "Resonant scattering of plasma sheet electrons leading to diffuse auroral precipitation: 2. Evaluation for whistler mode chorus waves", and "Evolution of pitch-angle distributions following injection from the plasma sheet". J. Geophys. Res. Space Phys. **118**, 839–842 (2013b). doi:10.1002/jgra.50154

K. Tsuruda et al., Correlations between the very low frequency chorus and pulsating aurora observed by low-light-level television at L = 4.4. Can. J. Phys. **59**, 1042–1048 (1981). doi:10.1139/p81-137

B.T. Tsurutani, E.J. Smith, Postmidnight chorus: a substorm phenomenon. J. Geophys. Res. **79**(1), 118–127 (1974). doi:10.1029/JA079i001p00118

B.T. Tsurutani, E.J. Smith, Two types of magnetospheric ELF chorus and their substorm dependences. J. Geophys. Res. **82**(32), 5112–5128 (1977). doi:10.1029/JA082i032p05112

N.A. Tsyganenko, A model of the near magnetosphere with a dawn-dusk asymmetry 1. Mathematical structure. J. Geophys. Res. **107**(A8), 1179 (2002a). doi:10.1029/2001JA000219

N.A. Tsyganenko, A model of the near magnetosphere with a dawn-dusk asymmetry: 2. Parameterization and fitting to observations. J. Geophys. Res. **107**(A8), 1176 (2002b). doi:10.1029/2001JA000220

M.E. Usanova et al., Conjugate ground and multisatellite observations of compression-related EMIC Pc1 waves and associated proton precipitation. J. Geophys. Res. **115**, A07208 (2010). doi:10.1029/2009JA014935

M.E. Usanova, I.R. Mann, J. Bortnik, L. Shao, V. Angelopoulos, THEMIS observations of electromagnetic ion cyclotron wave occurrence: dependence on AE, SYMH, and solar wind dynamic pressure. J. Geophys. Res. **117**, A10218 (2012). doi:10.1029/2012JA018049

E. Villalón, W.J. Burke, Pitch angle scattering of diffuse auroral electrons by whistler mode waves. J. Geophys. Res. **100**(A10), 19361–19369 (1995)

A.D.M. Walker, *Plasma Waves in the Magnetosphere* (Springer, New York, 1993)

M. Walt, *Introduction to Geomagnetically Trapped Radiation* (Cambridge University Press, Cambridge, 1994)

J.D. Winningham, C.D. Anger, G.G. Shepherd, E.J. Weber, R.A. Wagner, A case study of the aurora, high-latitude ionosphere, and particle precipitation during near-steady state conditions. J. Geophys. Res. **83**, 5717–5731 (1978)

T. Yamamoto, On the temporal fluctuations of pulsating auroral luminosity. J. Geophys. Res. **93**, 897–911 (1988)

A.W. Yau et al., Rocket-borne measurements of particle pulsation in pulsating aurora. J. Geophys. Res. **86**, 5673–5681 (1981)

T.S.T. Young, J.D. Callen, J.E. McCune, High-frequency electrostatic waves in the magnetosphere. J. Geophys. Res. **78**(7), 1082–1099 (1973). doi:10.1029/JA078i007p01082

X. Yu, Z. Yuan, D. Wang, H. Li, S. Huang, Z. Wang, Q. Zheng, M. Zhou, C.A. Kletzing, J.R. Wygant, In situ observations of EMIC waves in O+ band by the Van Allen Probe A. Geophys. Res. Lett. **42**, 1312–1317 (2015). doi:10.1002/2015GL063250

X. Zhang, V. Angelopoulos, On the relationship of electrostatic cyclotron harmonic emissions with electron injections and dipolarization fronts. J. Geophys. Res. Space Phys. **119** (2014). doi:10.1002/2013JA019540

J.-C. Zhang, L.M. Kistler, C.G. Mouikis, M.W. Dumlop, B. Klecker, J.-A. Sauvaud, A case study of EMIC wave-associated He+ energization in the outer magnetosphere: cluster and Double Star 1 observations. J. Geophys. Res. **115**, A06212 (2010). doi:10.1029/2009JA014784

J.-C. Zhang, L.M. Kistler, C.G. Mouikis, B. Klecker, J.-A. Sauvaud, M.W. Dumlop, A statistical study of EMIC wave-associated He+ energization in the outer magnetosphere: cluster/CODIF observations. J. Geophys. Res. **116**, A11201 (2011). doi:10.1029/2011JA016690

X. Zhang, V. Angelopoulos, B. Ni, R.M. Thorne, R.B. Horne, Quasi-steady, marginally unstable electron cyclotron harmonic wave amplitudes. J. Geophys. Res. Space Phys. **118**, 3165–3172 (2013). doi:10.1002/jgra.50319

X. Zhang, V. Angelopoulos, B. Ni, R.M. Thorne, R.B. Horne, Extent of ECH wave emissions in Earth's magnetotail. J. Geophys. Res. **119**, 5561–5574 (2014). doi:10.1002/2014JA019931

X. Zhang, V. Angelopoulos, B. Ni, R.M. Thorne, Predominance of ECH wave contribution to diffuse aurora in Earth's outer magnetosphere. J. Geophys. Res. Space Phys. **120**, 295–309 (2015). doi:10.1002/2014JA020455